

Natural strain in glacial and diapiric rock salt, with
emphasis on Oakwood Dome, East Texas

by

M. P. A. Jackson

Milestone Contract Report for the U. S. Department of Energy
under Contract No. DE-AC97-80ET46617

Bureau of Economic Geology
W. L. Fisher, Director
The University of Texas at Austin
Austin, Texas

1983

CONTENTS

ABSTRACT	
INTRODUCTION	1
PART I: GRAVITY-DRIVEN DUCTILE-FLOW STRUCTURES	1
Internal structure of ice and salt glaciers	1
Ice glaciers	1
Salt glaciers	3
Internal structure of salt diapirs	5
Mineral fabrics	6
Folds	7
Ductile shear zones	8
Fold style in salt stocks	10
Mechanics of similar folding	12
Formation of folds and interference structures in salt stocks	14
Assessing large-scale flow patterns from linear elements	18
Natural strain rates in salt	23
Physical conditions of salt diapirism	26
PART II: STRUCTURE OF THE TOG-1 SALT CORE, OAKWOOD DOME	26
Geometric analysis	28
Structural elements	28
Defining orientation in nonoriented core	28
Structural cross section	29
Implications to internal structure	31
Strain analysis	31
Two-dimensional strains	34
Three-dimensional strains	40

Significance of measured strains	43
Actual strains and measured strains	43
Model strains and measured strains	45
Recrystallization and measured strains	46
CONCLUSIONS	48
ACKNOWLEDGMENTS	50
REFERENCES	52

ABSTRACT

In Part I, structural styles in the gravity-driven, ductile-flow processes of glaciers and diapirs are analyzed. Salt glaciers flow under minute differential stress when dampened by rainfall. Thus, the concentration of water in diapiric rock salt is of paramount importance to predicting creep rates in a repository medium. Natural strain rates for rock salt vary enormously from $10^8/s$ to $10^{16}/s$; slowest rates are those for average diapiric uplift. Contrary to widespread generalization, structural attitudes in dome-salt mines are predominantly moderate to steep, rather than vertical.

In the proposed model, diapiric folds are triggered by (1) shear stresses induced by upward flow, (2) shear stresses induced by boundary effects of the salt source layer, and (3) normal stresses induced by convergent flow. Folding in salt stocks follows the similar-fold model although many folds appear to have been initiated by buckling. Closed interference structures are sheath folds formed by intense constriction of originally gentle fold culminations and depressions. Construction of plunge-isogon maps from mapped linear structures allows the flow directions of diapiric salt to be deduced.

Part II describes the results of geometric analysis and strain analysis of salt core from Oakwood Dome. The core has penetrated the hinge zone and lower limb of an inclined overturned antiform, which probably represents a salt tongue that has spread outward from the diapir center. Structural evidence indicates severe truncation of the diapir crest, probably by ground-water dissolution during cap-rock formation. The uppermost 2 m of rock salt recrystallized in the presence of water. Consideration of homologous temperatures and present maximum erosion rates suggests that the salt recrystallized at least 3 million years ago at depths 400 m greater than present.

All the strains recorded in Oakwood halite are of the flattening type. The ratio of flattening to constriction increases upward, whereas the strain intensity decreases upward, perhaps in transition to an originally "neutral" zone in the diapir, since removed by dissolution. The orientations of maximum-extension directions in rock salt vary widely.

INTRODUCTION

This report comprises two parts. Part I represents a literature survey of structural styles in the gravity-driven ductile-flow processes of glaciers and diapirs, together with a reinterpretation of these structures in light of modern structural theory. Part II describes aspects of the internal structure of Oakwood Dome in the East Texas Basin, as revealed by geometric analysis and strain analysis of a D.O.E.-funded salt core. A companion study on the lithology, microstructures, fluid inclusions, and geochemistry of the same salt core has already been published under funding from the same program (Dix and Jackson, 1982).

PART I: GRAVITY-DRIVEN DUCTILE-FLOW STRUCTURES

Internal Structure of Ice and Salt Glaciers

Glaciers provide readily observable natural analogues for diapiric flow of rock salt. Both are gravity-driven examples of large-scale creep of fairly pure metamorphic rock, and both contain a complex array of superposed fabrics, recrystallization zones, and zones of inhomogeneous shear. Although the boundary conditions in glaciers and diapirs are different, glaciers merit close study because the sequence of deformation during their creep may be easily studied in crevassed exposures or drill cores from the head of the glacier to the wasting snout. Before reviewing the nature of deformation in salt glaciers, relevant findings on the fabrics in ice glaciers are briefly discussed. Ice glaciers have been far more intensively studied on account of their greater abundance.

Ice glaciers

In broad terms the strain state of ice glaciers can be summarized as pure shear (coaxial strain) in the center and simple shear (non-coaxial strain) along the margins (Hambrey, 1979). However this gross distortion is accompanied by a large degree of strain heterogeneity on smaller scales. These small-scale structures are thought to be the result of different patterns

of cumulative deformation (i.e., different combinations of superposed strain) rather than direct reflections of the local stress state or strain rate (Hudleston and Hooke, 1980). The presence of recumbent folds indicates unsteady laminar flow (Hudleston, 1976), a process that almost certainly also operates in salt glaciers and diapirs. The two main fabric elements in glacial ice are layering (termed foliation in glaciology), and preferred crystallographic orientation. It has been convincingly argued with the aid of mathematical modeling (Hooke and Hudleston, 1978; Hudleston and Hooke, 1980) that layering forms not by migration of entrained dirt or bubbles, but by strain modification of primary inhomogeneities. For instance, irregularities such as ice glands and lenses and crevasse fillings that are initially normal to sedimentary stratification, rotate toward the XY strain plane to within 1° of mutual parallelism with the stratification in the distal parts of the glacier. This massive rotation and resulting high degree of subhorizontal parallelism may have its counterpart in the regular vertical layering within salt diapirs.

In the Barnes Ice Cap on Baffin Island, the ice initially consists of equant polygonal grains with no preferred orientation or with a weak vertical concentration of c axes (Hudleston, 1980). This near-isotropic fabric becomes progressively deformed near the glacial margins, the first signs of strain being the formation of shear zones parallel to bedrock with an aspect ratio of about 20:1. Each ductile zone of shear is outlined by sigmoidal patterns of elongated air bubbles and is marked by (1) decrease in plunge of elongated air bubbles, (2) increase in degree of c -axis preferred orientation, (3) development of weakly sutured grain boundaries, and (4) increase in grain size (Hudleston, 1980). Despite the high shear strains indicated by bubble inclination and elongation, the ice grains are equant, indicating recrystallization and grain growth during or after shearing. By analogy, megacrysts of salt arranged in planar zones in some diapirs may also mark the sites of fossil shear zones as well as fractures that formerly allowed ingress of brine. Increase in overall deformation of the ice results from the growth and coalescence of shear zones. Initially lenses of less deformed rock are isolated, and ultimately coalesce completely. Thus the glacial margin forms a single, large, highly strained shear zone

with only scattered pods of weakly deformed ice remaining. Hudleston (1980) compared c-axis patterns in glacial ice to those in natural or simulated quartzites deformed by simple shear in which basal glide dominated (Lister and Price, 1978). The voids that must have resulted from deformation with only one slip system are thought to have been closed by grain fracture, recrystallization, and grain-boundary sliding (Hudleston, 1980).

Salt glaciers

Kent (1979) has described the salt glaciers of southern Iran as "one of the geological wonders of the world." These remarkable structures also provide valuable analogues to diapiric flow of salt in that the complete sequence of deformation from bedded salt in the neck of the plug to mylonitized and partially dissolved salt at the glacial snout is exposed for observation. The Hormuz Salt, part of a late Proterozoic evaporitic sequence, has risen from depths of 3 to 5 km through a virtually continuous carbonate overburden 3 km thick to breach the surface in the form of more than 200 salt plugs (Ala, 1974; Kent, 1979).

Initiation of diapirism and salt intrusion in the Jurassic and Early Cretaceous was followed by Early to Late Cretaceous salt extrusion (Kent, 1979). The bedded Hormuz Salt provided a weak décollement zone for Zagros folding which began (after salt extrusion) in the middle Miocene and reached a peak in the Plio-Pleistocene; fold propagation was controlled by weak points represented by preexisting salt plugs (Kent, 1979).

The salt plugs, generally 5 to 10 km across, contain entrained debris that ranges in size from sand grade to enormous exotic rafts of Cambrian sediments up to 7 km² in exposed area (Chah Benu salt plug). The absence of deformation in these large rafts, apart from gentle curvature, and the horizontal stratification of rock salt in some plugs (e.g., Jehani salt plug) suggest emplacement in a pistonlike manner and little internal deformation (Ala, 1974; Kent, 1979). This contrasts strongly with the highly deformed interiors of salt domes in northern Germany and the Texas-Louisiana Gulf Coast. Kent (1979) deduced that because of the absence at surface of the many cubic kilometers of country rock displaced from the neck of each plug,

salt must have initially extruded at much higher stratigraphic levels, followed by deep erosion of the original vent material and displaced overburden.

The topographic expression of each salt plug depends on the ratio of the rate of extrusion versus the rate of rain-induced solution. Where this ratio is less than one, the salt plug is a depression or even an empty crater; where this ratio is more than one, the plug forms a mountain (1,300 m high in the case of Kuh-e-Namak) with concentric crestal ridges. Exceptionally active extrusion causes the rock salt to overflow its confining scarps and descend as one or more salt glaciers.

Field evidence for the recent flow of salt glaciers has long been known: Harrison (1930) described the flow of a salt glacier over alluvium composed of wasting debris from a former glacier; Kent (1966, 1970) emphasized the necessity for active flow to maintain the elevated topography of salt against perpetual climatic attrition. But direct measurement of glacial flow is far from straightforward. It has only recently been accomplished (Talbot and Rogers, 1980). Measurements were hampered by the fact that the glacier expanded thermally during the day and recovered these elastic strains at night by shrinkage; furthermore the rock salt expanded after wetting--coincident with the period of maximum flow. The effects of dilation due to heating and wetting were allowed for in the strain rates calculated by Talbot and Rogers (1980) (table 1).

As in the case of ice glaciers, deformation increases down the length of a salt glacier (Talbot, 1979). New generations of folds and fabrics are generated by perturbation of laminar flow at each place rock salt impinges on a bedrock irregularity. Toward the snout the relative volume of rock salt impeded by each bedrock irregularity is smaller; this indicates a decrease in competency (Talbot, 1979). This "strain softening" can be correlated with a progressive decrease in grain size by mylonitization and an increase in the proportion of less soluble residue left by solution. Toward its distal parts the northern glacier of Kuh-e-Namak consists of three components: (1) porphyroclastic remnants of transparent halite characteristic of the salt plug,

(2) fine-grained mylonitized halite groundmass, and (3) entrained insoluble minerals; the proportion of (2) and (3) increases distally. These features show certain similarities with the ice glaciers discussed above. However, an important difference is that the high-strain zones of glacial ice are anomalously coarse grained; shear zones in other rock types, including glacial salt, are finer grained than the surrounding rock. This may possibly be due to the differences in homologous temperature ($T_h = \text{temperature in } ^\circ\text{K} \text{ divided by melting point, } T_m, \text{ of mineral in } ^\circ\text{K}$). Glacial ice deforms under high homologous temperatures of 0.9 or more, whereas glacial salt deforms under low homologous temperatures of 0.3 or less. The "hot working" of glacial ice may provide sufficient thermal energy to promote grain growth in the shear zones.

Internal Structure of Salt Diapirs

Previous studies of the internal structure of salt diapirs have been based on excavated cavities in salt mines of Texas and Louisiana. The floors and ceilings of these large caverns have provided horizontal cross sections enabling meticulous structural mapping (e.g. Balk, 1949, 1953; Muehlberger, 1959; Hoy and others, 1962; Kupfer, 1962). Because almost all structures in the trunk of salt diapirs dip or plunge steeply, these mine levels provide near-perfect structural profiles. Walls and pillars in cross sections correspond to blank areas of no outcrop at surface.

Apart from structural mapping, two other types of structural study have also been attempted. Firstly petrofabric analysis of halite in Winnfield Dome, Grand Saline Dome, and Avery Island Dome has yielded information on fabric orientation (Clabaugh, 1962a, b; Schwerdtner, 1966; Muehlberger and Clabaugh, 1968; Carter and Hansen, 1980). Because halite is isotropic, poles to all three of its crystallographic planes, parallel to cubic cleavage, must be plotted on the same stereogram. The resulting confused appearance of multiple maxima, submaxima, and girdles provides fertile ground for subjective interpretation. Matching these fabrics with larger structures such as folds is difficult. But comparison of the fabric patterns

with those of mathematical models provides some information on the mechanism of deformation: translation gliding is suggested to be dominant (Schwerdtner, 1967).

Secondly the pioneering structural studies of Balk (1949, 1953) in Grand Saline and Jefferson Domes included the first published data on grain shapes in the fabric of deformed rock salt. Grain shape and the relation between flattening and constriction form a large component in Part II of the present paper.

Mineral Fabrics

The mineral fabric of a rock sample is the pattern of crystallographic or morphologic orientation of mineral grains within it. The fabrics of most rocks deformed by penetrative strain (i. e. tectonites) contain a planar preferred orientation or a linear preferred orientation, or both. Such preferred orientations are termed schistosity and mineral lineation, respectively. Nevertheless, although commonly described as separate structures, schistosity and mineral lineation are merely different components of the same system--the mineral fabric.

This fact was clearly recognized by Flinn (1965) and was incorporated in his \underline{L} - \underline{S} system of tectonite fabrics. Rocks containing no linear preferred orientation within the schistosity plane are termed \underline{S} tectonites, whereas those containing a lineation but no planar preferred orientation are termed \underline{L} tectonites. The fact that most natural rocks contain fabrics intermediate between these ideal end members (see, for example, Grocott, 1979) was recognized in Flinn's three additional intermediate categories that reflect the variable dominance of planar (\underline{S}) and linear (\underline{L}) components. His entire \underline{L} - \underline{S} fabric system therefore has five categories: \underline{L} , $\underline{L}>\underline{S}$, $\underline{L}\approx\underline{S}$, $\underline{S}>\underline{L}$, and \underline{S} . The equivalent strain ellipsoids for constrictive and flattening strains forming these fabrics are prolate and oblate spheroids for the \underline{L} fabrics and \underline{S} fabrics, respectively, and orthorhombic triaxial ellipsoids for the composite \underline{L} - \underline{S} fabrics.

All preferred orientations and shape fabrics described in this paper are based on the shape of halite grains rather than on their crystallographic orientation because isometric crystals do not have a unique crystallographic axis.

Where mineral fabrics and shape fabrics have been studied, linear fabrics clearly dominate the interior of salt stocks. In Grand Saline Dome Balk (1949) observed true lineations (as opposed to apparent lineations representing the trace of planar structures on the vertical mine walls) in so many places that he believed that the entire salt stock was lineated. The halite crystals had their longest axes plunging steeply to vertically. Most axial ratios of vertical elliptical sections through these crystals were close to 1.5. Balk's (1949) "pencil anhydrite," in cigar-shaped aggregates 5-8 cm long with elliptical cross sections, indicates a $\underline{L}>\underline{S}$ fabric. Lineation in Winnfield Dome takes the form of cigar-shaped aggregates of anhydrite and crenulation lineation (Hoy and others, 1962). In Jefferson Island Dome, halite defines a \underline{L} fabric with mean vertical axial ratios of 1.6 and mean horizontal axial ratios of 1.0; this lineation is axial to subvertically plunging folds (Balk, 1953). Linear fabrics were also reported from parts of Avery Island Dome and Weeks Island Dome (Rogers, 1918; Balk, 1953). Steeply oriented and elongated halite with elliptical cross sections define $L>S$ fabrics throughout 767 m of vertical salt core from Vacherie Dome (Nance and others, 1979) and 762 m of vertical salt core from Rayburn's Dome (Nance and Wilcox, 1979); axial ratios in the vertical plane average 3 and 2, respectively. In both Vacherie and Rayburn's Domes these linear fabrics alternate with isotropic fabrics composed of equant halite crystals.

Geologists tend to overestimate the relative strengths of lineations when making qualitative judgments of rock fabrics (Schwerdtner and others, 1977). Bearing this caveat in mind, it nevertheless appears that $\underline{L}>\underline{S}$ fabrics dominate in regions of salt stocks that have been sampled, generally the upper parts.

Folds

Dark-gray layers of salt containing disseminated anhydrite, which alternate with pale-gray layers of pure rock salt, provide ideal marker surfaces to define the form of mesoscopic folds and shear zones. Steeply plunging folds invariably dominate the internal structure of salt stocks in Texas and Louisiana (Balk, 1949, 1953; Muehlberger, 1959; Hoy and others, 1962;

Kupfer, 1968, 1970; Muehlberger and Clabaugh, 1968; Howard, 1971). The traces of the limbs of these folds are exposed as subvertical bands in the walls of mined caverns. Hinge zones are generally exposed in the roofs and floors of such caverns, but because of significant departure from vertical plunge, hinge zones are also exposed in the walls. Despite the strong consistency of steep dip, axial surfaces vary widely in strike over a small distance, thus giving rise to polyclinal profiles. Parasitic folds are congruent to larger folds (Balk, 1949; Muehlberger, 1959).

Closures, or eyed folds, in cavern roofs are not particularly abundant but have nevertheless been noted in almost every Gulf Coast salt mine mapped because of their unusual appearance (Balk, 1949, 1953; Muehlberger, 1959; Hoy and others, 1962; Kupfer, 1962, 1968). These folds have a shape equivalent to that of a cup, greatly elongated along a vertical axis; their geometry is that of a paraboloid of revolution (Carey, 1962).

The distribution of folds is variable. For instance folds are reported to be common near the contact of Jefferson Island salt stock, but rare near the margins of Grand Saline salt stock. This rarity was attributed by Balk (1949) to the stabilizing effects of the boundary. But high contact strains could also have tightened folds into pseudoconformity, as inferred by Kupfer (1968) and modeled by Ramberg (1981, fig. 11.107). The axial surfaces of steeply plunging folds in Winnfield Dome are concentric around the axis of the diapir and dip inwards parallel to an inverted cone (Hoy and others, 1962). Geometric analysis shows that folds tighten and layering tends to become more concordant toward the margins, forming point distributions rather than partial girdles on stereograms (Hoy and others, 1962).

Ductile Shear Zones

Ductile shear zones are of major significance to the emplacement of salt diapirs because they probably mark zones of differential movement between adjacent spines or tongues of rock salt (Muehlberger, 1959; Kupfer, 1974, 1976). Balk (1949) and Muehlberger (1959) suggested that displacements on regional faults triggered localized flow of salt, so that Grand Saline

diapir rose by successive differential intrusions of spines and lobes, as proposed for granite diapirism (Cloos, 1936; Balk, 1937). Again, the growth of lobes may be an inherent part of the intrusion mechanism (Howard, 1971) rather than fault controlled. Vertical lobes of differential movement have also been documented in the Five Island Domes of coastal Louisiana (Atwater and Forman, 1959; Kupfer, 1968, 1974).

High simple-shear strains in ductile shear zones generate schistosity parallel to the XY principal plane of maximum flattening and rotate older structures such as anhydrite layering toward this plane (Ramsay and Graham, 1970; Ramsay, 1980). The ductile shear zones are therefore recognized in salt stocks as roughly vertical tabular zones of highly drawn out subparallel structures which pass outward into progressively less rotated structures on the edges of the shear zone. Layers trending obliquely across the shear zone may be thickened or thinned depending on their relation to the shear directions (fig. 1). The displacement between salt lobes could potentially be quantified (Ramsay and Graham, 1970; Coward, 1976; Cobbold, 1977; Ramsay and Allison, 1979; Ramsay, 1980).

Kupfer (1968) equated planar zones of halite megacrysts with former fractures or faults closed by salt creep. This inference is supported by the occurrence of coarse-grained ice in the cores of partially annealed shear zones along the margins of the Barnes Ice Cap, Baffin Island (Hudleston, 1980).

Septa of included cataclastic country rock trapped between rising lobes also differentiate the shear zones (Kupfer, 1976). The high effective-viscosity contrast between sandstone in these septa and the enclosing matrix of highly ductile rock salt provides rheologic conditions equivalent to those at much higher temperatures where quartz is highly ductile and feldspar only moderately ductile. Large extension of sandstone layers therefore leads to the formation of low-temperature mylonite (fig. 2).

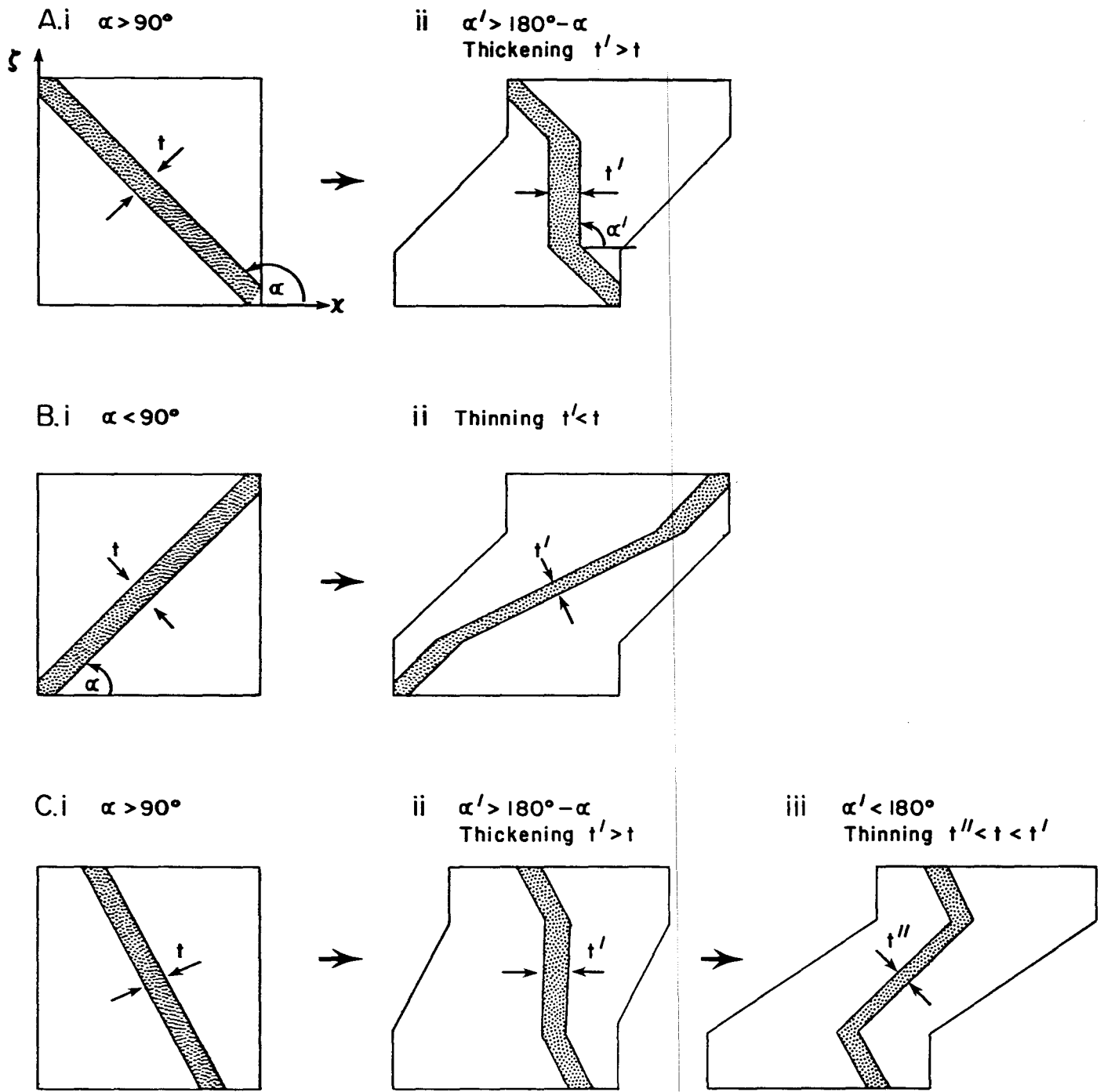


Figure 1. Homogeneous change in thickness from t to t' of a stippled layer in a matrix of similar viscosity by uniform simple shear parallel to x . (A) Thickening. (B) Thinning. (C) Thickening followed by thinning. (Adapted from Ramsay, 1980.)



Figure 2. Photograph of low-temperature mylonite comprising porphyroclasts and highly strained streaks of competent, pale, sandstone in an incompetent matrix of dark rock salt. Vertical rock face in underground mine, Avery Island Dome, Louisiana. Width of view is 0.5 m.

Fold Style in Salt Stocks

In this section the possible origins of folding within salt stocks are considered in light of current structural theory and an attempt is made to relate the shape and orientation of folds to emplacement of diapiric salt.

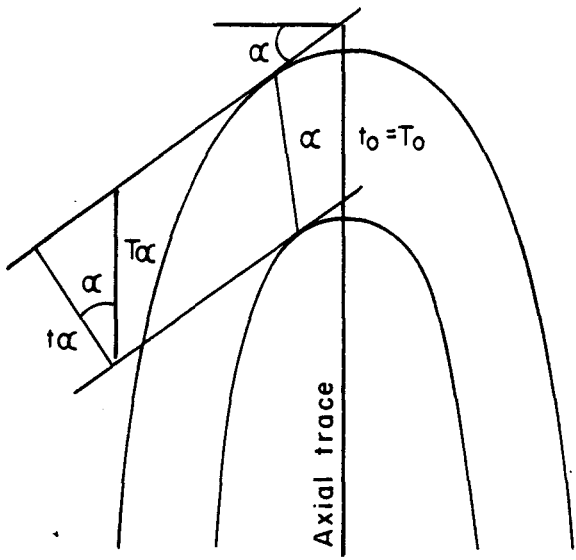
Small-scale parasitic folds in German salt mines were originally termed "seismograms" by Hartwig (1923); they were thought to represent "frozen" seismic tremors. This hypothesis cannot be said to have wide currency today, but no study has yet provided a plausible origin supported by quantitative data. Even the general fold geometry is disputed, largely because of imprecise terminology and lack of quantitative analysis. For example, Jefferson Island Dome (a "southern" dome), was described by Balk (1953) as showing close similarities with Grand Saline Dome (a "northern" dome), apart from the presence of folds in the contact zone and a possible spine at Jefferson Island. Structural elements such as the geometry and steep orientation of isoclinal, open, and closed folds are essentially alike, and were therefore deduced to have similar mechanisms of formation. Conversely Kupfer (1970) offered differences such as shear folding (in the sense of similar folding) in Grand Saline Dome and folding by "plastic flow and attenuation" in the southern domes; he thereby deduced higher temperatures of deformation in the southern domes.

In agreement with Balk (1953) there is no justification for such a distinction. Part of this confusion arose from Balk's (1949, 1953) use of the term "shear folds" to describe parasitic, lower-order folds on the limb of a larger fold. These parasitic folds are reportedly absent from Jefferson Island Dome (Balk, 1953). Shear fold is one of the many synonyms for similar fold, which may have led to the belief that similar folding is present in the northern domes but not in the southern domes. Even if this belief was correct, Kupfer's (1970) inference of higher temperatures of deformation in the southern domes on this basis would be untenable because similar folds characterize the hot, ductile core of many orogenic belts (Wynne-Edwards, 1963; Ramsay, 1967, p. 421).

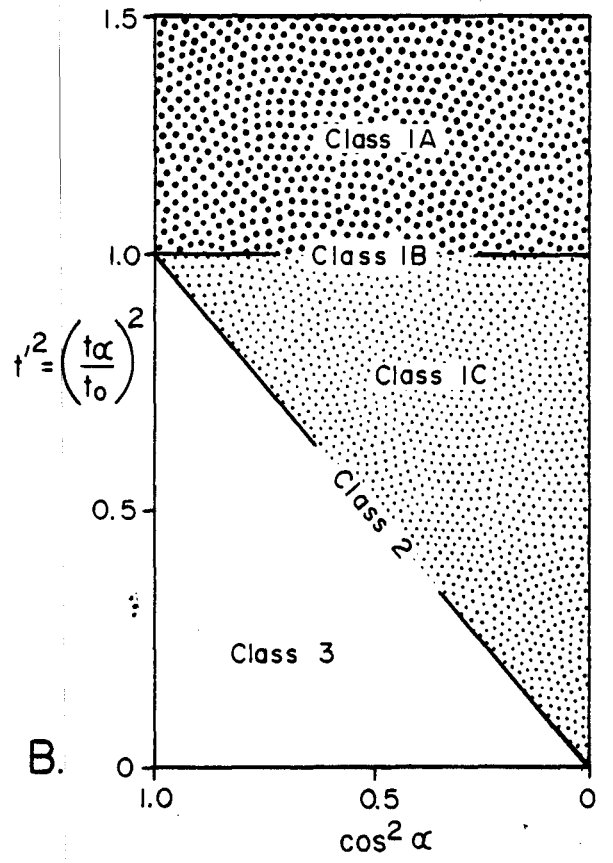
Fold profiles can be geometrically classified into two ideal members termed parallel folds, which have constant normalized orthogonal thickness, throughout the fold arc, and similar folds, which have constant normalized thickness parallel to their axial surfaces (Ramsay, 1967, p. 359-372) (fig. 3). These folds can be further distinguished by constructing lines of equal apparent dip, known as dip isogons (Elliott, 1965), connecting the inner and outer arcs of the fold (Ramsay, 1967, p. 363-366): the dip isogons of parallel folds, known as Class 1B folds, converge toward the core of the fold, whereas those of similar folds, known as Class 2 folds, diverge toward the core of the fold (fig. 3). That these are ideal shapes is indicated by the fact that the vast majority of natural folds have intermediate shapes, chiefly in Classes 1C and 3.

Fold profiles exposed in the mine roofs of Grand Saline Dome and Avery Island Dome were analyzed by the methods of Ramsay (1967, p. 359-366) and Hudleston (1973a). These folds are so close to ideal similar folds that there can be little doubt that this type of folding is present (fig. 4). Inspection of published maps (Hoy and others, 1962; Balk, 1949, 1953; Muehlberger, 1959; Kupfer, 1962) indicates that similar or subsimilar (having a shape close to, but not identical with true similar folds) folds predominate in all mapped salt domes. This is compatible with other aspects of fold geometry such as the absence of boudinaged limbs and the prevalence of limbs with attenuated orthogonal thickness. Deformation by similar folding also accords with the rheology of domal rock salt and interlayered disseminated anhydrite. Similar folding has been called "passive" because the layering is merely a marker surface with negligible mechanical control or anisotropy (Donath and Parker, 1964). Similar folding takes place in rocks that are highly ductile (such as those composed of evaporite minerals), but which have insignificant contrasts in effective viscosity between layers (Biot, 1965; Hudleston, 1973b). Anhydrite contents of the layered rock salt vary generally less than 5 percent, locally up to 30 percent (Nance and others, 1979; Nance and Wilcox, 1979; Kreitler and Muehlberger, 1981; Dix and Jackson, 1982). Thus the viscosity contrast in domal rock salt examined is low, so similar folding is likely on rheologic grounds alone (Schwerdtner, 1967; Ramberg, 1981). Low viscosity

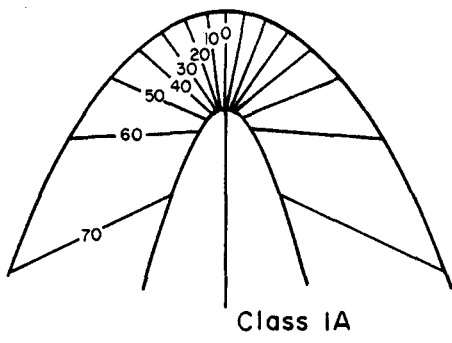
Figure 3. Fold-shape analysis and classification of folds. (A) Fold profile showing dip isogon (α) connecting points of equal dip, orthogonal thickness (t) and thickness parallel to the axial trace (T). Subscript refers to dip of tangents on folded surfaces measured from normal to axial trace. (B) Plot of $t^2/\cos^2 \alpha$ showing classification of folds on the basis of orthogonal-thickness changes. Each quarter-wavelength fold plots as a (theoretically) straight line originating at the point (1,1). (C) Representative examples of each class of folds: Class 1, dip isogons converge to core of fold; Class 2 isogons are parallel; Class 3, isogons diverge. Subclasses of Class 1 are differentiated by their $t^2/\cos^2 \alpha$ values, as in (B). (Adapted from Ramsay, 1967, figs. 7-18, 7-24, 7-25, and Hudleston, 1973a.)



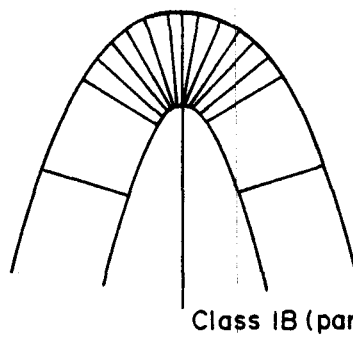
A.



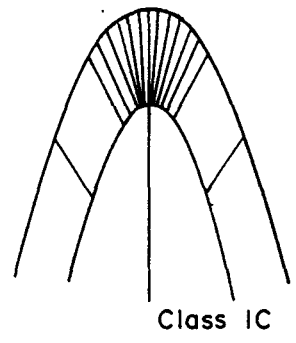
B.



Class IA

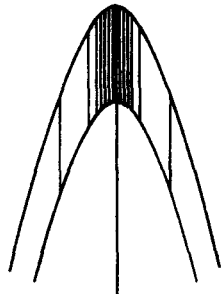


Class IB (parallel)

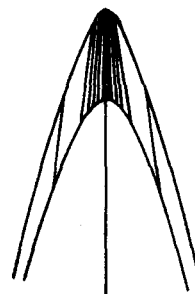


Class IC

C.



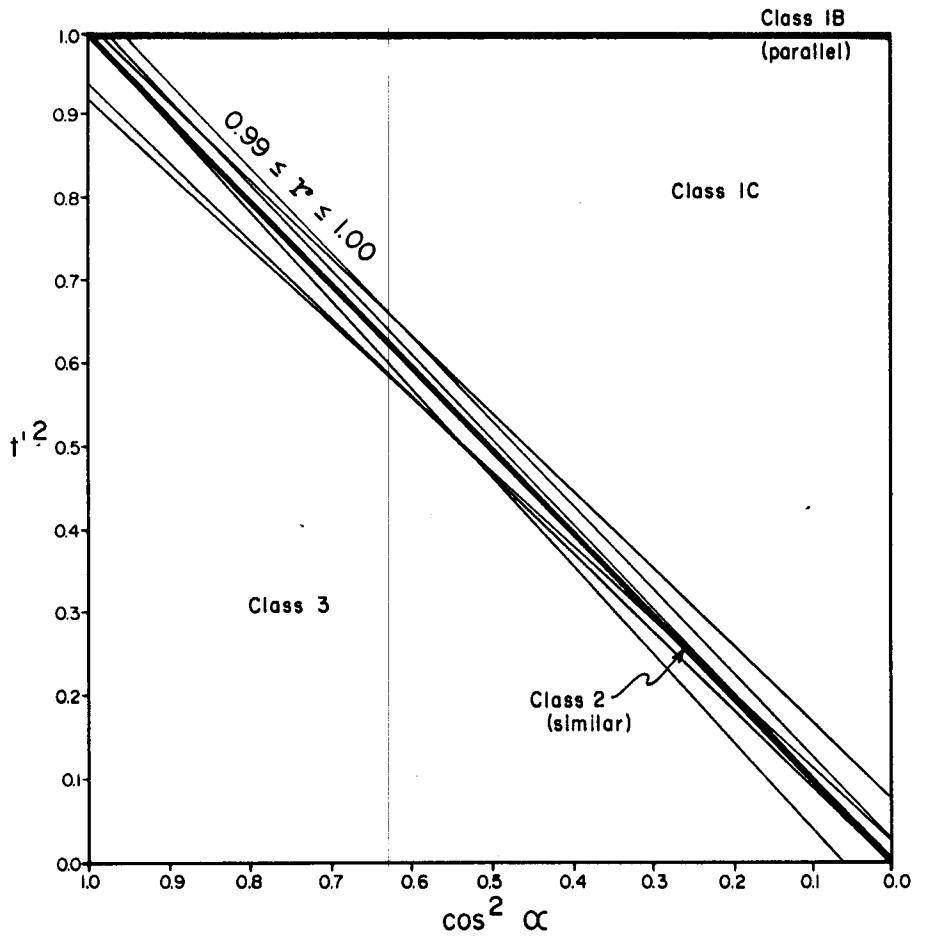
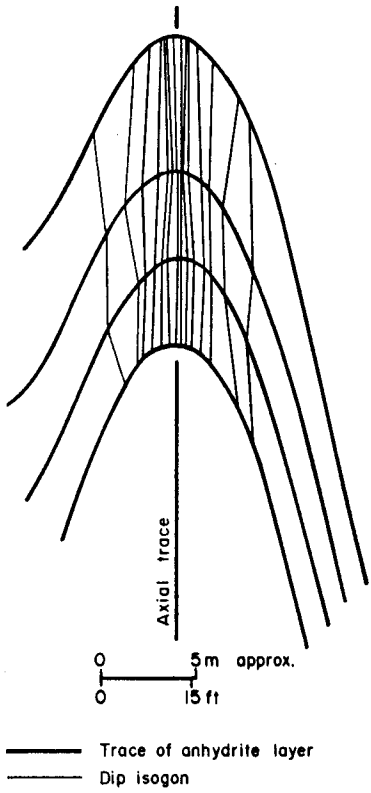
Class 2 (similar)



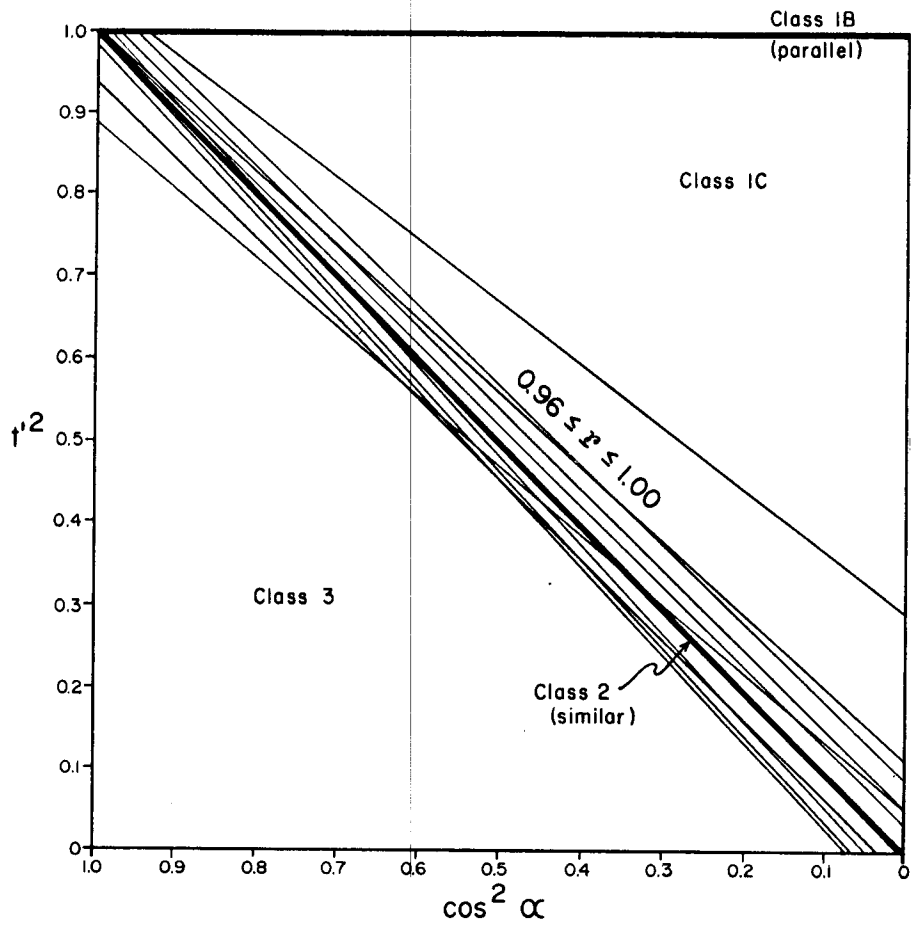
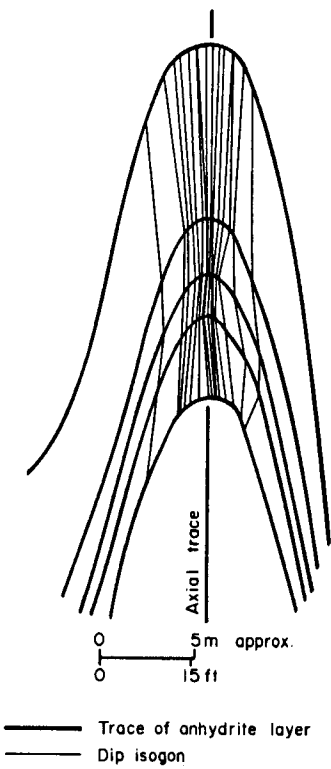
Class 3

Figure 4. Fold-shape analysis of large folds defined by disseminated-anhydrite layers in underground salt mines in Grand Saline Dome, East Texas, and Avery Island Dome, Louisiana. Left, fold profiles showing dip isogons (Grand Saline example from Muehlberger, 1959, Plate 5). Right, $t^2/\cos^2\alpha$ plots of 16 quarter-wavelength folds. Each plot is represented by a linear regression line. The high correlation coefficients (r) indicate close conformation to ideal folded surfaces. The positions and, more importantly, the slopes of these regression lines are those of similar folds.

GRAND SALINE DOME



AVERY ISLAND DOME



contrasts also characterize glacial ice containing layers of entrained dirt and bubbles; similar folding is by far the dominant fold style in such glaciers (Wegmann, 1963; Ragan, 1969; Hudleston, 1976, 1977).

Mechanics of Similar Folding

The only concept that satisfactorily explains the formation of true similar folds is that of differential simple shear acting across a layered structure in the rock and translating it by variable amounts, thereby inhomogeneously deforming the layers (Carey, 1962; Wynne-Edwards, 1963; Ramsay, 1967, p. 423). The shear surfaces that allow this differential translation can be infinitely close, such as viscous shear surfaces, or separated to form step-like discontinuities, separating microlithons or Gleitbretter.

In the case of similar folding by viscous shear (flow folding) the surfaces of viscous flow are termed flow surfaces; their traces in two dimensions are known as flow lines or displacement vectors (fig. 5). The geometry of similar folds was perceptively reviewed by Carey (1962) who made the following generalizations.

- 1) The axial trace of a fold is parallel to the flow lines.
- 2) Provided the flow lines are parallel, the thickness of a layer measured in the direction of flow remains constant, despite extreme orthogonal attenuation of layering on the fold limbs and thickening in the hinge zone.
- 3) The shear direction (parallel to the flow lines) is unrelated to the orientation of the layering, which acts merely as a passive marker distorted by differential shear. Consequently fold hinges can form within the shear surface at any angle to the shear direction.
- 4) Similar folds only disclose differential shear that is not parallel to the layering.
- 5) Similar folds do not uniquely imply either shortening or extension normal to the axial surfaces. Extreme contortion can accompany zero bulk strain normal to the axial surface.

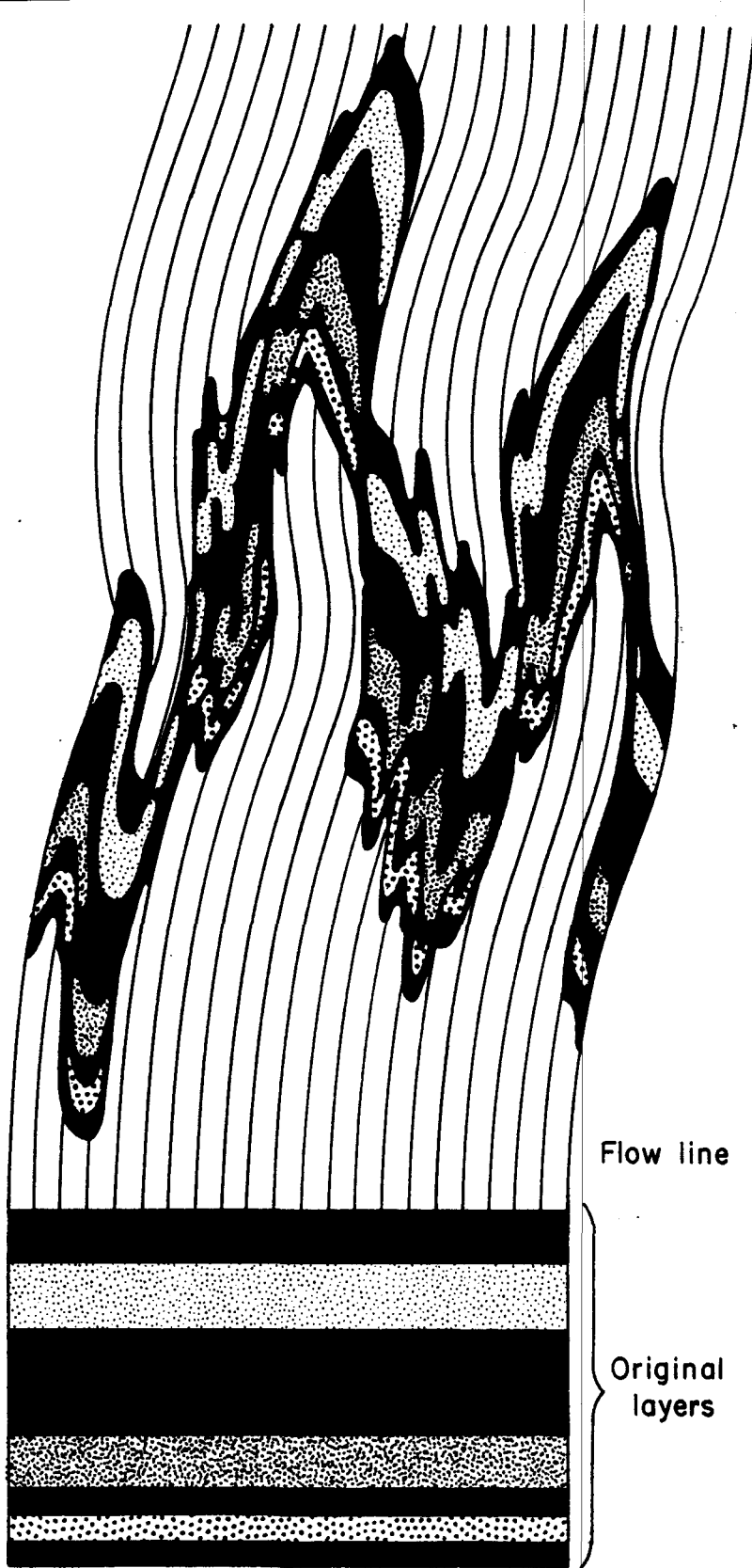


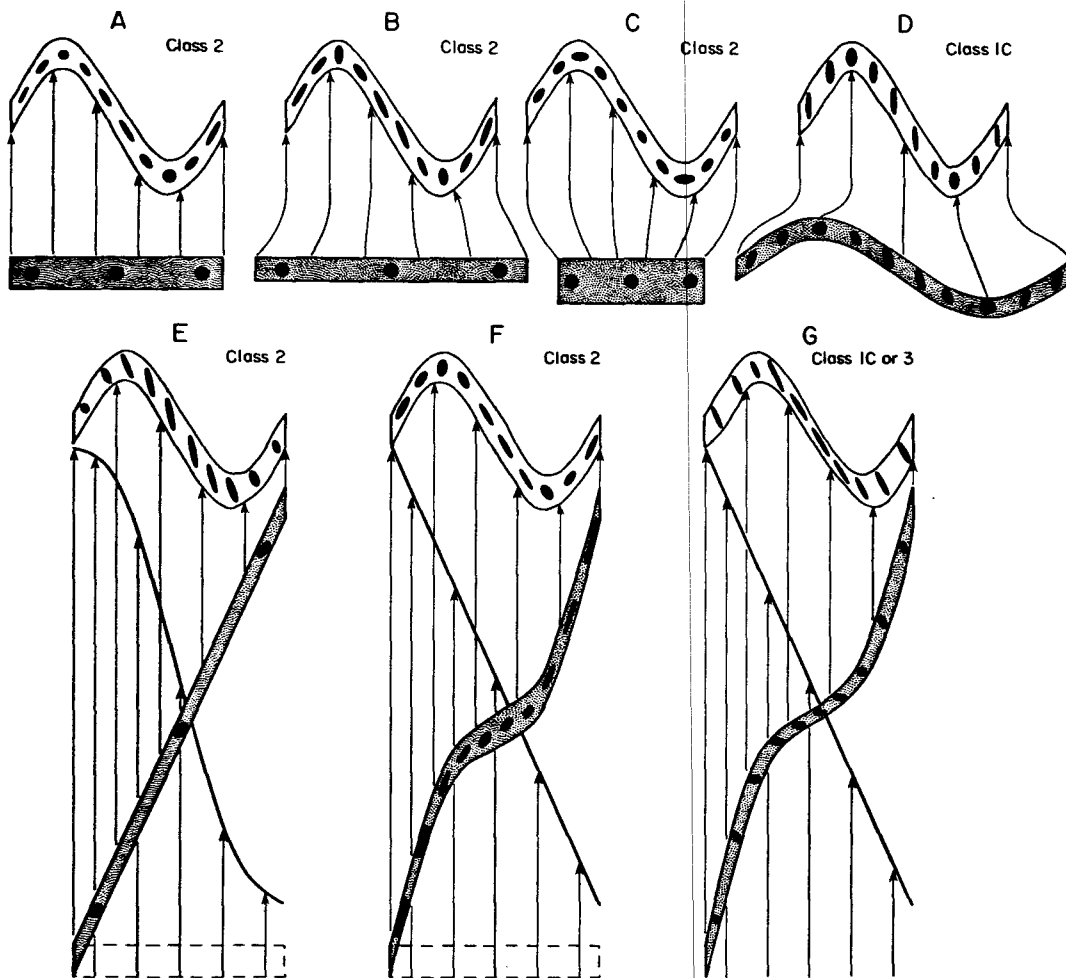
Figure 5. The appearance of ideal similar folds formed by differential simple shear of layers along parallel flow lines (flow surfaces in three dimensions). Layers act merely as passive markers with no mechanical influence. Strain is zero along axial traces, which are parallel to the flow lines. Limbs show apparent attenuation in terms of their orthogonal thicknesses, but limb thicknesses measured parallel to the axial traces are constant. Limbs are not boudinaged, and there is no shortening normal to the flow lines. (After Carey, 1962.)

Similar folds defined by medial moraines in glaciers suggest that flow lines can both converge and diverge (Washburn, 1935; Sharp, 1958; Holmes, 1965, figs. 463 and 464). Convergence or divergence of flow lines causes the thickness of the folding layer to increase or decrease, respectively, in the direction of flow (Ramsay, 1967, p. 430-431).

The orientation of an initially planar layer relative to the flow lines controls the final form of the fold. The simplest and most frequently cited case is that where the layer is perpendicular to the shear direction (fig. 6A). After differential shear, ellipse major axes define a fan that diverges toward the core of the fold. If a homogeneous flattening normal to the axial surface (i.e. converging flow lines) accompanies or follows this type of folding, a similar fold with less strongly divergent strain ellipses is formed (fig. 6B). Diverging flow lines produce a similar fold with strongly divergent strain ellipses (fig. 6C). Subsimilar, Class 1C, folds can form by superimposing very high flattening strains ($X:Y > 10:1$) on Class 1B buckle folds (Flinn, 1962; Ramsay, 1967, p. 411-415; Hudleston, 1973a; Hudleston and Stephansson, 1973). The resulting internal strains (fig. 6D) depend on the exact mechanism of buckling but will generally correspond to slightly converging strain ellipses (e.g., Dieterich, 1970; Anthony and Wickham, 1978). This mechanism for producing subsimilar folds satisfactorily explains a feature that is unaccounted for by the differential shear models outlined above: the apparent periodicity of many similar-fold trains. This periodicity would be initiated by the buckling process. However, buckling may be limited in rocks with low contrasts in effective viscosity like rock salt or ice and cannot explain the formation of true similar folds.

A further objection to the models of similar folding in fig. 6A-C is that they require an unlikely systematic reversal in the sense of shear across every axial trace. No satisfactory mechanism for producing the necessary heterogeneities in flow has been suggested. However, if a layer is initially oriented in the opposite direction to the shearing motion, heterogeneous shear with a single sense can produce a similar fold if the layering is initially planar and of constant thickness (fig. 6D) (Ragan, 1969). Homogeneous simple shear acting on a gently

Figure 6. Mechanisms for the formation of similar (Class 2) and subsimilar (nearly similar) folds. Folds with the same shape (e.g., A, B, C, E, and F) have different internal strains (diagrammatically shown by black strain ellipses) because they are formed by different mechanisms. Models A, B, and C show simple shear acting on previously unstrained layers: A, zero tangential (parallel to original layer) elongation; B, tangential shortening; C, tangential extension. D, subsimilar fold formed by homogeneous tangential shortening acting on a weakly buckled flexural fold (Class 1B parallel fold). Models A-C require unlikely reversals of shear sense across every fold axial trace. Models E-G are more realistic because they do not require reversals of shear sense. Model E shows differential simple shear (curved shear profile) acting on a stippled planar layer (which may have undergone a previous episode of uniform simple shear oriented in the opposite direction to the shear profile, as shown). Model F shows uniform simple shear (straight shear profile) acting on a layer of constant T thickness previously deformed by differential simple shear of constant shear sense. Model G shows uniform simple shear acting on a layer of constant t thickness previously deformed by flexural buckling. (E adapted from Ragan, 1969, F and G adapted from Hudleston, 1977.)



EXPLANATION

-  Folded layer showing internal strain
-  Original layer showing internal strain
-  Original layer before first simple shear
-  Shear profile
-  Flow line or displacement vector

undulating layer oriented in the opposite direction to the shearing motion will also produce similar folds if the thickness of the undulating layer is constant parallel to the shear direction (fig. 6F) (Hudleston, 1977). More generally this thickness will not be constant (as in buckle folds) and subsimilar folds will result (fig. 6G). Significantly, minor undulations do not require formation by buckling. They form by deflection of moving ice or rock salt over bedrock irregularities in the soles of glaciers (Hudleston, 1976; Talbot, 1979, 1981). Hudleston (1976) demonstrated by mathematical modeling how very slight upward deflections of the layering across the flow surfaces of the ice became magnified by further glacial flow so that isoclinal, recumbent folds form distally. In salt domes, primary heterogeneities such as a slightly irregular floor to the evaporite unit, or facies changes within the evaporite unit, could deflect flow lines sufficiently to initiate folds. These folds would later be modified by simple shear to form the spectacular similar folds mapped inside salt stocks.

Formation of Folds and Interference Structures in Salt Stocks

Having surveyed mechanisms capable of generating similar and subsimilar folds, we are now in a position to relate the formation of these folds to the emplacement of salt diapirs. The basic flow pattern in diapirs has been known since the experiments of Escher and Kuenen (1929), who suggested the popular analogy of raising several horizontal sheets through a horizontal ring. The flow circulation in a diapir has the form of a toroid: the diapir occupies the hole in the doughnut (Carey, 1961). Thus flow is initially centripetal in the source layer, upward in the diapir trunk, and centrifugal in the overhang region of the diapir. If the source layer is inclined, as on the dipping margins of a basin, or is wedge-shaped, model diapirs preferentially overhang the downdip or thinner side (Talbot, 1974, 1977).

In the source layer at the onset of doming, convergent flow toward the root of the diapir causes a volume element of salt to be lengthened parallel to the converging flow lines and shortened normal to the flow lines in a horizontal plane; that is, radial lengthening and tangential shortening (Ramberg, 1981, p. 309). Viscous drag along the upper and lower

boundaries of the salt layer induces additional shear strains. In the peripheral parts of a salt pillow or in the base of a diapir, flow surfaces are parallel to horizontal bedding, so no folds are formed. As salt then moves inward, it becomes subject to several types of stresses by three mechanisms, each of which can cause different folding:

1) Shear stresses induced by upward flow (fig. 7A): As flow surfaces curve upward toward parallelism with the axis of the salt structure, simple shear acts across the bedding and progressively rotates it toward parallelism with the shear surfaces. This folding on horizontal axes, about increasingly steeper axial surfaces, forms only the major structure by simple upward deflection.

2) Normal stresses induced by convergent flow (fig. 7B): These stresses act parallel to the layer to cause tangential shortening. Such stresses acting on a rheologically isotropic medium cause homogeneous shortening without folding. However, a weak planar anisotropy is imparted by layers of sparsely disseminated anhydrite in the rock salt. This results in the formation of gentle buckle folds of parallel style; amplitude/thickness ratios are low because of the low viscosity between the disseminated-anhydrite layers and the pure rock salt.

3) Shear stresses induced by boundary effects of the salt body (fig. 7C): As observed in salt glaciers and ice glaciers (Talbot, 1979, 1981; Hudleston, 1976, 1977), an irregular floor to the salt source layer could trigger the formation of intense, recumbent folding with similar style. Such structures could also be formed by irregularities in the upper contact of the salt source layer.

Mechanism 1 gives rise to the gross structure of a salt diapir and rotates minor structures formed by other mechanisms to a vertical position. Mechanisms 2 and 3 are examined in turn to assess how this rotation affects the form and orientation of minor structures.

Convergent laminar flow superposed on weak buckling: As the gentle buckle folds formed by mechanism 2 are drawn toward the axis of the growing salt structure, they are modified by centripetal and upward flow (fig. 8). Converging and steepening flow paths deform the buckles

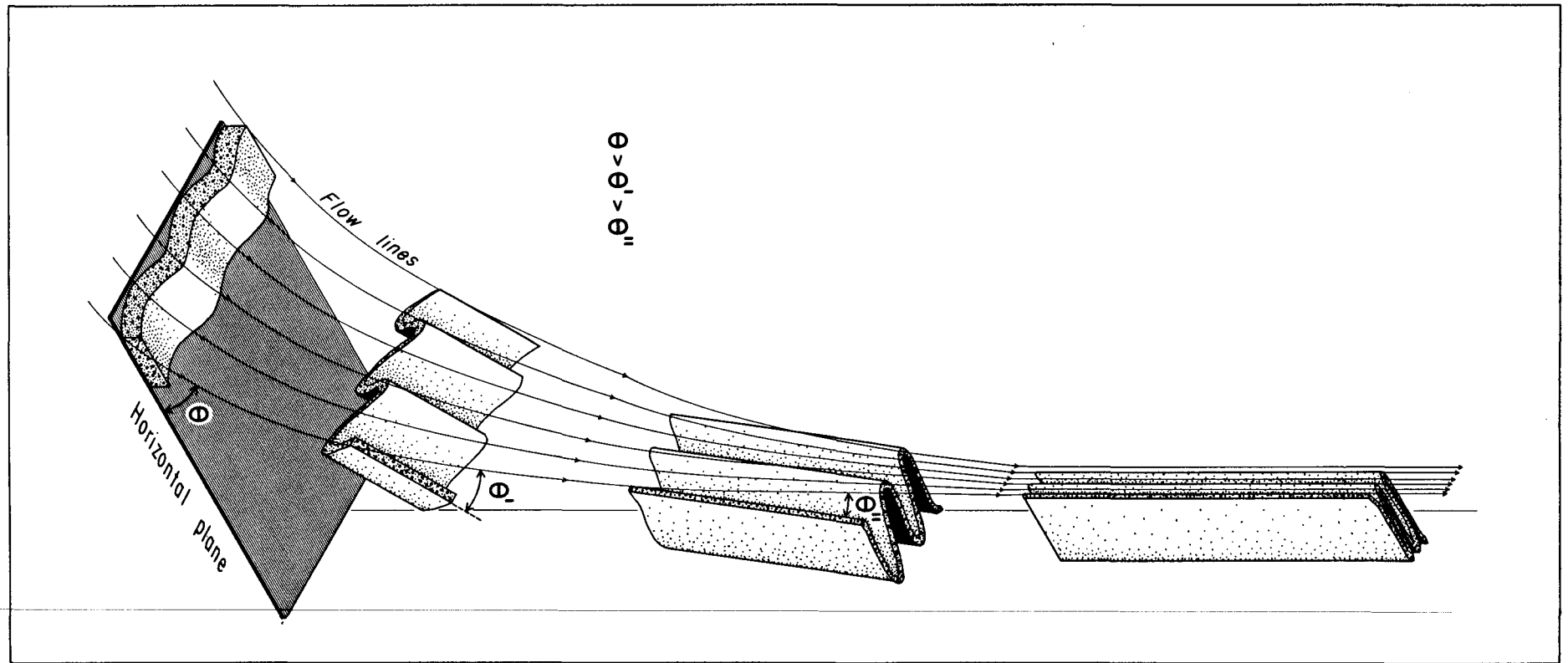


Figure 8. Rotation and axial constriction (by the mechanism in fig. 7A) of initially open, upright, horizontal folds (folded by the mechanism in fig. 7B) to form isoclinal, vertical folds by upward flow of salt into the trunk of a diapir.

by: (1) rotating fold hinges to steeper plunges; (2) reducing wavelength; (3) increasing amplitude; (4) causing extension parallel to the fold hinges. Although this convergent flow can be heterogeneous at any scale its predominant effect is that of homogeneous strain, thereby converting the parallel folds to subsimilar Class 1C folds (Ramsay, 1967, p. 411-415; Hudleston, 1973a); these folds will become virtually similar (Class 2) with considerable shear flow up the trunk of a diapir. The folds plunge near-vertically at their limit.

Refolding and rotation of upright to recumbent folds: What is the result of combining the effects of convergent flow and weak F2 buckling on pre-existing recumbent F1 folds formed by mechanism 3? The F1 hinges and axial surfaces are deformed and rotated by the superposed strain (fig. 9B). The resulting interference structure is eventually dominated by the F2 folds (fig. 9C). Whether F1 folds are recognized in a horizontal cross section such as a mine ceiling depends on their orientation. If the F2 folds have subvertical orientation, so that the cross section is parallel to the F1 fold hinges, no interference structures would be visible (fig. 9D). Way-up structures such as graded anhydrite layering would reveal multiple F1 axial traces even though no F1 fold hinges were visible. Nevertheless in oblique sections, caused by non-vertical plunge of the F2 folds, the familiar closed crescentic interference patterns (Ramsay, 1967, Type 2; Thiessen and Means, 1980, Case N) would be visible (fig. 9E). Other interference patterns arise from other oblique sections through this structure (fig. 9F, G), including hook-shaped patterns.

The orientation of each fold generation during progressive rotation has been calculated and depicted in figure 10, both in stereographic form and on the dip-pitch-plunge (DPP) ternary diagram of Rickard (1971). The F2 folds maintain their upright attitude as they rotate from upright horizontal to vertical in their ascent up the diapir trunk (X symbols in fig. 10). In contrast the F1 folds, which are initially close to recumbent, take on a wide range of attitudes during refolding and rotation, ranging from horizontal to inclined plunging (stippled field in DPP diagram). But they never attain a vertical orientation. All F1 folds tend toward an upright

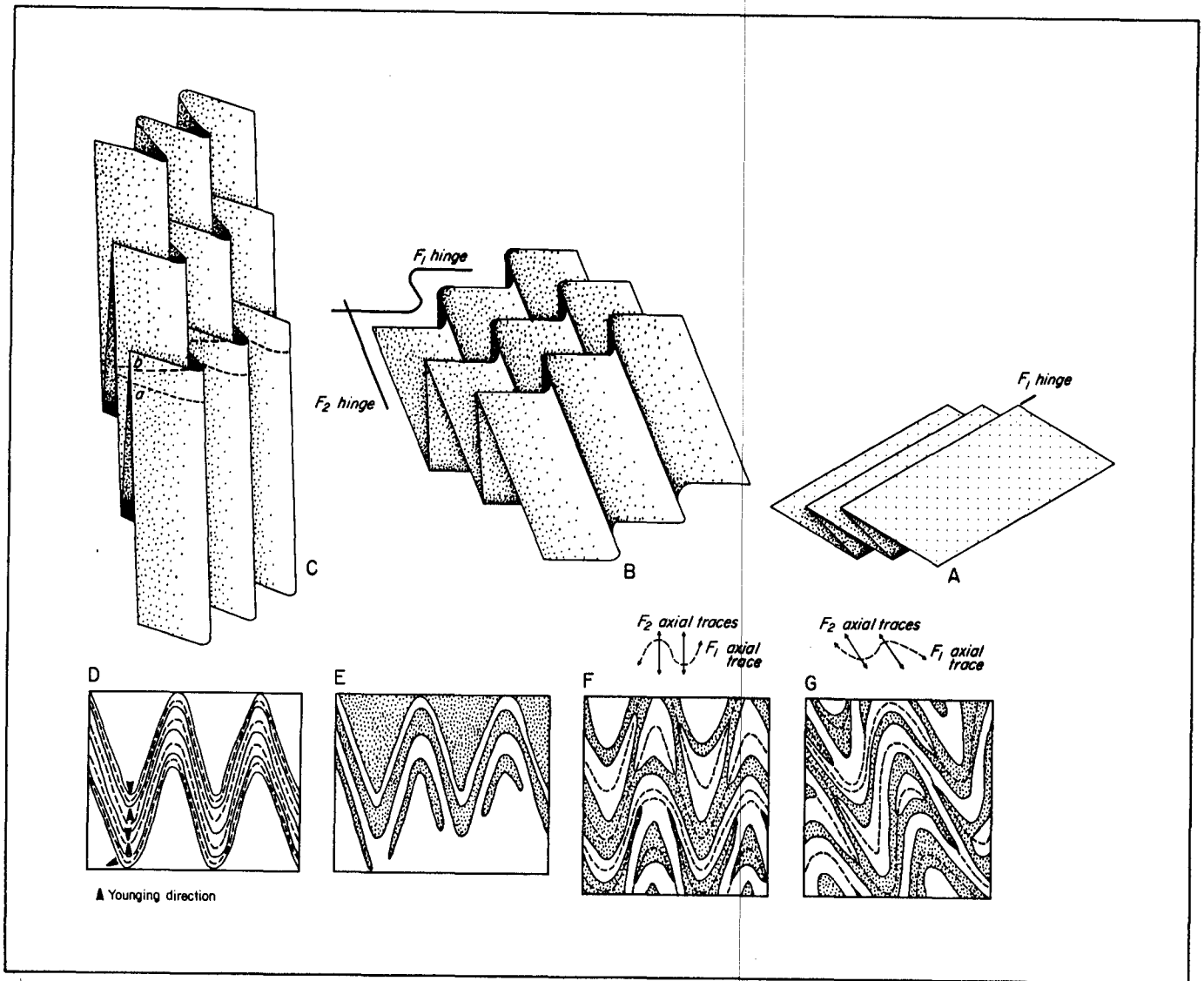
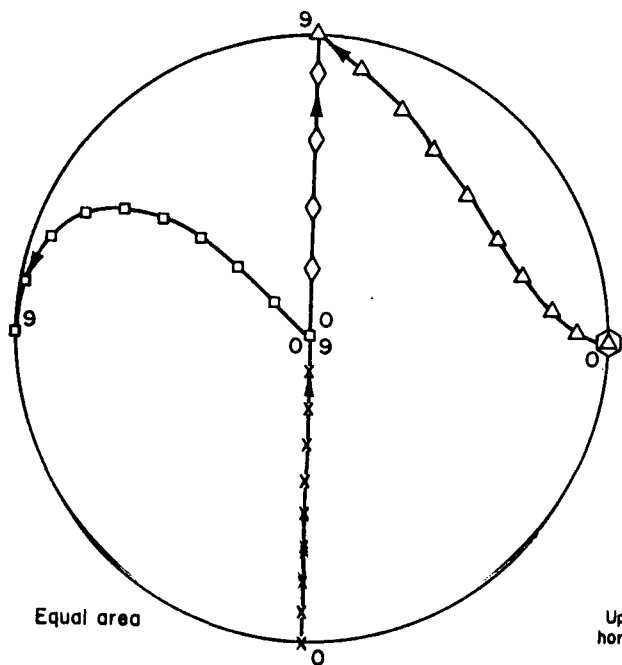
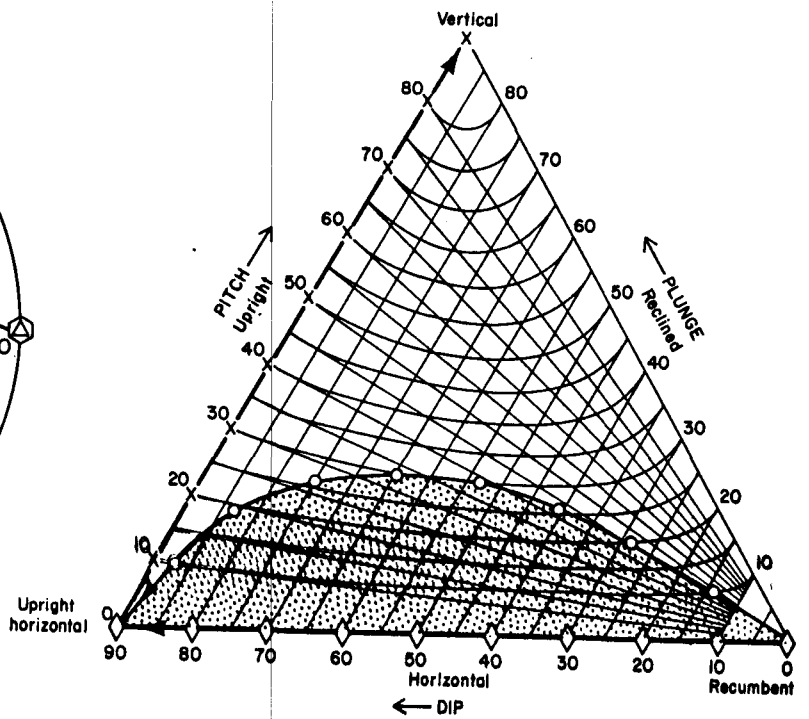


Figure 9. Refolding and rotation (by the mechanisms in fig. 7A, B) of originally recumbent F1 folds (formed by the mechanism in fig. 7C) during flow of salt into and up the trunk of a diapir. (A) Original F1 folds. (B, C) Progressive F2 refolding analogous to Ramsay's (1967) Type 2 interference. (D) No interference patterns, apart from reversal of younging directions, are visible in cross section plane a in figure C, normal to F2 hinges. (E) Characteristic crescentic patterns visible in slightly oblique cross section plane b. Reversal of younging would also be present. (F, G) Oblique cross sections through computer modeled, orthogonally superposed folds (case N, Thiessen and Means, 1980) of similar geometry to those in figure C. Hooks and crescents predominate.



EXPLANATION

- △ Hinge line of F_1 fold on limb of F_2 fold
- Hinge line of F_1 fold in hinge of F_2 fold
- Pole to axial surface of F_1 fold on limb of F_2 fold
- ◇ Pole to axial surface of F_1 fold in hinge of F_2 fold
- x Hinge line of F_2 fold
- Pole to axial surface of F_2 fold



EXPLANATION

- Orientation of F_1 fold on limb of F_2 fold
- ◇ Orientation of F_1 fold in hinge of F_2 fold
- ▨ Orientation of all F_1 folds after refolding by F_2 fold
- x Orientation of F_2 fold

Figure 10. The changing orientations of F_1 and F_2 folds during F_2 refolding and rotation shown in figure 9. Left, stereographic projection, right Rickard's (1971) dip-pitch-plunge diagram; curved lines in grid are for pitch. F_2 folds rotate from upright (axial planes) horizontal (hinges) to vertical along a single path with upright axial planes. F_1 folds rotate from recumbent to upright horizontal along an infinite number of paths (stippled area) ranging from horizontal hinges (diamond symbols) to moderately inclined (axial planes) plunging (hinges) (circle symbols). F_1 folds cannot be rotated to a vertical position in the model shown in figure 9.

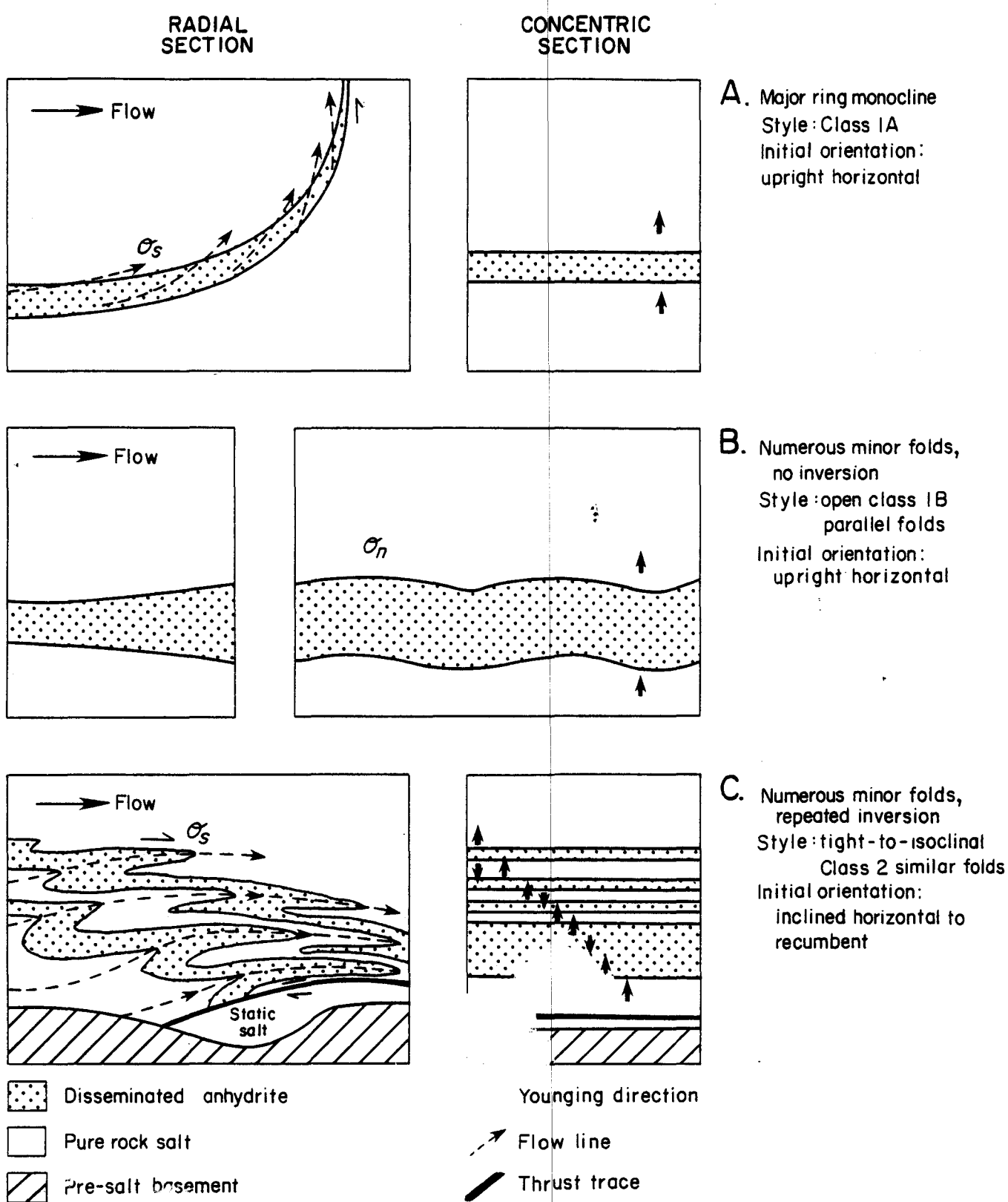


Figure 7. Models for generating folds during centripetal flow of rock salt into a salt diapir. Diapir axis lies to right of each radial section; flow in concentric section is normal to paper. (A) Shear stresses (σ_s) induced by upward flow. (B) Normal stresses (σ_n) induced by convergent flow. (C) Shear stresses (σ_s) induced by lower boundary effects. (C adapted from Talbot, 1981, Kuh-e-Namak salt glacier, Iran.)

horizontal attitude with extreme strain. Thus vertical folds cannot be formed by rotation of the F1 folds shown in figure 9A.

Notwithstanding this conclusion, vertical folds could be formed if the F1 folds were not cylindrical, as depicted in figure 9A, but had nonlinear fold hinges, as shown in figure 11 (left). The subtle culminations in the original F1 folds would be greatly amplified by convergent upward laminar flow during F2 to become tongue-like folds with circular, elliptical, crescentic, or involute cross sections and vertical fold hinges (fig. 11, right).

It is therefore probable that inclined horizontal F1 folds form tangential to salt stocks by centripetal salt flow over basement irregularities, and that culminations in their noncylindrical fold hinges can be magnified into tonguelike vertical folds during constrictive passage up the trunk of a diapir. Accordingly, as a test for this hypothesis, the resulting interference patterns should be visible in salt mines. They are. Closures, or eyed folds, in cavern roofs mapped by Balk (1949, 1953), Muehlberger (1959), Hoy and others (1962), and Kupfer (1962, 1968) are the cross sections through these structures. Balk and Muehlberger inferred that the closures in Grand Saline Dome were cross sections through the culminations and depressions of closed interference structures with "pipelike form" although they did not attempt to analyze the formation of these "pipelike" folds. A corollary of this hypothesis is that above or below these closures the plunge of the fold hinges must locally decrease to zero. Kupfer (1962) proposed another explanation for Weeks Island Dome; he inferred that the closures formed by partial fusion of isoclinal fold limbs.

The writer supports the model of tonguelike folds formed by vertical elongation of fold structures. Tonguelike folds, now generically called sheath folds, have been widely reported from blueschists, layered marbles, and mylonite (Quinquis and others, 1978; Minnigh, 1979; Mukhopadhyay and Sengupta, 1979; Cobbold and Quinquis, 1980; Henderson, 1981). The three-dimensional geometry of these sheath folds is known from serial cross sections, and the mechanics of their formation has been studied by means of theoretical and experimental

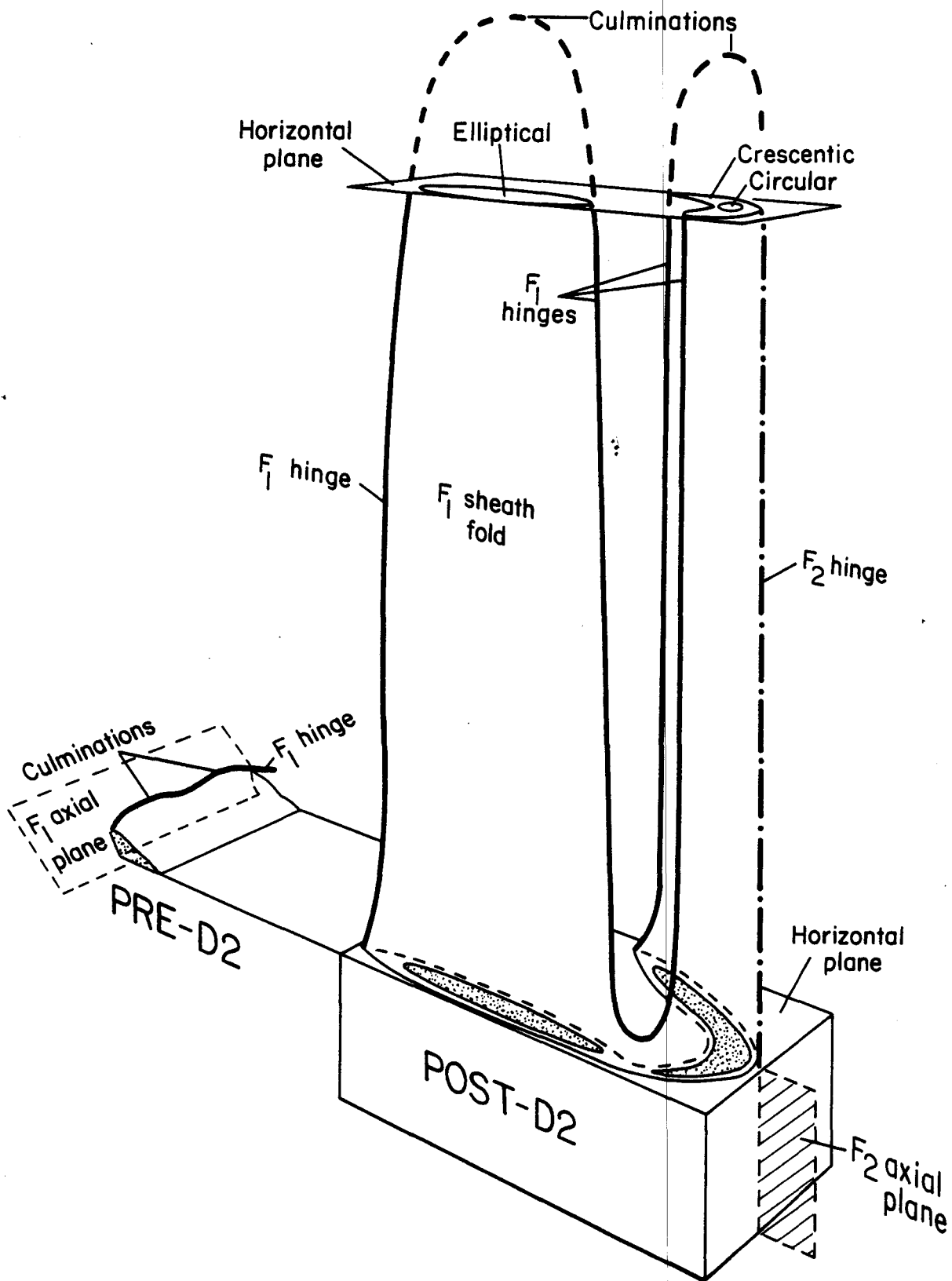


Figure 11. Model for the formation of vertical and near-vertical F2-F1 sheath folds (right) during D2 deformation by intense constriction of originally upright or inclined, noncylindrical folds (left) during diapiric rise of rock salt. F1 folds on the limbs of F2 folds have elliptical cross sections, whereas F1 folds in the hinge of F2 folds have crescentic or circular cross sections. The F1 sheath folds are too noncylindrical to plot on a dip-pitch-plunge diagram, but vary from upright horizontal at the culminations to vertical down the sheath flanks.

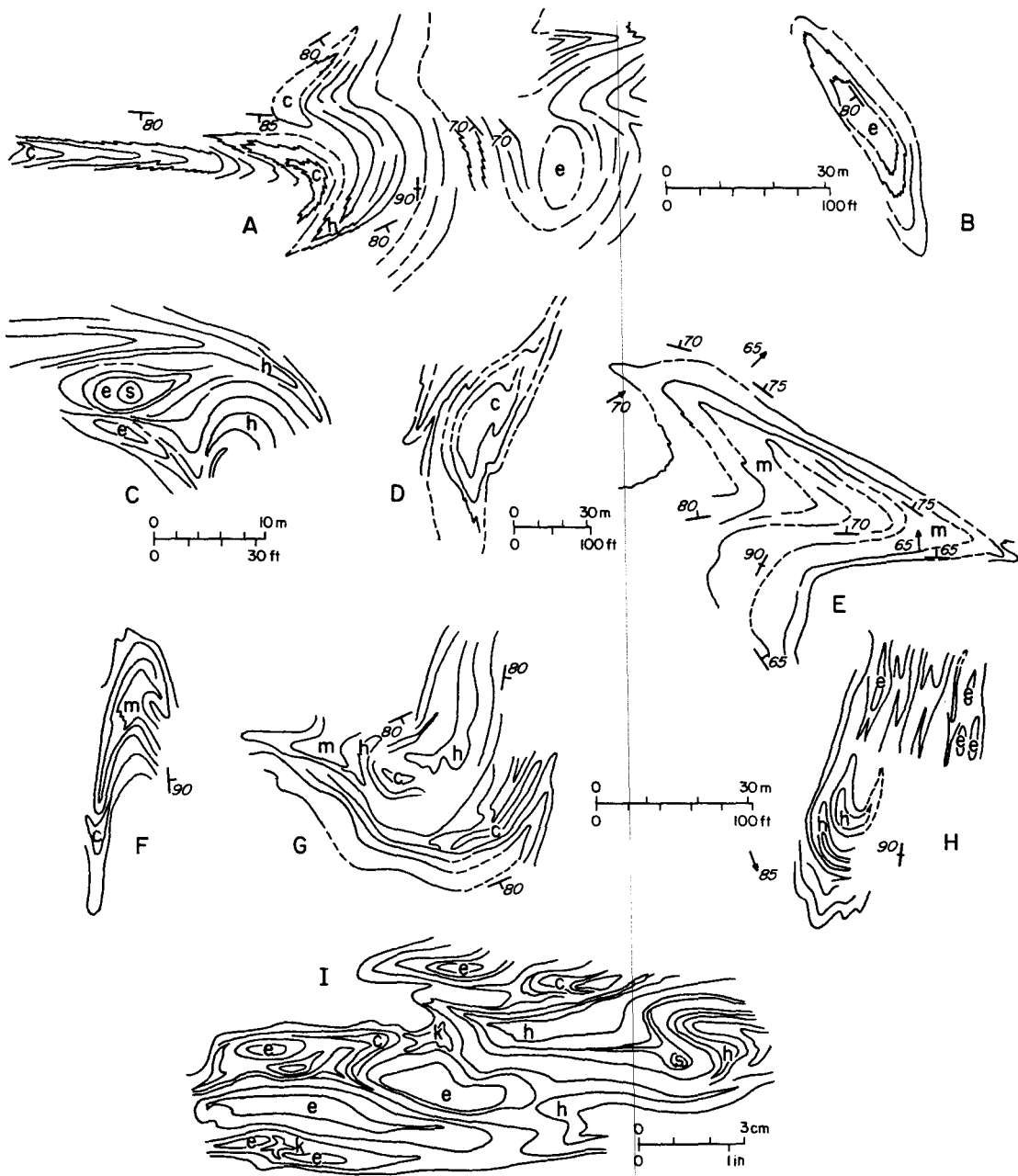
modeling. Similarities between cross sections through natural sheath folds and cross sections of salt folds are illustrated in figure 12. Note that the sheath folds in the mylonite example are about two orders of magnitude smaller than those in the salt, but their geometric similarity is striking. The most common patterns in rock salt are circles, ellipses, crescents, and hooks (fig. 12). The mushroom shapes are fairly rare. But, with the crescentic shapes, they provide the most critical evidence of all--they can only be formed by interference of folds with restricted mutual relations (Thiessen and Means, 1980). These relations are satisfied by the model shown in figure 11.

It can therefore be concluded that fold closures, mushroom shapes, and certain hook-shaped folds in horizontal sections of salt mines represent the distorted and rotated remains of F1 folds (fig. 11). These folds originally formed concentrically around the base of the salt dome as a result of perturbation of laminar flow by irregularities in the upper and lower contacts of the salt source layers (fig. 7C). These F1 folds were then carried into the trunk of the diapir by inward salt flow, where they were refolded. The majority of folds now exposed within salt diapirs are of F2 age (it should be stressed that this is a label of convenience and includes all post-F1 folding, obviously a broad category). The F2 folds originally must have formed as weak buckles trending toward the dome axis and resulting from tangential shortening during centripetal salt flow (figs. 7B and 8). These folds were rotated to near-vertical orientations (fig. 10) and stretched vertically; differential stretching would have encouraged the formation of ductile shear zones between tongues of salt rising at different rates. Where F1 folds had not previously formed, the F2 folds in the diapir trunk tend to have the following stratigraphic relations: anticlines face outward and synclines face inward; nevertheless, because of their vertical plunge these folds are structurally neutral (neither antiforms nor synforms).

Assessing Large-Scale Flow Patterns From Linear Elements

Because the trunks of active salt diapirs are regimes of intense subvertical elongation by simple-shear viscous flow, the patterns of flow can be deduced on the basis of the theoretical

Figure 12. Cross sections through large fold interference structures in the roofs of Gulf Coast dome-salt mines, illustrating six basic patterns. These patterns are postulated to be profiles of sheath folds formed by the model shown in figure 11. Except for C, all views are downward and normal to horizontal plan projections; north is to the top of the diagram. (A, B) Grand Saline Dome, East Texas, 700-ft level of Klear Mine (Balk, 1949). (C) Jefferson Island Dome, Louisiana, 1000-ft level of Jefferson Island Salt Company Mine (Balk, 1953). Oblique view about 60 degrees upward toward southwest. (D, E) Winnfield Dome, Louisiana, 811-foot level of Carey Salt Company Mine (Hoy and others, 1962). (F-H) Weeks Island Dome, Louisiana, 758-foot level of Morton Salt Company Mine (Kupfer, 1962). (I) For comparison, a profile through much smaller, but similar, sheath folds in mylonitic rocks from Vang, Valdres, Norway, probably deformed by intense simple shear nearly parallel to the layers (Cobbold and Quinquis, 1980).



EXPLANATION

INTERFERENCE PATTERNS

Closed	Open
s circle	h hook
e ellipse	m mushroom
c crescent	
k complex	

↙80 Strike and dip of anhydrite layering

↘70 Trend and plunge of lineation

behavior of linear elements within them. Fold hinges and the \underline{L} component of $\underline{L}-\underline{S}$ mineral fabrics (mineral lineation) are linear finite-strain elements. These elements rotate toward the shear direction as the rock enclosing them deforms by progressive simple shear. The greater the shear strain, the closer these elements rotate toward the shear direction, attaining parallelism in the case of infinite shear. At reasonably high shear strains, then, the orientation of lineations and fold hinges provide approximate indicators of the flow paths within salt stocks.

These flow paths are merely pathways; what is the polarity of the flow? Flow patterns within an intruding salt stock are largely conjectural. But because the diapir moves upward relative to the surrounding strata, the probability of a given unit of salt moving upward is much greater than the probability of it moving downward. Thus, the trend of a linear element indicates the azimuth of the flow path, whereas the up-plunge direction (180° from the trend) indicates the probable direction of flow. In addition, however, strike directions of anhydrite layering are also flow-path indicators. Where the layering is vertical (for practical purposes, $88-90^\circ$), fold hinges defined by the layering must be contained within the vertical plane; thus the trend of the fold hinge must be parallel to the strike of layer. Such strikes provide the flow path, but not the direction, or polarity, of flow; they are thus of less use than measurements of a linear element.

Only three salt domes contain mines with sufficiently numerous measurements of linear elements, or strikes of vertical layers, to enable flow directions to be estimated: the southeastern part of Grand Saline Dome (Balk, 1949), Weeks Island Dome (Kupfer, 1962), and Winnfield Dome (Hoy and others, 1962). The inferred flow directions and flow paths are shown for these mines in figure 13. It is readily apparent from the locality maps (fig. 13A) that only the Carey Salt Company Mine in Winnfield Dome covers a substantial part of a dome. The percentage of linear elements in the total number of control points (\underline{n}) is shown as $\underline{L}\%$ for each mine; this percentage and the density of control points enable the quality of the data to be assessed.

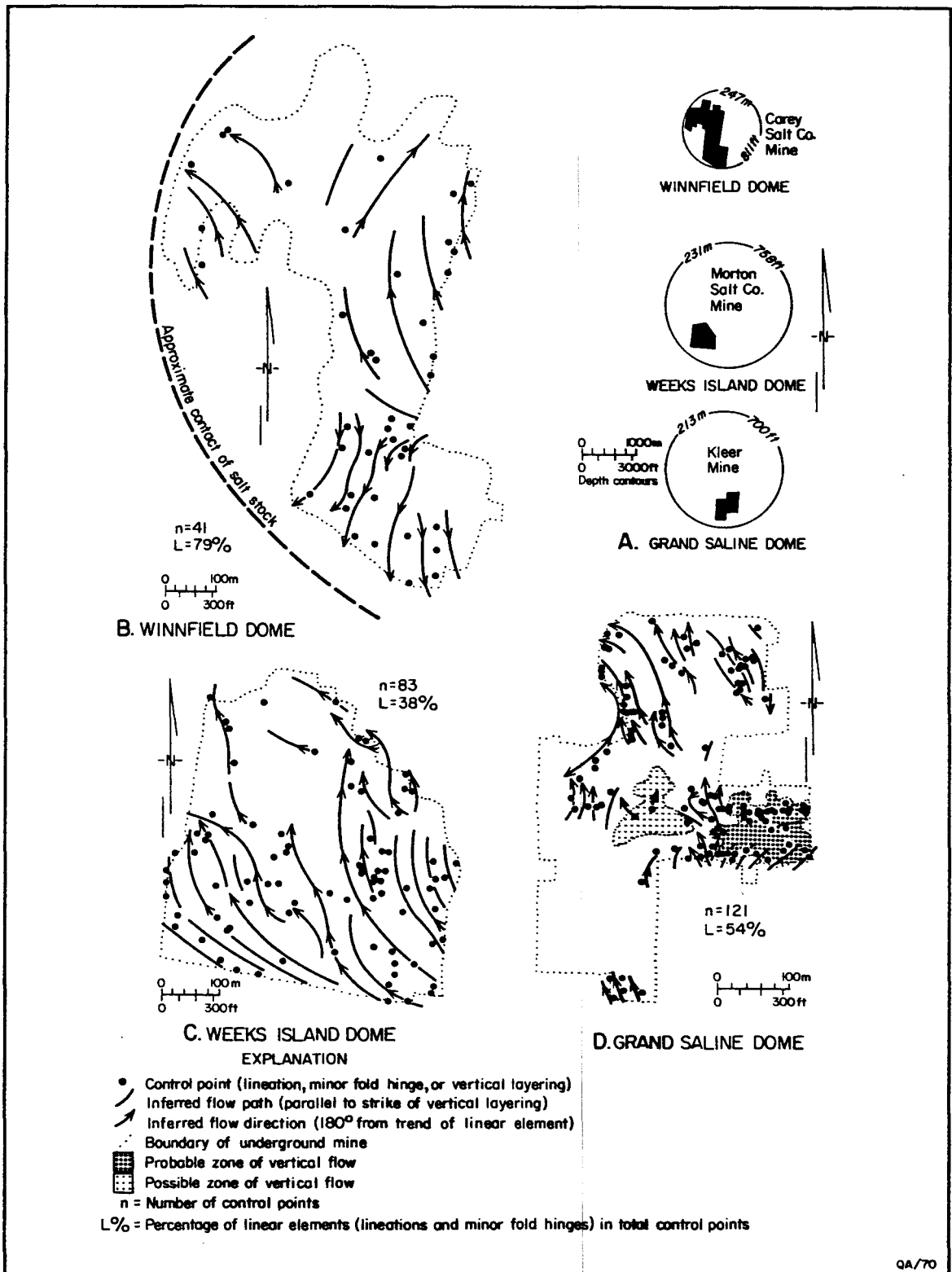


Figure 13. Maps showing inferred flow paths and flow directions of rock salt in three dome-salt mines. Flow paths have much larger vertical components of movement, but only horizontal components are shown. Data collected by Balk (1949), Hoy and others (1962), and Kupfer (1962).

The inferred flow directions indicate the azimuth of flow, but it should be stressed that the vertical component of this flow is much greater than the horizontal component shown on the maps. The inferred flow pattern in Winnfield Dome is that of flow outward from a zone in the southern part of the dome (fig. 13B). The inferred flow patterns in Weeks Island and Grand Saline Domes (fig. 13C, D) both suggest flow inward to the dome center; they thus appear to be opposite to Winnfield Dome, although the small area sampled may not be representative. The probable zone of vertical flow in Grand Saline Dome is marked by vertically plunging linear elements, and the possible zone of vertical flow is marked by an absence of planar structures. All the maps in figure 13 illustrate that linear trends (and inferred flow directions) form coherent patterns that vary far less than the seemingly chaotic strikes of layering and fold axial surfaces; the linear trends therefore impart a structural unity and are essential to an understanding of the structure and its implications to salt flow.

A more revealing way of treating the linear data is to examine the variation in plunge of these elements. The data base varies between 38 and 79 percent of the size of the previous data base because vertical dips of layering, which yield trends but not plunges, are omitted. Figure 14 shows maps of plunge isogons (lines joining points of equal plunge) drawn on the surface containing the linear elements. In order to filter out errors in the original measurements as much as possible--errors that would cause meaningless and confusing perturbations in the map pattern--a measuring error of $\pm 2^\circ$ was assumed. The assumed error is based on a study by Rondeel and Storbeck (1978), who found that in groups of 100 measurements of rotatable bedding surface, under optimum conditions, 90 percent of the poles fell within an error cone of 2° half-apical angle around the mean pole; the measurement of a linear element, which is inherently more difficult to measure, in dim light is likely to be considerably more error-prone, so the assumption of 2° error is conservative. Even so, the plunge-isogon maps show considerable consistency and smooth variations in plunge from point to point.

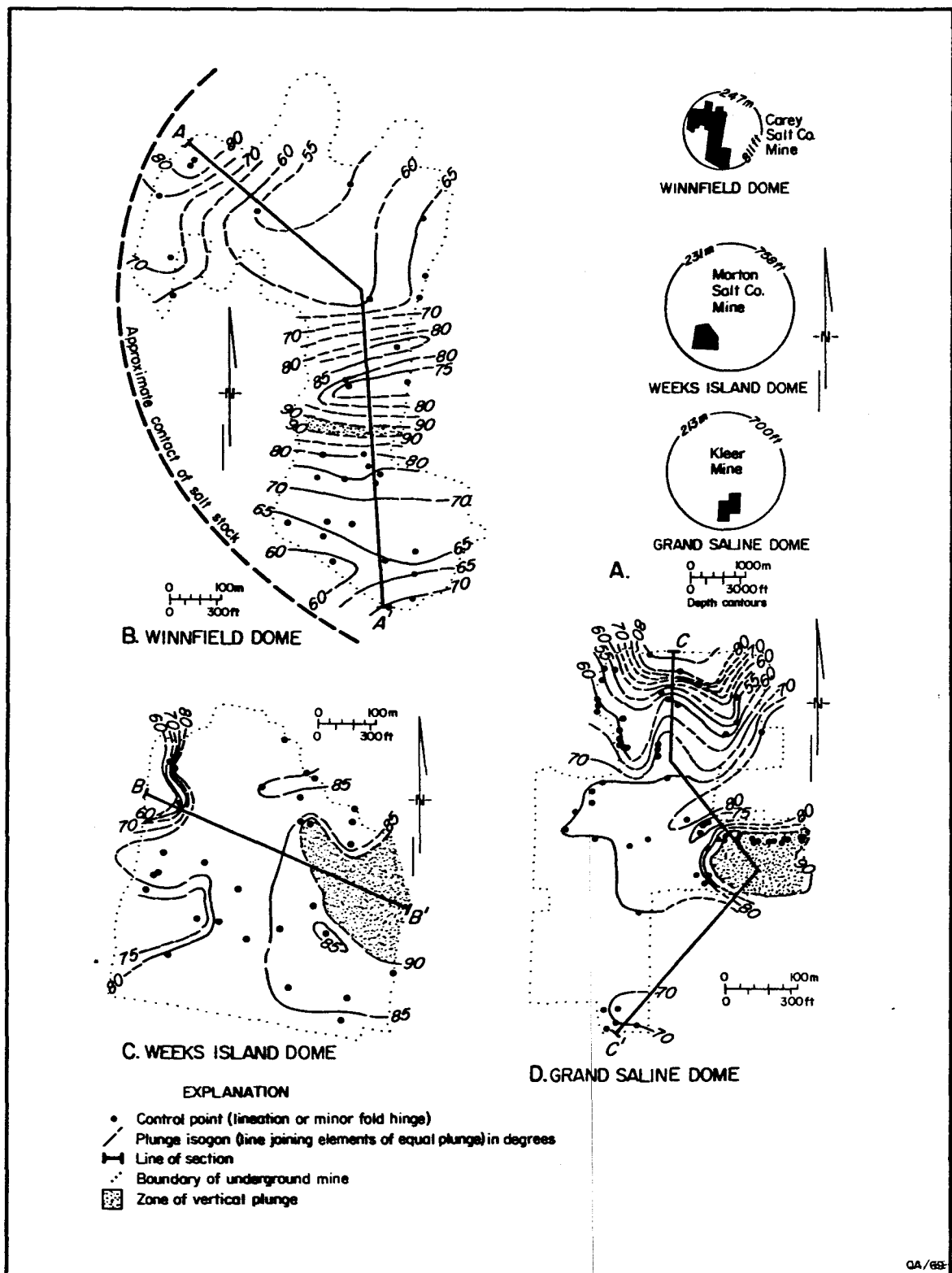


Figure 14. Maps showing plunge isogons for linear elements in rock salt in three salt-dome mines. Note the rarity of vertical plunges. See figure 13 for data sources.

How should such isogon maps be interpreted? The answer lies in deducing the most probable relation between rheid flow in a crystalline solid and the orientation of the resulting linear fabric. Two contrasting models can be considered.

The first of these (fig. 15A) is similar to that of free thermal convection in a confined aquifer (after Donaldson, 1962). The isotherms serve as the traces of marker surfaces to illustrate variations in flow velocity. The maximum-extension directions are, of course, not applicable to liquids, but correspond to the inferred directions of maximum stretching in a crystalline tectonite, subparallel to the flow paths. We are less concerned here with the nature of the driving mechanism for flow than we are with the geometry of such flow. And the essential feature of this geometry is that the zones of maximum flow correspond with the zones of steepest plunge. As in the case of all complete convection systems, rising currents are separated by sinking currents (shown by large arrows in fig. 15A). Hot convecting fluid has to go somewhere at its zenith, so it sinks because cooling increases density through contraction. Conceivably these sinking currents need not be present in a salt diapir where either active lengthening of the salt column or truncation of ground-water dissolution negate the necessity for sinking return currents.

The possibility of subsolidus thermal convection in a salt diapir is intriguing because the factors necessary (together producing a sufficiently high Raleigh number) for tongues of hot salt to rise may well be present in the deep source layers of diapirs (Talbot, 1978; Talbot and others, 1982). However, this model is speculative because so little is known of the material properties (such as kinematic viscosities and coefficients of volumetric expansion) of the rocks involved and the depth during internal flow.

The essential geometric feature of the second model--the differential-advance model (fig. 2-15B)--is that the zones of steeply plunging structures mark the borders of advancing tongues of rock, and are therefore the slowest-moving part of the advancing tongue. Paradoxically they are also the most deformed part, characterized by very high shear strains. The most compelling

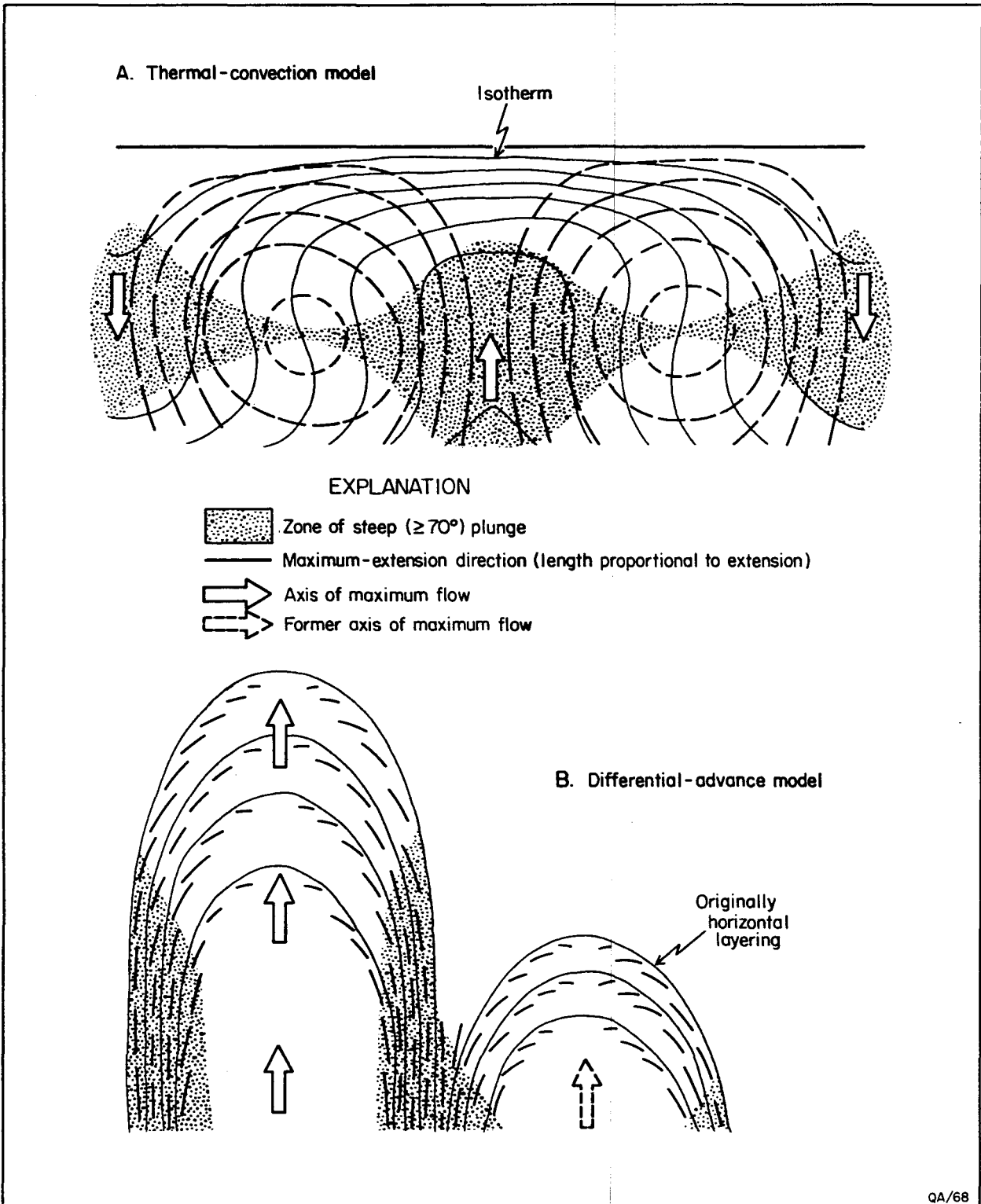


Figure 15. Models for the inhomogeneous rise of material. (A) During thermal convection, maximum upward flow occurs in zones of steep plunge. (B) During differential advance, as in glacial surges, maximum upward flow takes place beneath zones of shallow plunge; zones of steep plunge mark the borders of advancing tongues. Model B is considered more appropriate for diapiric salt.

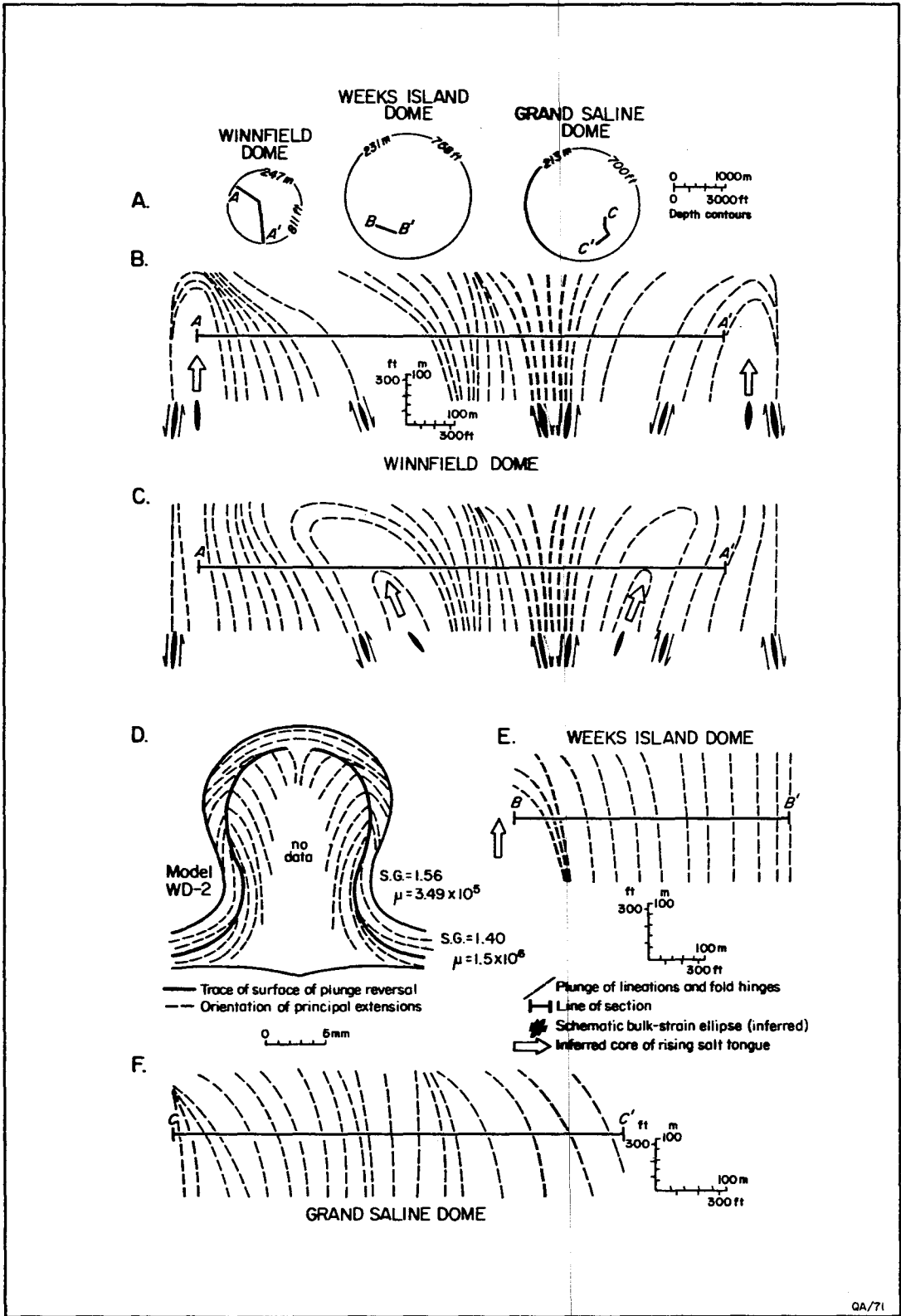
reasons for adopting this model are as follows: the ductile shear zones mapped within salt stocks, the inference that they mark the borders of salt tongues rising at differential velocities, and the field evidence for tonguelike protrusions of salt above the salt stocks (Atwater and Forman, 1959; Muehlberger, 1959; Kupfer, 1974, 1976).

This type of flow pattern is beautifully illustrated in the horizontal plane by the arcuate similar folds defined by flow-contorted moraines and "annual" bands of the Malaspina compound piedmont glacier and the Susitna glacier of Alaska (Washburn, 1935; Sharp, 1958; Holmes, 1965, figs. 463 and 464). The folding results from differential advance of lobes of the glacier during periods of ice surge, and the encountering of transverse impediments such as terminal moraines, which divert ice flow laterally (Sharp, 1958). Mapping of ice fabrics in, and mathematical modeling of, the Barnes Ice Cap, Baffin Island, shows clearly that the flow velocity decreases downward toward the sole of the glacier because of frictional drag; conversely strain rates and cumulative strains increase downward and laterally toward the glacial snout (Hooke and Hudleston, 1980; Hudleston and Hooke, 1980). Fold nappes appear to move laterally by gravitational collapse and spreading of weak rocks, advancing as tongues bordered by lower velocity, higher-strain planar zones, according to experimental models by Bucher (1956) and Ramberg (1981, figs. 9.9 and 9.10). Likewise, centrifuge models of diapirs clearly show that the zones of steepest dips and plunges correspond to the borders of rising tongues of buoyant materials (Talbot, 1974, 1977; Dixon, 1975; Ramberg, 1981, figs. 11.25 and 15.4).

In summary, evidence from all these sources suggests that whereas the flow pattern of thermal convection is appropriate in cases where a source layer is deeply buried under a high thermal gradient, the flow pattern of differential advance is not only appropriate over a wide range of crustal conditions and tectonic settings, but is also suggested by the field evidence from within and above salt domes.

The isogon maps of figure 14 may be interpreted on the basis of the differential-advance model. Figure 16 shows cross sections across the three salt domes in question, constructed with

Figure 16. Cross sections through salt domes showing major structure and inferred salt tongues based on plunge isogons in figure 14. These tongues are defined by changes in plunge of linear elements rather than by conventional layering. (A) Location of cross-section lines; see also figure 14. (B, C) Alternative models for Winnfield Dome; C is more realistic and shows two major salt tongues rising symmetrically outward. (D) Almost identical structure to C in Dixon's (1975) model WD-2, in which a surface of plunge reversal of principal extensions marks the axial surface of two symmetric tongues of diapiric material. (E, F) Cross sections for the other two domes are too short to define major structures.



no vertical exaggeration from the plunge-isogon maps. Alternative cross sections are shown across Winnfield Dome (fig. 16, B, C). Because no zones of shallow-plunging structures were mapped, the cores of rising salt tongues can be inferred to be along the margin of the dome, beyond the ends of the cross section line (fig. 16B). The junction between two tongues is inferred to be the zone of steep plunge where the sense of shear changes south of the dome center. This model is unrealistic because the two inferred tongues are placed too close to the contact zone, where frictional drag discourages any kind of rising plume, as in the glacial analogies. The alternative model places two rising tongues (marked by large arrows in fig. 16C) in the zones where Hoy and others (1962) mapped the lowest plunges (55-65 degrees); this model entails that even lower plunges may be present in these zones, but these have not been recorded. Some of the senses of shear are different in this model to those in figure 16B, but the two lobes still adjoin each other in the zone of maximum plunge south of the dome center. This inferred flow pattern is supported by a remarkable similarity with the flow pattern and strain pattern inside a model diapir of Dixon (1975). The measured orientations of principal extensions in this model are closely analogous to the orientations of the linear elements in Winnfield Dome. The principal extensions in the model also define two outward-facing inclined lobes, as inferred for Winnfield Dome (fig. 16D). The surface of plunge reversal in figure 16D roughly corresponds to the lobes of maximum flow velocity in this model. Cross sections through Weeks Island Dome and Grand Saline Dome are shown in figure 16E and F. Probably because of the shortness of the line of section in relation to the whole dome, little can be deduced from them. Nonetheless, there is a suggestion of the flanks of a salt tongue just west of cross section BB' (fig. 2-16).

Natural Strain Rates in Salt

Strain rates estimated for natural deformation of rock salt vary enormously over eight orders of magnitude, from $10^{-8}/s$ to $10^{-16}/s$ (table 1; see note a for definition of strain rate).

Table 1. Natural strain rates in the deformation of rock salt.

ENVIRONMENT	STRAIN RATE ^a (per second)
Glacial salt	
Direct measurement of flow ^b	1×10^{-11} to 2×10^{-9}
Estimated from glacial morphology ^c	2×10^{-13} to 2×10^{-8}
Diapiric salt	
Direct measurement of closure of mined cavity ^d	1×10^{-11} to 9×10^{-12}
Direct measurement of peak borehole closure ^e	3×10^{-8}
Measurement of topographic mound ^f	2×10^{-14}
Estimates from stratigraphic thickness changes around diapirs	
Overall rates, range ^g	1.1×10^{-15} to 1.1×10^{-16}
mean ^g	6.7×10^{-16}
Fastest rates, range ^g	3.7×10^{-15} to 6.2×10^{-16}
mean ^g	2.3×10^{-15}
Average growth for Zechstein Domes ^h	2×10^{-15}

a Conventional strain rate $\dot{\epsilon} = e/s$, where elongation $e =$ change in length/original length.

b Talbot and Rogers (1980), survey of markers distorted by glacial flow of Hormuz Salt, Kuh-e-Namak salt glacier, Iran. Duration of strains, 292 days (2.5×10^7 s). Maximum flow after 5 mm rainfall. Calculated shear stress, $\tau \leq 0.25$ MPa.

c Wenkert (1979), average shear-strain rates for 5 Iranian glaciers of Hormuz Salt, assuming steady-state equilibrium between extrusion and wasting, and based on erosion rates of 0.08-0.25 cm/yr. Calculated shear stress $\tau \approx 0.03$ MPa.

- d Serata and Gloyna (1959) and Reynolds and Gloyna (1960), peak rates in Grand Saline Dome (East Texas Basin) and bedded rock salt (Hutchinson Mine, Kansas). Estimated stress difference, $\sigma_1 - \sigma_3 \approx 10$ MPa. Duration of strains 10-30 yr (3.2×10^8 s to 9.5×10^8 s).
- e Martinez and others (1978), Vacherie Dome (Louisiana Interior Basin). Duration of strain, 3 months (7.8×10^6 s).
- f Ewing and Ewing (1962), Sigsbee Knolls (Gulf of Mexico abyssal plain), calculation based on salt-stock height of 1300 m (seismic section in Martin (1980). Duration of strain, 11,000 yr (3.5×10^{11} s).
- g Data from Seni and Jackson (1983), based on salt diapirs in the East Texas Basin. Overall rates are those during entire known history of diapirism (duration, 30-56 Ma, or 9.5×10^{14} s to 1.8×10^{15} s) of 16 diapirs; net rates calculated by maximum rate of deposition in salt-withdrawal basins. Fastest rates are those during particular stratigraphic periods characterized by the most rapid diapirism (duration, 1-13 Ma, or 3.2×10^{13} s to 4.1×10^{14} s) of 5 diapirs; gross rates calculated by dividing the volume of sediments in a salt-withdrawal basin by the product of the maximum cross-sectional area of the diapir and the duration of the stratigraphic interval whose sediments constitute the salt-withdrawal basin. See reference for further details.
- h Sannemann (in Trusheim, 1960), based on stratigraphic-thickness data and salt-stock height of 4 km. Duration of strain, 35-130 Ma (1.1×10^{15} s to 4.1×10^{15} s).

By comparison, the estimated rate of flow in the asthenosphere--a standard datum for steady-state geologic strain--is about $10^{-14}/s$ (Carter, 1976). Average strain rates for orogeny have also been calculated at $10^{-14}/s$ (Pfiffner and Ramsay, 1982). The wide range in halite strain rates largely reflects the diverse conditions of observed flow. The most rapid rates are those of corehole closure, where rock salt under comparatively high lithostatic pressure expands toward a free surface to fill a corehole. After a period of accelerating flow lasting a few weeks, the rate of flow declines in approximately exponential manner. The higher rate of measured closure in the corehole than in mined cavities is probably due to the fact that the observation period for cavity closure was 40-120 times as long and included the long period of decelerating flow (table 1, notes d and e). Salt glaciers are driven downhill by geologically minute shear stresses resulting from gravity (table 1, notes b and c). The glacial salt overcomes internal friction and bedrock drag and undergoes geologically rapid seasonal flow. Although Wenkert's (1979) estimates of flow rates are fairly similar to the direct measurements by Talbot and Rogers (1980), they may be slightly too high because he assumed a steady-state equilibrium between extrusion and wasting (solution); most glaciers are actually in overall retreat despite seasonal advances (Kent, 1979).

Estimates of the rate of salt uplift during diapirism cannot be made with the same precision as the direct measurements referred to above. Not only must certain assumptions be made, but all these methods also rely on paleontologic-radiometric dating of variable accuracy. Ewing and Ewing (1962) adopted the approach of directly measuring the thickness of sedimentary strata draped over an abyssal salt diapir. They assumed that the strata had been folded after their deposition. However, this is somewhat debatable because the strata are composed almost entirely of pelagic ooze, which could have settled on the seafloor mound with no evidence of angular unconformity on reflection seismic profiles. It is therefore possible that the calculated strain rate for the Sigsbee mound is too high.

Different methods must be applied to older salt diapirs in the interior salt basins such as the East Texas Basin. Estimates based on the upward flexure of overburden are likely to be too low because they ignore the effects of dissolution or extrusion of salt, and record only the late, declining phase of growth. Carter and Heard (1970) made a "crude estimate" of strain rate of $10^{-15}/s$ in calculating areal strain from the difference in plan-view area between the peripheral sink and the salt stock. These authors assumed a conservatively long period of diapiric growth (120 Ma), whereas detailed stratigraphic thickness measurements of East Texas Domes suggests that more than 90 percent of the growth of each diapir took place over only 30 Ma (Seni and Jackson, 1983).

The distinction between rates of gross growth and net growth is important. Gross rates are a function of the volume of salt evacuated from a withdrawal basin and mobilized up the diapir. Net rates are a function not only of this process, but also of all other processes that affect diapir height, such as salt dissolution, extrusion, and lateral intrusion. Strain rates calculated for the diapirs of East Texas are shown in table 1, note g (from Seni and Jackson, 1983). These calculations are based on borehole information, which is commonly lacking for the deeper intervals that record early stages of diapir growth. Hainesville Dome is an exception. Because of the anomalously late initiation of diapirism, subsurface data reflecting almost all of its growth history is available. Its peak growth rate is approximately seven times that of its average rate. In the case of the Zechstein Salt Basin in northern Germany, Sanneman (1968, and in Trusheim, 1960) has estimated average flow rates of 0.3 mm/yr in both a horizontal (wave migration) and vertical (diapiric rise) direction by stratigraphic-thickness measurements. His strain rate of $10^{-15}/s$ was based on an average for all diapirs.

In summary, we can be reasonably confident that under natural geologic conditions rock salt flows with strain rates as rapid as 10^{-11} to $10^{-9}/s$ in glaciers and 10^{-14} to $10^{-15}/s$ in actively growing diapirs.

Physical Conditions of Salt Diapirism

The physical conditions of diapirism, illustrated for Oakwood Dome in East Texas vary with depth and time, but can be estimated within limits (table 2). Depth limits are provided by the base and crest of the salt stock. Maximum and minimum temperatures at these depths can be estimated from measured heat flow, allowing for the high thermal conductivity of rock salt (Selig and Wallick, 1966), which allows the salt stocks to act as "heat chimneys." Because the East Texas Basin shows many of the attributes of a passive margin produced by rifting and breakup of continental crust (Turk, Kehle and Associates, 1978; Jackson and Seni, 1983), it may be convincingly argued that heat flow during Late Cretaceous diapirism would have been higher than at present (Sprague and Pollack, 1980). However, the Louann Salt lay beneath a thinner overburden during the Cretaceous, which would nullify the effects of higher heat flow. The differential lithostatic pressure between the top and the base of the salt stock results from a negative density contrast at the base (dense sediments overlying less dense rock salt). At the crest of the diapir the uncompacted state of the surrounding sediments ensures that they are less dense than the virtually incompressible rock salt; the diapir therefore has negative buoyancy. At the crest the rock salt is not supported by the surrounding strata but by the strength of the salt column below.

PART II: STRUCTURE OF THE TOG-1 SALT CORE, OAKWOOD DOME

Core from the LETCO TOG-1 borehole represents the primary data source for this study. The vertical borehole was drilled just north of the axis of Oakwood Dome in Freestone County. It intersects rock salt at 354.5 m and ends at a depth of 411.8 m, yielding 57.3 m of rock-salt core. The lithology of the continuous 10 cm-wide core through salt and the base of the cap rock was studied by Dix and Jackson (1982) in transmitted and reflected light using both thick sections (1-10 mm thick) and thin sections (< 1 mm thick). The microstructure, fluid inclusions, and geochemistry of rock salt in this core were also studied, and a detailed lithologic log of the core was provided (Dix and Jackson, 1982).

Table 2. Probable physical conditions for Oakwood diapirism^a

	Depth (m)	Lithostatic Pressure (MPa) ^d	Temperature ^e (°C)	Pressure difference ^f (MPa)
Crest	355 ^b	8	34	negative buoyancy
	600	14	44	0
Base	5,500 ^c	124	201	8.3

a Adapted from Carter and Heard (1970).

b From corehole log.

c From depth-corrected seismic section.

d Based on linear lithostatic pressure gradient of 22.5 MPa/km (Dickinson, 1953).

e Based on geothermal gradient of 40°C/km at 500 m and 33°C/km at 5,000 m, derived from regional geothermal gradient (American Association of Petroleum Geologists and United States Geological Survey, 1976), on core hole temperatures at 750 m and 1,500 m in Vacherie Dome, Louisiana, 4 yr after drilling (R. L. Thoms, personal communication, 1982), consideration of salt-dome conductivity (Selig and Wallick, 1966), and on mean surface temperature of 19.5°C.

f Between top of stock and depth listed (due to buoyancy).

The principal conclusions of their study were as follows. All but the uppermost 2 m of rock salt displays a strong deformation fabric induced by flow of salt during diapirism. Recrystallization of previously foliated rock salt produced a granoblastic polygonal texture in the upper 2 m of salt core. Microstructure, fluid inclusions, and bromine concentrations in halite suggest that recrystallization was promoted by downward movement of intercrystalline brine from the lower contact of the anhydrite cap rock. The absence of a cavity at this contact indicates that the salt stock is not presently being dissolved in the zone intersected by the borehole, and that previous dissolution has been compensated by diapiric rise of rock salt. An anhydrite lamina across halite-filled extension fractures at the base of the cap rock indicates that anhydrite layers have accreted against the base of the cap rock. The 57.3 m of rock-salt core contains an average of 1.3 ± 0.7 percent anhydrite. If all the cap rock was derived by residual accumulation of such low concentrations of anhydrite, dissolution of more than 6 km of rock salt would be required. Vertical shortening in the cap rock just above the contact was probably induced by upward force from the salt stock. This stress formed a horizontal, spaced, stylolitic cleavage by pressure solution and mass transfer of anhydrite. The stylolitic cleavage, which is marked by a dark insoluble residue, transects older lamination that is thought to reflect cycles of accretion of anhydrite against the base of the cap rock. Further lateral extension and vertical shortening in the base of the cap rock formed halite-filled vertical extension fractures and inclined shear fractures that postdate both the cap-rock lamination and the stylolitic cleavage.

The present report describes the result of a companion study on the natural strains in this salt core to evaluate the geologic stability of the salt. Geometric analysis was used to delineate the large-scale structure of the salt intersected by the vertical drill core. Strain analysis was used to estimate the orientation, type, and magnitude of finite strains at various depths.

Geometric Analysis

Structural Elements

Minor structures present in the Oakwood core allow the form and orientation of major structures to be deduced. The basic minor structural elements are as follows.

- (1) Layering is defined by disseminated anhydrite inclusions in poikiloblastic halite grains. It represents the deformed remains of bedding in the original evaporite.
- (2) Tectonic Fabric is defined by the shape and orientation of halite grains. A strong planar (S) component has the form of a schistosity defined by the planar preferred orientation of disc-like halite grains. A penetrative cleavage is parallel to the schistosity. A weaker linear (L) component is a mineral lineation defined by the preferred orientation of the major axes of halite grains within the plane of schistosity. Both the schistosity and the lineation can generally be recognized and delineated by eye. But in one part of the core where the fabric is weak, only strain analysis can detect the existence and orientation of these elements.

Defining Orientation in Nonoriented Core

Using the relative orientations of layering and schistosity to determine major structures in a single borehole is not straightforward. Because the TOG-1 borehole is vertical to within 2° throughout its length, all dip angles measured relative to the core axis represent true dip. But the core itself is nonoriented, so the directions of dip (or strikes, or trends) are uncertain. Nevertheless the dip of the schistosity is extremely consistent: 64 dip readings with a mean of 34° have a standard deviation of only 4°. Conceivably the direction of dip could vary although the dip remained constant. But the resulting pattern of strain is improbable. The most likely and reasonable estimate of the major structure is therefore obtained by assuming a constant direction of dip for the schistosity. In vertical cross sections this dip direction is fixed toward the left, and in plan views the dip azimuth of the schistosity is to the south. The leftward direction was arbitrarily chosen. The southward direction is the most likely dip azimuth--

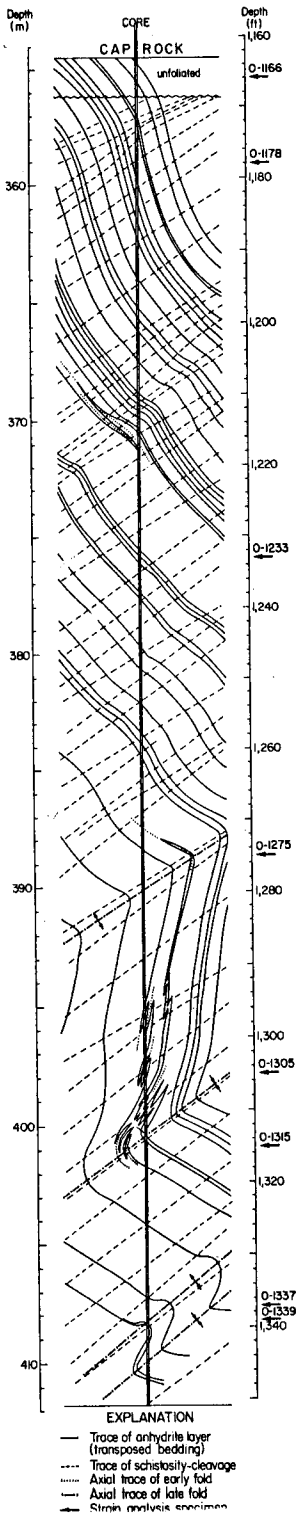
though far from certain--because this is the direction in which lies the dome axis. Because of its consistent dip, the schistosity provides a useful reference surface with which the much more variable layering can be compared. In vertical cross sections the schistosity is arbitrarily assigned positive dip angles. Accordingly layering with a dip azimuth within 90° from that of the schistosity is assigned positive angles of dip (fig. 17). Conversely, layering with a dip azimuth of more than 90° from that of the schistosity is assigned negative angles of dip.

Structural Cross Section

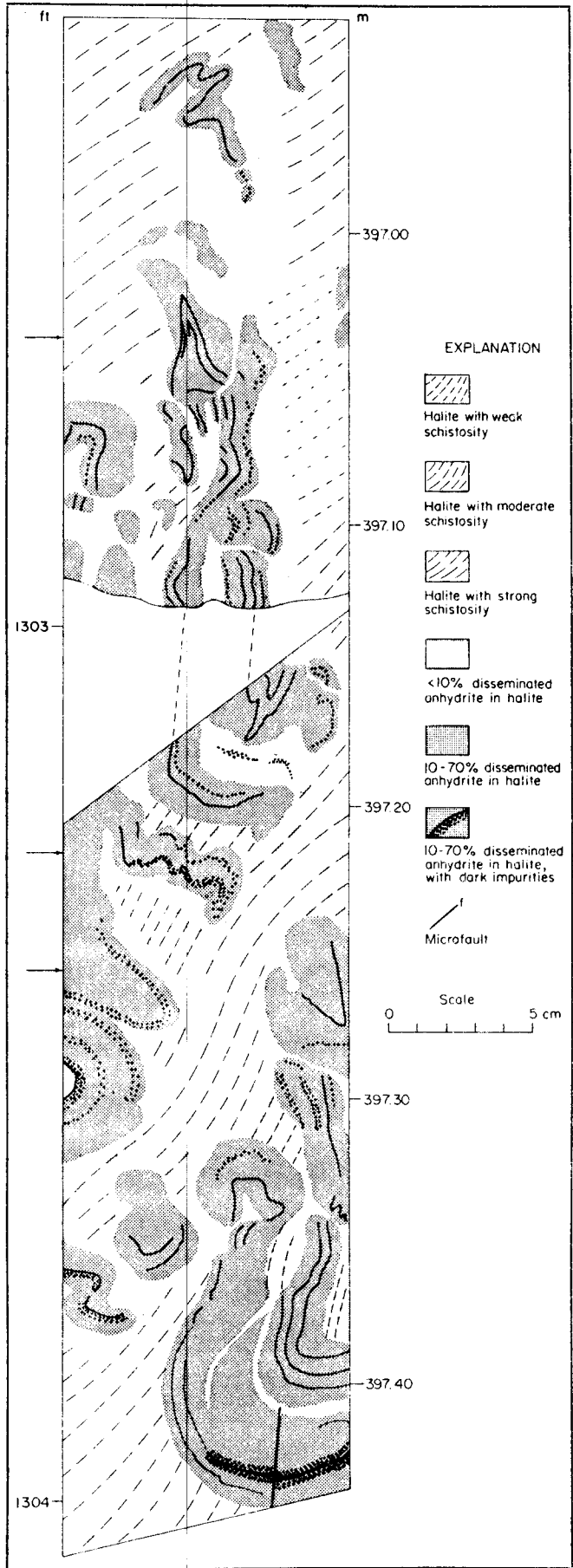
Figure 18A was constructed to scale according to the above conventions. It represents a vertical cross section based on the structural elements intersected by the core. The core itself is shown as a double line down the axis of the section. The traces of layering have been projected laterally beyond the limits of the core into the adjacent areas in order to display the large-scale structure clearly without resorting to scalar distortion, such as exaggerating the horizontal scale. The projection assumes similar-type folding for reasons discussed in the section entitled "Fold style in salt stocks". The traces of layering were projected with fixed orientation along the schistosity trace. In similar folds the schistosity trace represents a direction of high geometric stability, along which changes in layering orientation are small.

In the upper two-thirds of the salt core the schistosity and the layering dip in opposite directions, separated by a dihedral angle of approximately 90° . This geometric relation indicates the hinge zone of a first-order inclined antiform. The axial surface of this fold dips leftward. The lower third of the core represents the lower limb of the first-order antiform, in which four second-order major folds have formed. Their axial traces are shown in figure 18. These first-order and second-order flexures can be termed young folds, for they fold an older generation of isoclinal folds. The axial traces of these older isoclines are subparallel to the layering. Examples can be seen at depths of 370 m and 394-401 m in figure 18A and in detail in figure 18B. The minor isoclines are transected by the schistosity. These older folds may be prediapiric, having formed by diagenetic volume changes in the evaporite unit. Or they may be syndiapiric, having formed during centripetal salt flow toward the base of Oakwood Dome by

Figure 18. (A) Structural cross section along vertical salt core, Oakwood Dome. On the basis of measurements of layering and schistosity, the section was constructed to scale assuming a mechanism of similar folding and projecting elements outward from the core for better visibility. (B) Schistosity (dashed lines) in the halite transects older isoclinal folds at arrowed localities. Thin, anhydrite-rich layers containing dark laminae (each shown as a solid line) have been boudinaged in numerous places. Traced from contiguous thick sections. [From Dix and Jackson, 1982.]



A.



B.

either of the two mechanisms (convergent flow superposed on weak buckling, or refolding and rotation of recumbent folds) discussed in the section entitled "Formation of folds and interference structures in salt stocks."

The mutual orientations of schistosity and layering allow determination of the orientation of the fold axes relative to the schistosity. As explained above, schistosity is assumed to dip southward. In the core the trace of the disseminated-anhydrite layering is visible on the schistosity surface as a fuzzy band 1-5 cm wide. The broad width and vague delineation of this layering trace make it difficult to measure with precision. But where recognized, this trace is approximately parallel to the strike of the schistosity (fig. 19). Using Laing's (1977) method for bedding-cleavage intersections on cleavage surfaces, the axes of the major folds intersected by the drill were determined to trend east-west with negligible plunge (fig. 19). These inclined horizontal folds therefore appear to be concentric about the axis of Oakwood Dome, assuming the schistosity dip towards this axis.

The large-scale structure of a first-order inclined antiform (or anticlinorium) with second-order folds on its lower limb is illustrated in figure 20. The inferred form of the major structure above and below the core is shown in dashed lines. Three hypothetical fold forms marked a, b, and c, show the possible upward continuation of the structure in the past. However, this zone is presently occupied by cap rock, indicating that the inferred salt structures have been removed during truncation of the dome crest. The most obvious agent for truncation of the salt stock is groundwater dissolution. The minimum thickness of salt removed can be estimated, as shown in figure 20. These estimates vary from 30 m upward, according to the model selected for the former shape of the upper part of the structure, shown as a, b, or c.

Because of this inferred truncation, the horizontal base of the cap rock is discordant across the inclined layering and schistosity (fig. 18). On a broad scale, therefore, this contact resembles an angular unconformity. Nevertheless detailed study of the microstructure of the uppermost zone of rock salt, which is unfoliated and very coarse grained, shows that this salt

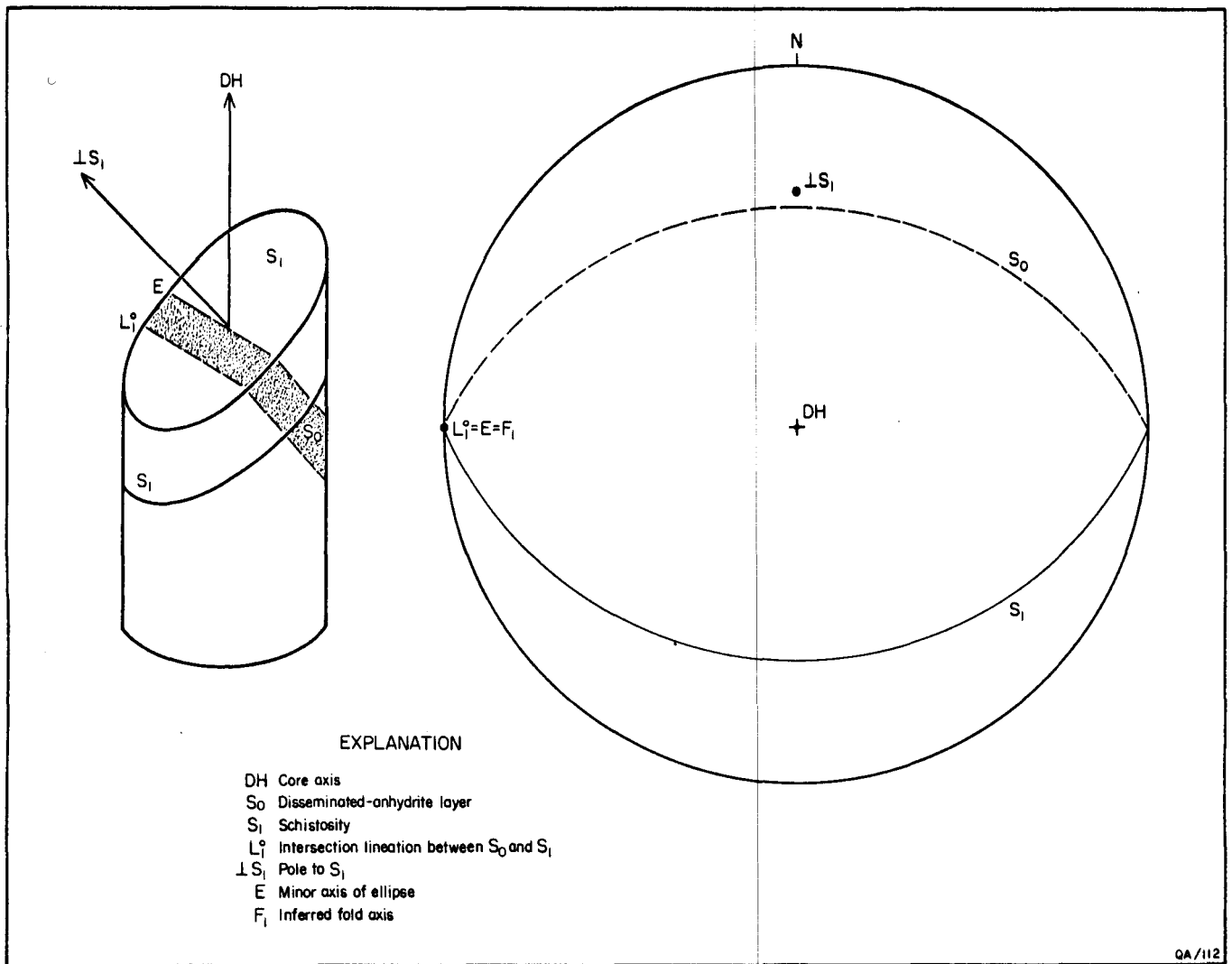


Figure 19. Deducing the orientation of a fold axis from the trace of layering in a schistosity plane. Fold axis trends subhorizontally, parallel to strikes of S_0 and S_1 . Left, diagrammatic view of vertical core. Right, equal-area stereographic projection.

recrystallized and was partly dissolved during accretion of the lowermost layer of the anhydrite cap rock (Dix and Jackson, 1982). The structure is therefore partly equivalent to a metamorphosed angular unconformity. A high degree of discordance between the cap-rock contact and layering in rock salt has also been reported from Tatum Dome in Mississippi (Eagle, 1962), and from Rayburn's and Vacherie Domes in Louisiana (Nance and Wilcox, 1979; Nance and others, 1979). Structural evidence for the truncation of diapiric crests may thus be more common than previously supposed.

Implications to Internal Structure

Figure 21 is a model for salt emplacement as discrete tongues of rock salt flowing at different velocities and times, based on the structural geometry of the TOG-1 core. Differential vertical movement of salt tongues has been previously inferred for other salt domes (Balk, 1949; Lotze, 1957; Muehlberger, 1959; Kupfer, 1974, 1976) but was not formerly postulated for lateral flow as well. The salt tongues emerge from the stem of the diapir as vertically plunging folds and become progressively refolded by lateral flow to form recumbent overthrust folds. The geometry of the Oakwood salt core suggests that it passed through the hinge zone of one of the younger, higher overthrust anticlinoria within the dome.

These observations show how it is possible to delineate the form of major structures in salt stocks on the basis of a single core, despite the absence of either stratigraphic criteria or core orientation.

Strain Analysis

Strain analysis--the determination of the magnitude, orientation, and type of strains in a given sample--has progressed so that virtually any rock, including ice, may be investigated. Petrofabric studies, which represent a microscopic approach to geometric analysis, have been carried out on halite (for example, Balk, 1949; Schwerdtner, 1967; Muehlberger and Clabaugh, 1968), but these studies did not attempt to quantify strains.

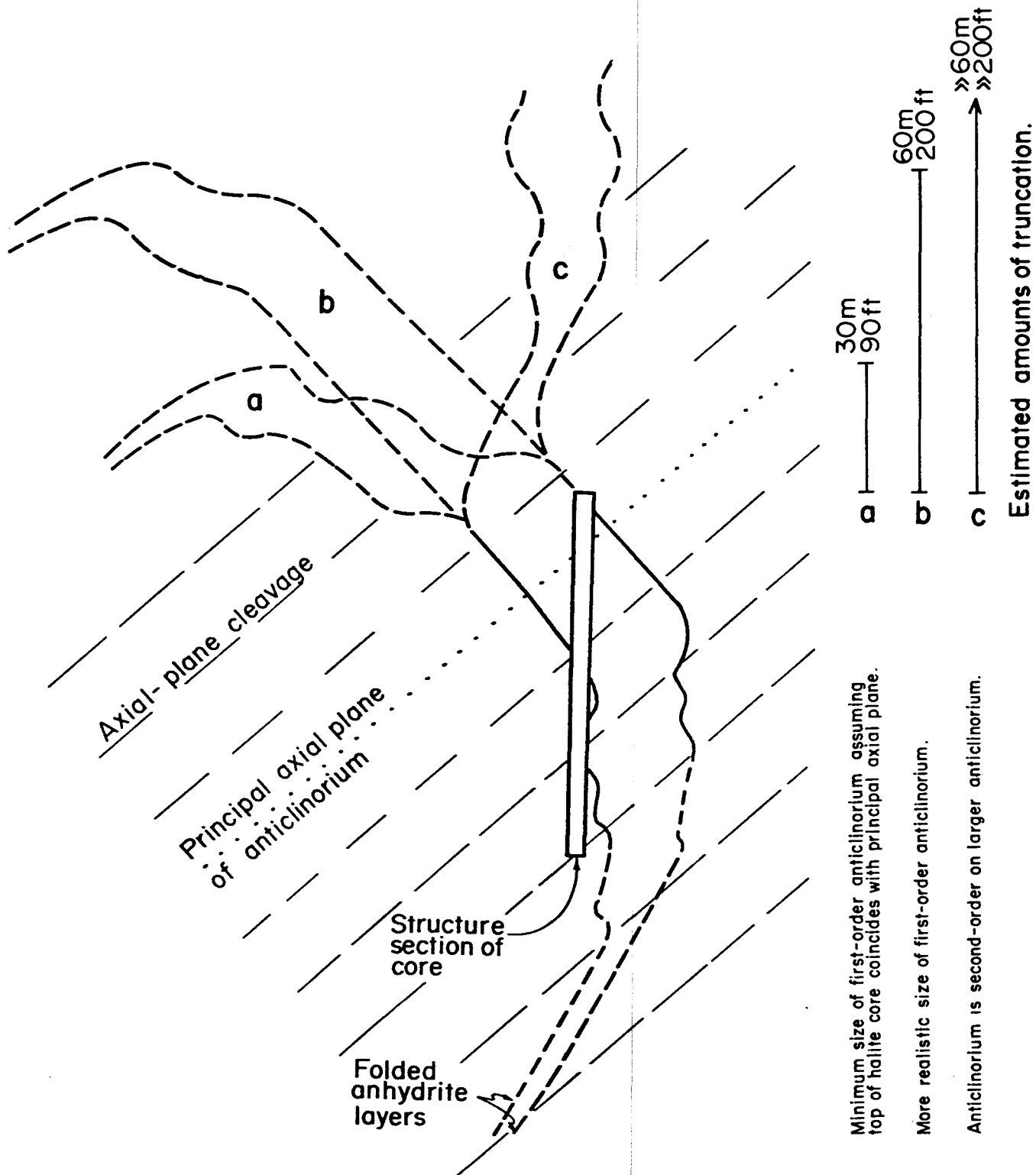


Figure 20. Medium-scale structure within Oakwood Dome, extrapolated on the basis of figure 18A. Three hypothetical structures, a, b, c, were possible. Removal of each allows for different estimates of the amount of structural truncation.

The raw material for strain analysis is discrete objects in deformed rock, such as initially subspherical ooids, spherulites, pisolites, oncolites, reduction spots, and vesicles and non-spherical mineral grains, clasts, lapilli, body and trace fossils, stromatolites, folds, or igneous and sedimentary veins. Only objects whose initial shape, size, or orientation can be reasonably inferred can be used as strain markers.

Not all aspects of deformation can be computed by strain analysis of natural rocks. The translation, or direction and amount of movement of the whole rock mass from its place of origin, can rarely be determined. Similarly strain analysis is rarely capable of determining the rotational component of strain, that is, the rotation of a line which has become the direction of maximum elongation. Nevertheless, strain analysis excels at determining the distortional component of strain, which describes the change of shape during deformation. Most strain markers yield only the proportional ratio of the principal strains rather than the actual elongations.

Because the shapes of halite grains in the deformed rock salt of Oakwood Dome can be approximated closely by ellipsoids, we need consider only those methods of strain analysis applicable to ellipsoidal objects. Most objects in sedimentary rocks can be mathematically treated as ellipsoids. Two-dimensional sections through them yield elliptical shapes. Critical examination of unstrained, natural fabrics in undeformed rocks has shown that truly spherical particles are extremely rare, even in rocks such as oolitic limestone (Boulter, 1976; Ramsay, 1976; Sarkar and others, 1982). Accordingly, the deformation fabric shown in figure 22, A is rare in natural examples; it would be unrealistic to assume that all particles were initially circular, as in some early methods of strain analysis. The initial distribution in figure 22, B is also unrealistic. Even if a rock was composed of ellipsoidal particles of uniform shape and size, elliptical sections through them would vary in size because not all of them would pass through the centers of grains. Most sedimentary rocks contain elliptical markers that initially had

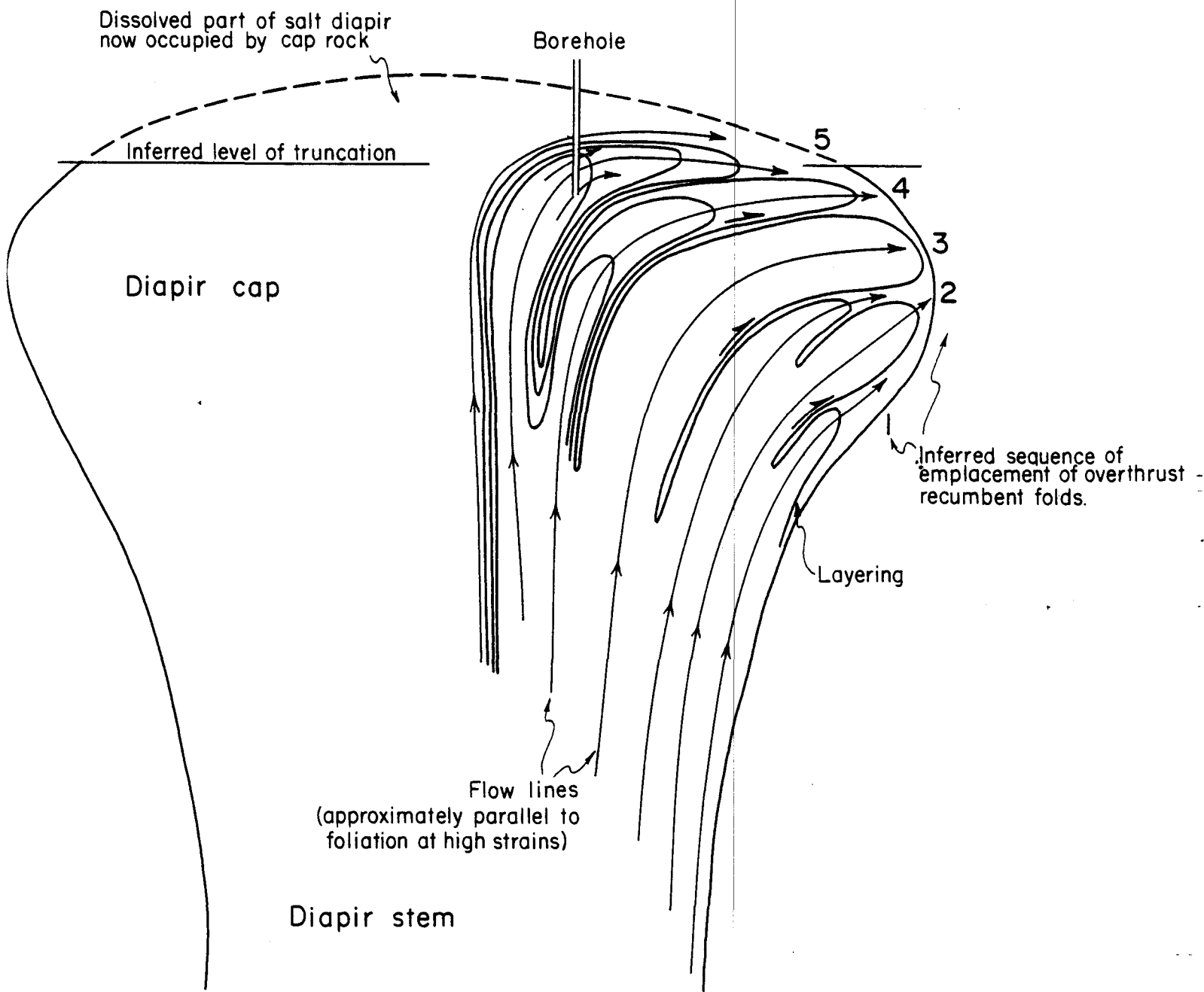
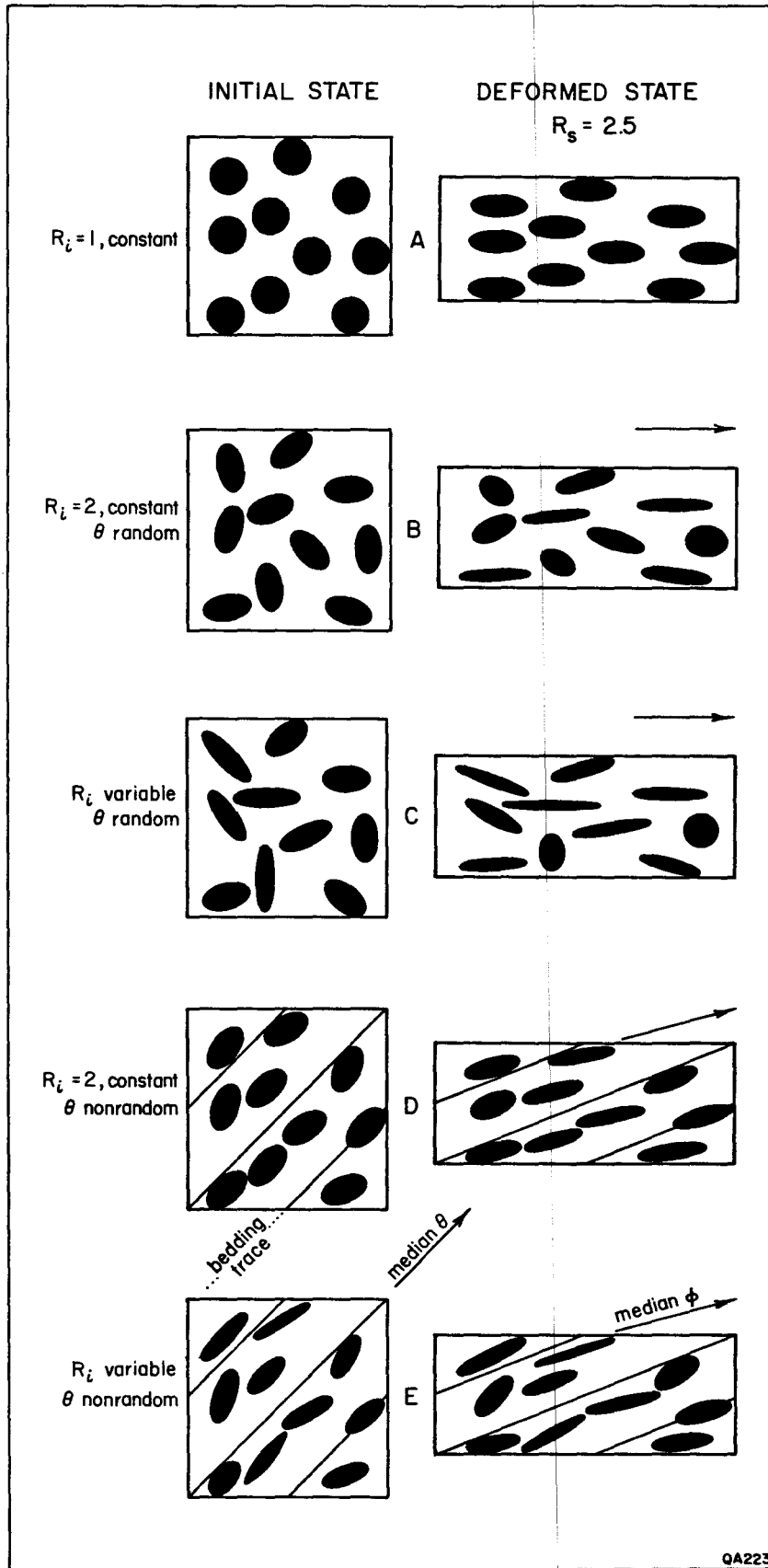


Figure 21. Model, based on figures 18 and 20, for flow patterns within Oakwood Dome. Tongues of salt are sequentially overthrust as vertical folds refolded to recumbent folds. The TOG-1 borehole has pierced the lower part of tongue 5. The upper part of this tongue has been removed by truncation of the dome crest.

Figure 22. Model deformation fabrics produced by homogeneous, plane-strain, pure shear ($R_S = 2.5$) of ideal populations of circular and elliptical particles (black dots). Initial axial ratios and orientations are designated R_i and θ , respectively and shown at left. In cases of random initial distributions (B, C) median ϕ orientations after strain (shown by arrows) are parallel to principal extension directions (long side of right rectangles). In cases of nonrandom initial distribution where the particles show bedding-preferred orientation (D, E) neither the median ϕ , nor the principal extension direction, nor the bedding trace are parallel after strain. (A-D modified from Ramsay, 1976).



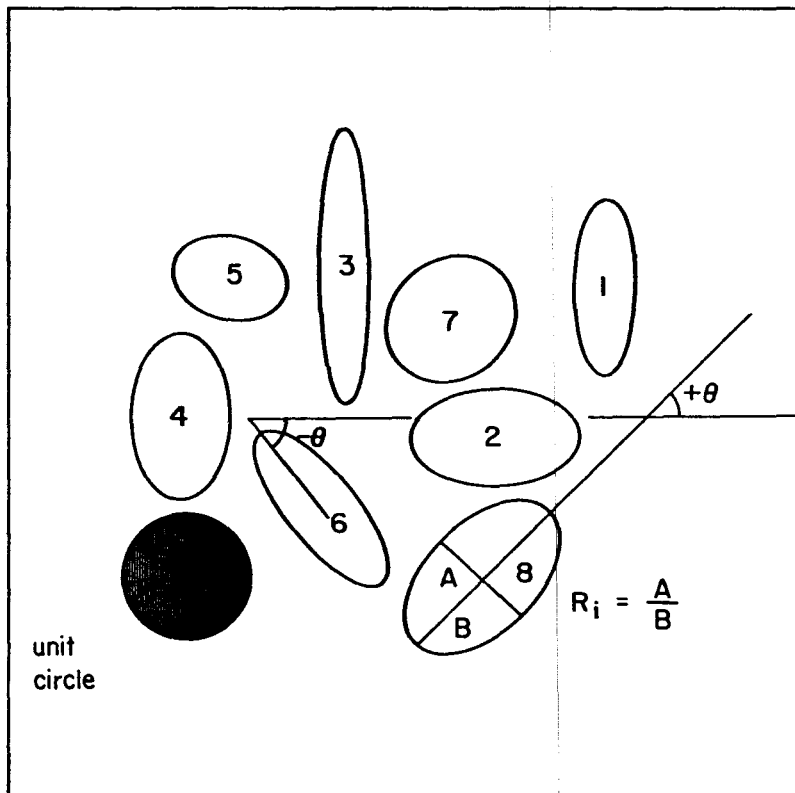


Figure 23. Unstrained elliptical particles, with arbitrary numbers for reference, and a unit circle, showing initial axial ratios (R_i) and θ angles measured from a reference line. Note the sign convention for θ .

variable axial ratios, and are commonly in random orientation. Figure 22, C, therefore, represents a common sedimentary fabric.

In contrast to these isotropic initial fabrics, many tectonically undeformed rocks contain anisotropic fabrics caused by depositional currents, mass flow, or compaction. This anisotropy is manifested in linear or planar preferred orientation of clasts. Initial anisotropy is difficult to detect after the rock has been naturally deformed (fig. 22, D, E), and most methods of strain analysis are not equal to the task. Fortunately, although the initial fabric in figure 22, E is probably common in clastic rocks because of compaction, the anisotropy does not always pose problems because either the rock is such that compaction is negligible (as in chemical precipitates and most igneous rocks), or the compactional strain is dwarfed by the tectonic strain.

Ideally methods of strain analysis should be able to: (1) determine whether strain was homogeneous (i.e., sets of planes that were parallel before deformation remained parallel after deformation) within the scale of the sample; (2) be applied to particles that were of variable shape and orientation before deformation; and (3) recognize whether, or at least accommodate, fabrics that were anisotropic before deformation, such as those containing imbricate clasts. Methods of strain analysis use data concerning grain shape and, commonly, grain orientation taken from samples of deformed rocks. The data are then mathematically or graphically "unstrained" to the point where the fabrics are closest to the assumed original, undeformed, state—typically ellipses of variable axial ratio and random orientation. The reciprocal of this "unstrain" is inferred to be the amount of finite strain undergone by the rock since its initial undeformed state.

Most methods of strain analysis study two-dimensional strains recorded in planes through rock samples. Three-dimensional strains can be estimated by integrating strains calculated in two or more of these planes.

The theoretical behavior of elliptical particles during homogeneous strain is well understood (e.g., Ramsay, 1967, p. 202-221; Dunnet, 1969; Dunnet and Siddans, 1971; Elliott, 1970; Matthews and others, 1974; Shimamoto and Ikeda, 1976). In any group of elliptical particles, the shape and orientation of each ellipse can be specified by its axial ratio, R_i , and the angle, θ , between its major axis and an arbitrary direction (fig. 23); note the sign convention for θ angles, proposed by Elliott (1970). After a homogeneous strain of $R_s = 3$, represented by the strain ellipse in figure 24, each ellipse takes up a new shape, R_f , and orientation, ϕ , depending on its initial shape and orientation and the imposed strain.

Particles whose major or minor axes are parallel to the principal extension direction, or X direction, can be divided into four types (Elliott, 1970), whose names follow those applied to distorted fossils by Breddin (1956). Particles, such as ellipse 1, can be distorted to a circular form if their initial shape and orientation is an exact reciprocal of the imposed strain (fig. 24). Particles that are "unstrained" to less-elliptical shapes are known as pre-circle broad (Elliott, 1970), such as ellipse 3. Particles that are "unstrained" to the point where they pass through the circular form and switch their major axis orientation, like ellipse 4, are known as post-circle broad. Particles that simply become progressively more elliptical because they were originally elongated in the principal extension direction, like ellipse 2, are known as narrow. Apart from these four special forms, most particles become more elliptical and rotate toward the X direction with increasing homogeneous strain. As a result, the fluctuation, or range of ϕ angles, invariably decreases with increasing strain, a characteristic exploited by some methods of strain analysis.

Two-dimensional strains

Eight sample sites were selected along the salt core; seven are in the foliated R-1 section and one is in the unfoliated R-2 section (fig. 18); sample numbers are equivalent to depths in feet. Sample sites were selected to (1) avoid rock salt with very coarse grain size and, consequently, few grains per specimen, (2) avoid concentrations of disseminated anhydrite

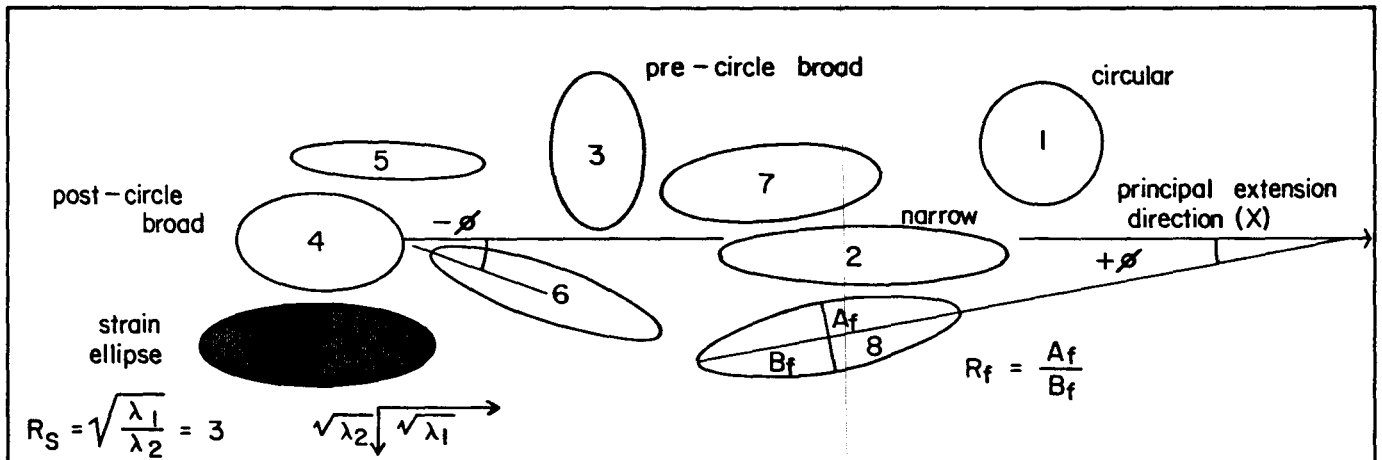


Figure 24. The particles of figure 23, after homogeneous pure shear ($R_s = 3$ illustrated by the strain ellipse), showing finite axial ratios (R_f), and ϕ angles measured from a reference line (here, parallel to the principal extension direction, X). Note the sign convention for ϕ . Most particles have become thinner and have rotated toward the X direction. But particle 3 has become fatter, particle 1 has become circular, and particle 4 is little changed in shape although its orientation has changed by 90 degrees.

grains, which obscure halite grain boundaries and induce inhomogeneous deformation, (3) occupy interesting structural positions. From each sample site three mutually perpendicular planes were cut parallel to the principal planes of strain. The orientation of the foliation (XY) plane was estimated visually, and the first cut was made parallel to it. The orientation of the principal extension (X direction) was determined by strain analysis. Planes parallel to the XZ and YZ planes could then be accurately cut and analyzed. From these analyses it could then be determined how close the initial cut was to the XY plane, and the results adjusted algebraically or on a Mohr diagram (see next section).

Preparation of rock-salt specimens requires special techniques because of high solubility and very coarse grain size, which varies from an average of 23 x 7 mm in foliated pure rock salt to an average of 11 x 3 mm foliated rock salt containing more than 5 percent disseminated anhydrite; in the unfoliated R-2 zone the mean grain size is 5 to 10 mm (Dix and Jackson, 1982). The effects of high solubility were countered by lubricating the cutting saw with mineral oil. The coarse grain size was accommodated by large specimens, either thick sections, about 250 x 100 x 9 mm in size, or etched slabs of similar lateral dimensions. Thick sections were constructed by polishing a slabbed surface on a grinding wheel in mineral oil, removing the oil by heating overnight at 80°C or with acetone, mounting on Plexiglas with polyester resin, planing down with slow, dry sawing, polishing, and cleaning with acetone, and covering with a thin layer of polyester using a sheet of mylar to ensure smoothness of the upper surface of the polyester. Etched slabs were prepared by lightly rubbing the sawn surface with fingers and water to smooth out saw marks, air drying to frost the surface by hydrous etching, and coating with a thin layer of 1:1 glycerin-water mixture; such surfaces are transparent but can be marked with fine pencil lines.

On each of the three principal planes at each of the eight sample sites the maximum and minimum lengths and orientation, with respect to the side of the slab or section, of 100 halite grains were measured, using the conventions shown in figure 24. A total of 2,400 grains were

measured. Large grains were preferentially selected in order to omit less deformed subgrains, which record little of the deformation history. Grain boundaries were distinguished from fractures and other surfaces by having a combination of the following features: (a) different cleavage directions on opposite sides of the boundary, (b) concentrations of small anhydrite crystals along them; (c) irregular geometry and air bubbles at intersections; and (d) an etched-induced depression along them, commonly rimmed with salt rime.

A wide range of strain-analysis methods is available for the study of elliptical particles. The principal groups of methods, their sources, and their relative advantages and disadvantages, are summarized in table 3. Because no one method is wholly advantageous, three different methods were employed to allow comparisons and to provide maximum objectivity and versatility: the Harmonic Mean Method, the Theta Curve Method, and the Shape Factor Grid. The results of these three methods for an XY (little deformed) section and an XZ (highly deformed) section are compared in figure 25. Only the third method is valid for initially anisotropic fabrics (e.g., fig. 22, D, E), and was included mainly for this reason. However, as described below, it transpired that no evidence for initial anisotropy was found. This is understandable in a chemical precipitate.

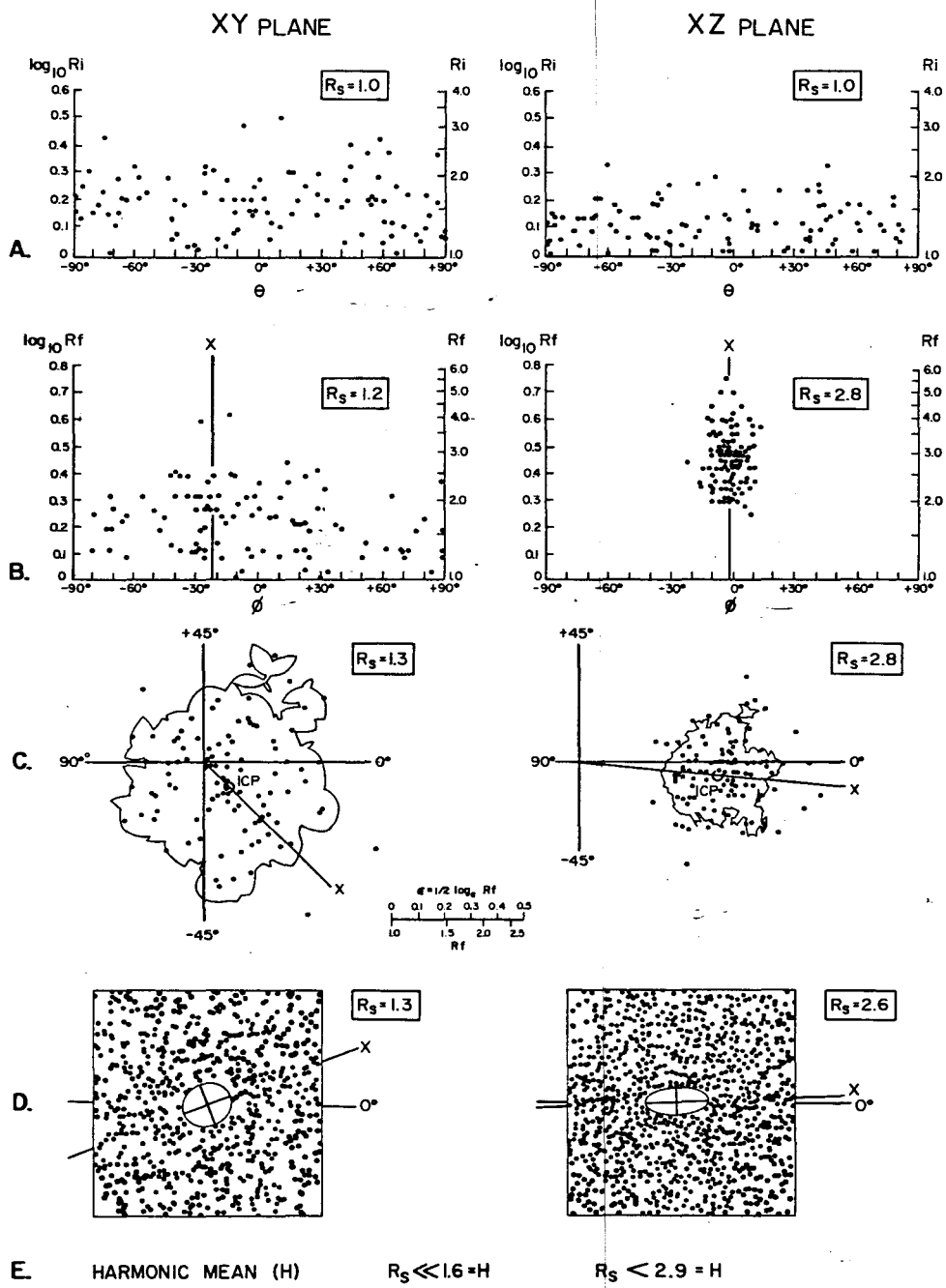
The harmonic mean (table 3) of the axial ratios of a set of elliptical particles provides an approximate measure of the strain ratio, R_s . The accuracy of this measure increases with increasing strain ratios and decreasing initial axial ratios, R_i , and fluctuation; it is invariably more accurate than either the arithmetic mean or the geometric mean (Lisle, 1977b). Unlike the other methods, it does not require measurement of grain orientations, ϕ , so both data collection and processing are much faster.

The Theta Curve Method (Lisle, 1977a) provides an accurate and completely objective means of determining strain. Its efficiency was greatly improved by the development of the computer program THETA by Peach and Lisle (1979). As well as calculating the harmonic mean, the program sequentially unstrains the R_f/ϕ data in small increments by superimposing a

Figure 25. Comparison between methods of strain analysis of perpendicular sections through the same specimen (O-1339) of rock salt in core from Oakwood Dome, showing minimum strain ($R_s = 1.2$ in XY plane) and maximum strain ($R_s = 2.8$ in XZ plane). (A) 100 mathematically unstrained grains on a R_f/ϕ plot showing estimated initial fabrics in salt before deformation. (B) 100 strained grains on a R_f/ϕ plot, showing the present strains in the salt. (C) 100 strained grains on the shape-factor grid. The ICP (initial circle point) lies on the X direction and defines the finite strain for the whole sample of grains. (D) Random-point distributions that define ellipses representing whole-rock strain. In these particular distributions the ellipses are comparatively well defined and the strain magnitudes agree with that of the other methods. But in general this method did not define strain ellipses sufficiently accurately to be used. (E) Harmonic means provide reasonably accurate strain ratios at high strains (XZ plane), but overestimate strain ratios at low strains (XY plane).

Table 3. Some methods of strain analysis applied to elliptical particles.

Methods	Principles	Advantages	Disadvantages	References
Harmonic mean (H)	$H = \frac{n}{\sum \frac{1}{R_f}}$	Fast, simple, objective. Accurate to within 10% with $R_s > 2.5$, $R_i < 2.2$, or $R_s > 1.5$, $R_i < 1.5$. Accuracy increases at high strains and low fluctuation. Measurements of ϕ not required.	Valid only for isotropic initial fabrics. Greatly overestimates R_s in cases of low R_s or high R_i .	Lisle (1977b) Lisle (1979)
Shape factor grid	Polar graph of 2ϕ against $1/2 \log_e R_f$. Qualitative identification of initial fabric from Mellis contoured pattern on graph. Strain estimate based on identification of initial circle point (ICP).	Suitable for isotropic, bedding-parallel, or imbricate initial fabrics. Does not require bedding or cleavage trace.	Serious errors result from misidentification of initial fabric. Less accurate at high R_s and low ϕ .	Elliott (1970) Boulter (1976)
Theta curve (θ)	Rectangular graph of ϕ against $\log R_f$ compared with sets of θ curves, which are loci of equal initial orientation, for different R_s values. Set resulting in most uniform distribution is taken as actual R_s . Computerized method provides unstraining facilities, χ^2 tests for goodness of fit.	Objective. Can test data for anisotropy in initial fabrics. Checks for ductility contrast or pressure solution. Does not require bedding or cleavage trace.	Valid only for isotropic initial fabrics. Less accurate at high R_s and low ϕ .	Lisle (1977a) Peach and Lisle (1979)
R_f/ϕ	Rectangular graph of ϕ against $\log_{10} R_f$ compared with sets of R_f/ϕ curves and "50% of data" curves. Computerized methods check symmetry.	Enables R_s estimates to be made from initially anisotropic fabrics in some cases. Valid for non-coaxial strain.	Later versions designed for some anisotropic initial fabrics, but not necessarily valid. Matching of R_f/ϕ curves is subjective. Data are not used to test method. Less accurate at high R_s and low ϕ . Most versions require bedding or cleavage trace.	Ramsay (1967) Dunnett (1969) Dunnett and Siddans (1971) Roberts and Siddans (1971) Le Theoff (1979) De Paor (1980) Siddans (1980)
Random-point distributions	Produces "all-object-separations" plot corresponding to strain ellipse. Computerized or entirely graphical methods available.	Records total strain in rock. Method unaffected by pressure solution. Does not require bedding or cleavage trace.	Not suitable for Poisson, or truly random, initial distributions. Valid only for isotropic initial distributions.	Fry (1979) Hanna and Fry (1979)



coaxial strain whose extension direction is normal to the preferred orientation of the grain distribution. The program calculates the vector mean and the median ϕ angle to check for skewness of data and to find the correct unstraining angle. At each unstraining increment the distribution is tested for randomness by the χ^2 test until the point of maximum randomness (lowest χ^2 value) is reached. The reciprocal of the unstraining amount is taken to be the amount of finite strain undergone by the analyzed specimen. The lowest χ^2 value also serves as an objective test for the appropriateness of the method. In cases of inhomogeneous strain or initial preferred orientation, specified χ^2 levels are exceeded, indicating that results should be treated with caution.

Unlike the two previously mentioned methods, Elliott's (1970) Shape Factor Grid is a largely graphical method. It uses exactly the same R_f/ϕ data as the Theta Curve Method. The data were plotted on a special polar grid, the coordinates of each point corresponding to a radius proportional to half the natural log of the R_f ratio and an angle of 2ϕ . After contouring the data by the Mellis Method, the location of the Initial Circle Point (ICP) was located, corresponding to an imaginary grain of circular section before deformation. The subjectivity inherent in this locating process was minimized by (1) assuming an initial random distribution unless the pattern of points diverged markedly from a circular or elliptical distribution field; (2) knowing that the ICP must lie along the schistosity trace on the grid; (3) locating the ICP slightly farther away from the graph's origin than the present center. Heart-shaped or delta-shaped contour patterns would indicate an initial preferred orientation in clastic rocks; here the ICP would again be on a plane of mirror symmetry but on the edge of the field.

The two-dimensional strains obtained by these three methods are summarized in table 4; figures 26 through 29 show the measured data in graphical form. In order to test the hypothesis that smaller grains in each data sample may represent less deformed subgrains, program THETA was modified slightly to order each sample of 100 grains by size and divide them into two groups of 50 grains separated by the median value; these groups are termed "large grains" and

Table 4. Two-dimensional strain ratios (R_f) from Oakwood salt core obtained by three different methods.

Sample Depth (ft)	Principal Plane	Harmonic Mean			All	Theta Curve		Shape Factor Grid
		All	Large	Small		Large	Small	
1166	XY	1.02	1.03	1.07	1.00	1.38	1.03	1.16
	YZ	1.71	1.63	1.74	1.40	1.12	1.33	1.31
	XZ	1.74	1.69	1.87	1.40	1.54	1.37	1.51
1178	XY	1.14	1.10	1.19	1.00	1.02	1.00	1.18
	YZ	2.08	2.09	2.07	2.00	2.08	1.89	1.96
	XZ	2.38	2.31	2.45	2.00	2.12	1.89	2.31
1233	XY	1.11	1.06	1.16	1.18	1.20	1.13	1.30
	YZ	2.25	2.26	2.23	1.97	1.94	2.36	2.06
	XZ	2.49	2.41	2.58	2.33	2.33	2.09	2.67
1275	XY	1.42	1.46	1.37	1.30	1.28	1.21	1.30
	YZ	2.24	2.16	2.33	2.24	2.14	2.18	2.28
	XZ	3.17	3.15	3.19	2.91	2.75	2.63	2.97
1305	XY	1.42	1.33	1.51	1.15	1.08	1.44	1.20
	YZ	2.13	2.28	1.99	2.12	2.39	1.74	2.29
	XZ	3.02	3.03	3.00	2.44	2.58	2.50	2.75
1315	XY	1.29	1.34	1.24	1.41	1.47	1.29	1.47
	YZ	2.32	2.21	2.46	2.00	1.97	2.20	2.20
	XZ	3.00	2.95	3.05	2.81	2.89	2.83	3.23
1337	XY	1.39	1.56	1.21	1.25	1.40	1.13	1.37
	YZ	2.23	2.04	2.48	2.23	2.15	2.40	2.25
	XZ	3.10	3.17	3.00	2.79	3.01	2.72	3.08
1339	XY	1.25	1.19	1.19	1.23	1.32	1.29	1.31
	YZ	2.53	2.62	2.54	2.43	2.41	2.23	2.62
	XZ	3.16	3.11	3.02	2.99	3.18	2.87	3.44

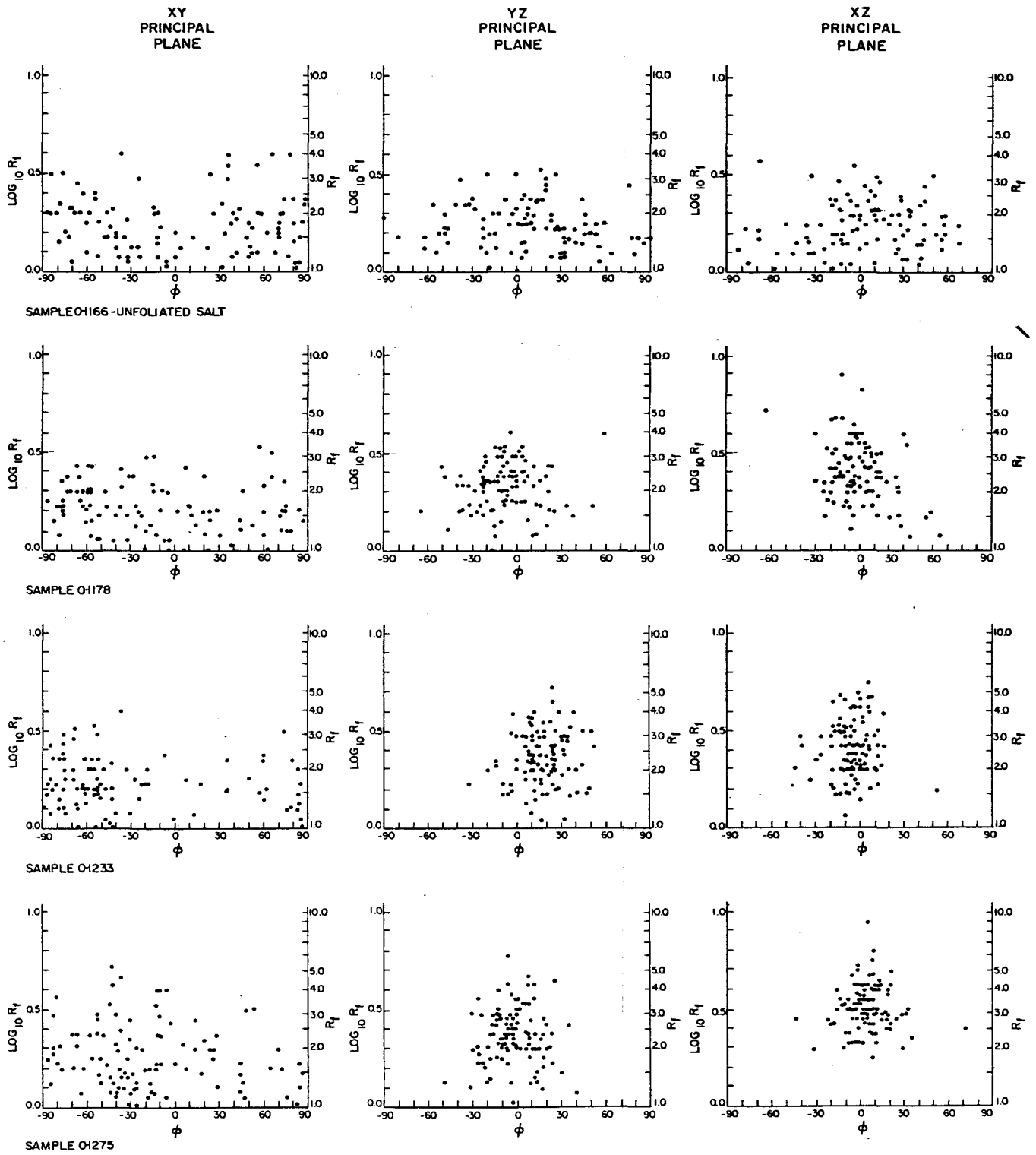


Figure 26. Strain states in rock-salt specimens O-1166, O-1178, O-1233, and O-1275 on R_f/ϕ plots. Note the increased degree of preferred orientation in the most strained (XZ) sections.

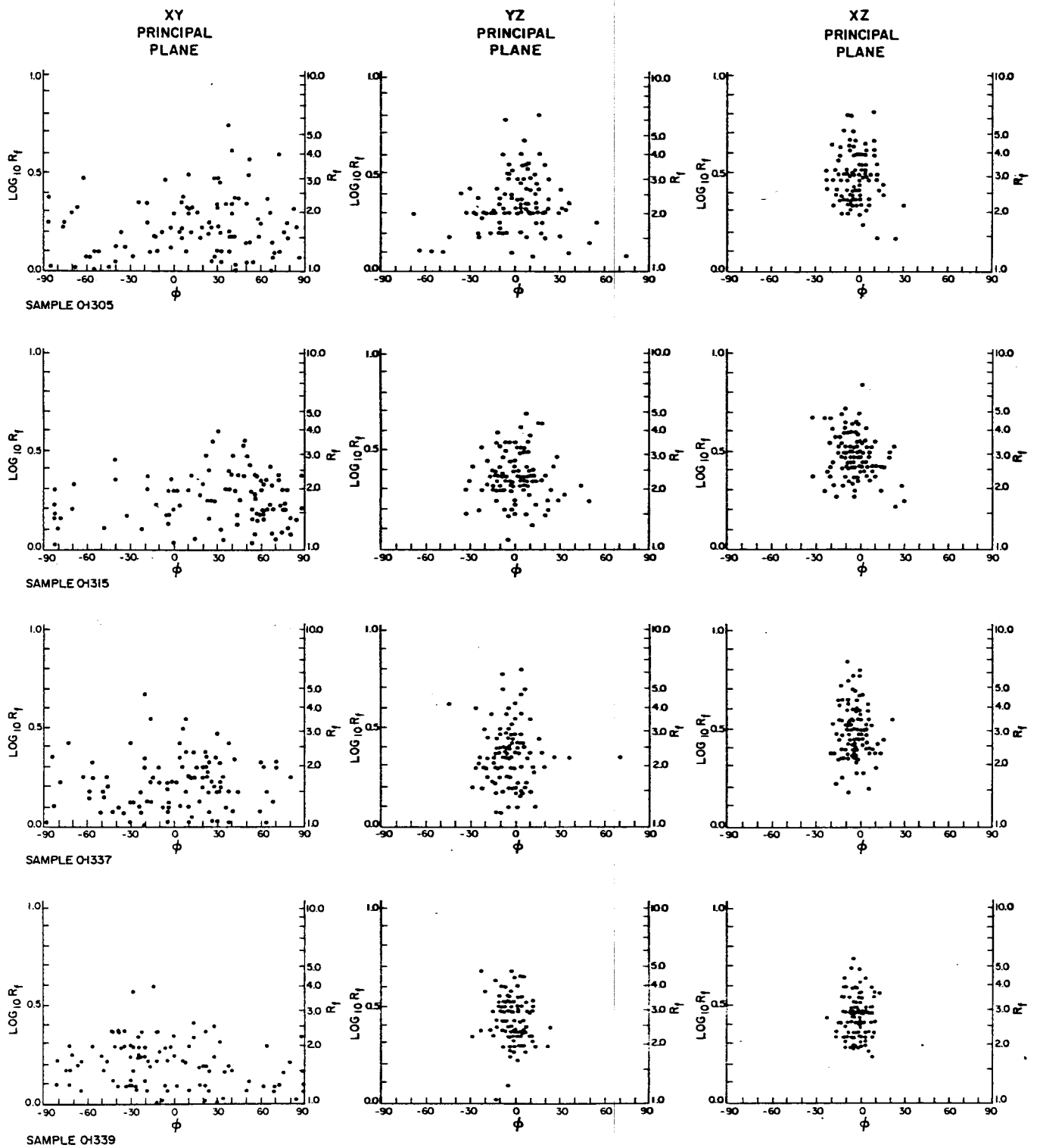


Figure 27. Strain states in rock-salt specimens O-1305, O-1315, O-1337, and O-1339 on R_f/ϕ plots. Note the increased degree of preferred orientation in the most strained (XZ) sections.

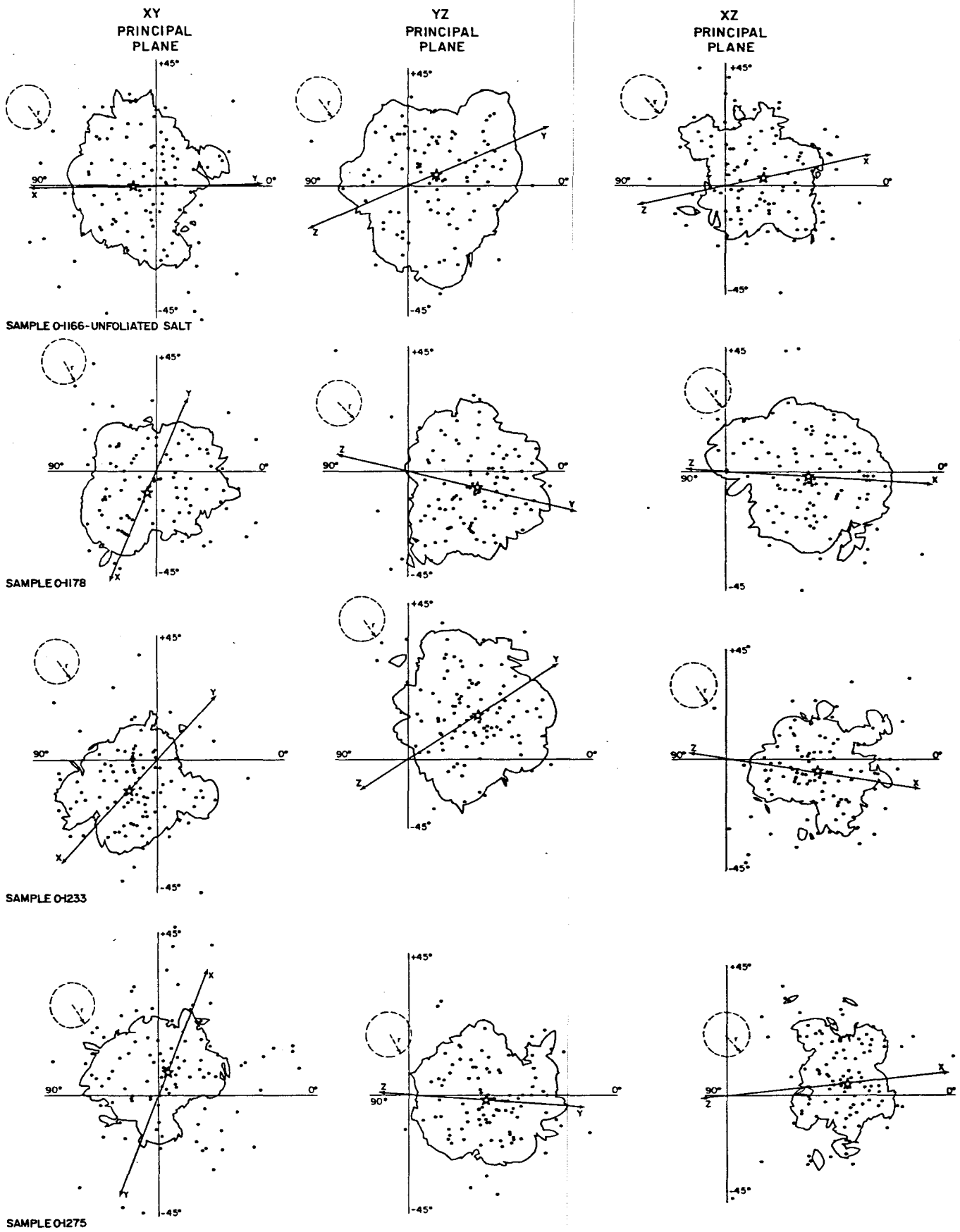


Figure 28. Strain states in rock-salt specimens O-1166, O-1178, O-1233, and O-1275 on the shape-factor grid. See figure 29 for key and scale.

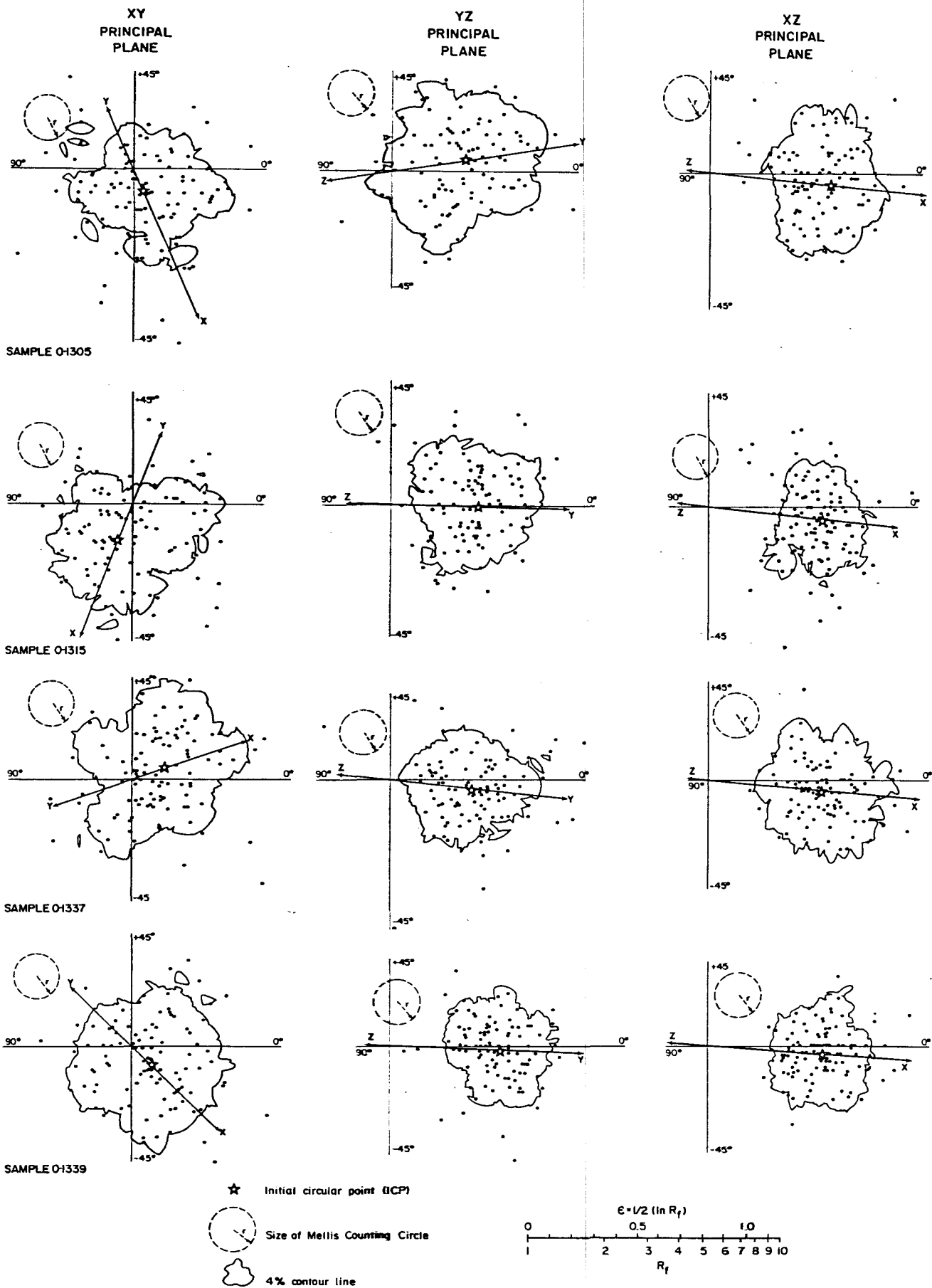
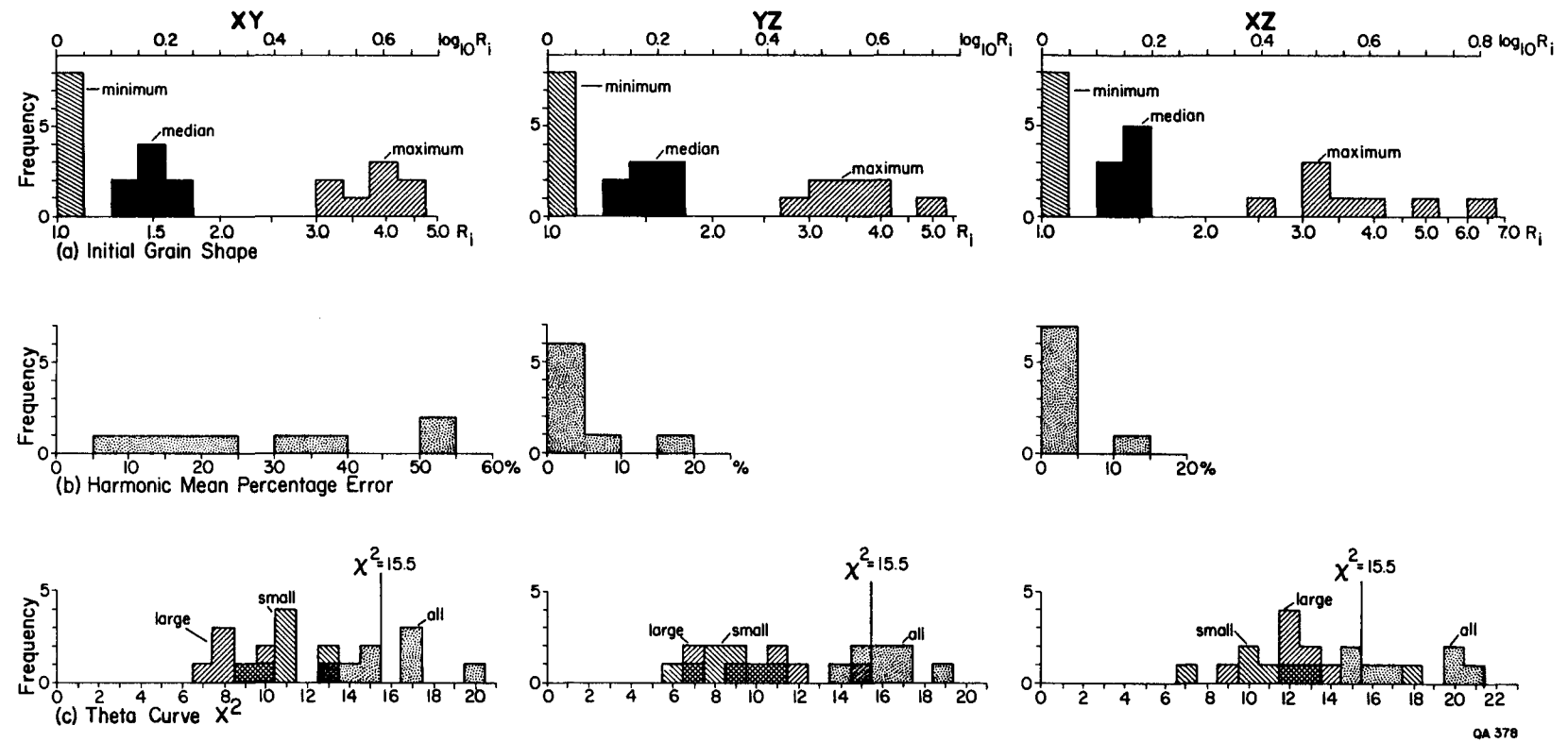


Figure 29. Strain states in rock-salt specimens O-1305, O-1315, O-1337, and O-1339 on the shape-factor grid.

"small grains," whereas the full sample is termed "all grains." All strain ratios shown have been corrected by internal checks, described in the following section on three-dimensional strains.

The harmonic mean invariably provides an overestimate of the strain ratio (Lisle, 1977b, 1979). If the strain ratio, R_s , and the initial grain shape, R_i , are known, the error can be calculated. Figure 30A shows the maximum, minimum, and median axial ratio in each data sample before the grains were deformed, (referred to as initial grains) as calculated by program THETA. Although the maximum initial grain axial ratio varies widely in each of the principal strain planes XY, YZ, and XZ, the median value is remarkably constant at $R_i \approx 1.5$. Using estimates of strain ratios from the Theta Curve Method, the expected percentage error, or overestimate, of the harmonic mean, can be obtained for each of the principal strain planes, using Lisle's (1979) figure 2. Histograms of these errors are shown in figure 30b. Predictably, because the median value of the initial grain shape is uniform, the error is almost entirely controlled by the strain ratio. Thus, the more highly strained YZ and XZ sections have much lower error than the XY foliation plane. This characteristic was exploited in the integration of the results into three dimensions (following section). These expected errors are similar to the actual discrepancies of the YZ and XZ strain ratios obtained by the Harmonic Mean and Theta Curve Methods (table 4). Confidence in both methods is therefore increased.

The Theta Curve Method of Lisle (1977a) and Peach and Lisle (1979) allows the reliability of the unstraining procedure to be statistically tested by the χ^2 test for randomness. Figure 30c summarizes the results of these tests. At least half the unstrained "all grains" population exceed the specified χ^2 limit (for eight degrees of freedom, 10 classes) of 15.5: they are not statistically random. This nonrandomness could have two causes: either the grains were not randomly oriented before strain, or strain was inhomogeneous at the scale of the specimens. It is demonstrated below that the first proposition is invalid. What of the second? After splitting the "all grains" population into equal numbers of "large grains" and "small grains", almost all the χ^2 values fall below the limit of 15.5 (fig. 30C), indicating the validity of

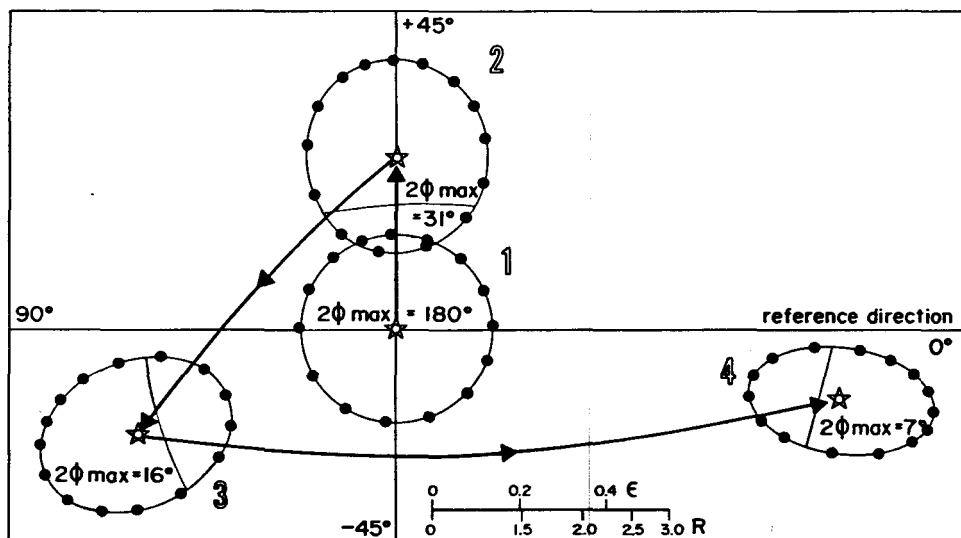
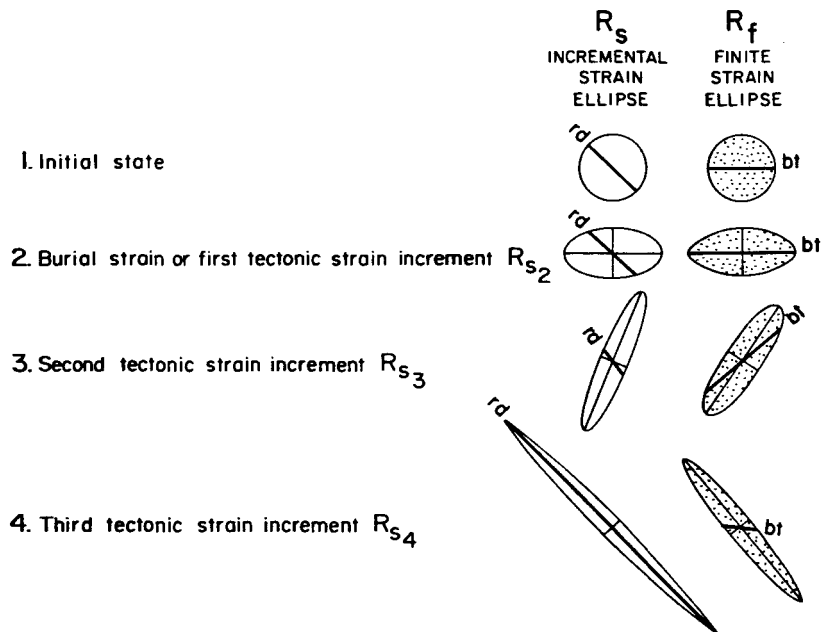


QA 378

Figure 30. Error analysis in histogram form of strain data of 2,400 grains in the eight specimens. (A) Initial grain shapes calculated by program THETA. The median initial axial ratio was 1.5 in all three principal planes of strain. (B) Percentage overestimate of strain by the harmonic-mean method. The error increases with increase of initial grain axial ratios, R_i , and decreases with increase of imposed strain, R_s . (C) χ^2 tests for randomness by program THETA. Half of the "all grains" samples exceed the χ^2 limit of 15.5. But if separated into "large grains" and "small grains," almost all samples fall below the χ^2 limit.

the test. Thus, if treated as separate populations, the large and small grains strained homogeneously. But combined into a single population, the strain is inhomogeneous in half the cases. Because the finite strains calculated for the "all grains", "large grains", and "small grains" populations are similar, (table 4) the results of the "all grains" populations can be accepted as substantially correct, particularly as they are similar to the results of the Shape Factor Grid Method.

The Shape Factor Grid Method was designed to test for the existence of preferred orientation (nonrandomness) in initial fabrics. Elliott (1970) demonstrated how a clastic rock with an initially unimodal fabric would yield delta-shaped or heart-shaped distributions on the shape factor grid; such distributions are recognizable after superimposed tectonic strain. These distributions arise because thin ellipses (large axial ratios) are better oriented (lower ϕ range) by currents or mass flow than are fat ellipses (small axial ratios). However, these distributions are produced in clastic sediments rather than in chemical precipitates (though it may also be common in igneous rocks that have undergone viscous flow before cooling). Thus, it is inapplicable to rock salt, even though some of the plots suggest deltas (e.g., O-1315 XY in fig. 29). Nor can deltoid distributions result from the effects of compactional strain, superimposed tectonic strain, or both. Figure 31 shows how an initially random distribution, which is circular, can only produce elliptical distributions, no matter how many times the rock is strained, regardless of whether the rock had a pre-tectonic burial strain. Thus, only elliptical distributions are possible in evaporites. The absence of initial preferred orientation is also indicated by the close similarities between the calculated initial grain shapes and χ^2 values for differently oriented sections through the sample. Compare the XY, YZ, and XZ values in figure 30A, C. Differently oriented sections would be expected to yield different initial values if there was initial anisotropy.



- Elliptical particle defining distribution
 - ★ Initial circular point
 - Deformation path of initial circular point
 - Distribution of elliptical particles
- R = axial ratio of strain ellipse or elliptical particle
 $\epsilon = 1/2 \ln R$
 $2\phi_{max}$ = fluctuation
 rd = reference direction
 bt = bedding trace

Figure 31. Theoretical fabrics produced by homogeneous strains of a model sample of elliptical particles on the shape-factor grid. An initially random distribution, defining a circular field at the graph's origin, is deformed to form an elliptical field by burial or tectonic strain. Subsequently superimposed strains produce only elliptical fields. Strain ellipses above show how a finite, or total, strain can be less than even one of the incremental strains that built up the finite strain.

Three-dimensional strains

For each of the eight samples, two-dimensional strains were calculated for three mutually perpendicular surfaces by the methods discussed in the previous section. Each trio was integrated to yield three-dimensional strains for each sample. Because each surface was parallel, or near parallel, to a principal plane of strain, the mathematical procedure was simple. The strains estimated in misaligned surfaces were adjusted to conform with principal planes, either graphically by using a Mohr diagram (Ramsay, 1967, p. 69-74) or mathematically by equation 3-49 (Ramsay, 1967, p. 69).

Because the measured surfaces are parallel to principal planes of strain, internal checks on the errors are available, according to the relations $X.Y.Z. = 1$ and $X/Y.Y/Z = X/Z$. The measured strains were adjusted to conform with these relations by exploiting the strengths of each method. The Harmonic Mean Method is known to be more accurate at higher R_s values (Lisle, 1977a, 1979). Thus the XY ratio was adjusted to conform to the higher strain ratios, so that $XY = XZ/YZ$. The other two methods are more accurate at low R_s values (where the fluctuation is high). Thus both XZ and YZ values were adjusted by the same proportion so that $XZ/YZ = XY$. Table 4 shows two-dimensional strain values after adjustment.

Three-dimensional strain values are shown in table 5, which also defines strain parameters. These results are graphically summarized in two deformation plots, the Flinn diagram (fig. 32, compare Flinn, 1978) and the Hsu diagram (fig. 33, compare Hossack, 1968). Both diagrams show the average strains measured by all three methods for the "all grains" population.

All the strains lie in the flattening field of deformation, in which both the large and intermediate principal axes of strain, X and Y, have extended. Figure 34 compares the results obtained by the three different methods; each method forms an apex for each of the eight triangles. Areas of the triangles (a measure of the discrepancy between methods) decrease with increasing strain, or distance away from the origin of the graph. This is probably due to the logarithmic nature of the two coordinates. In general the Shape Factor Grid Method yields

Table 5. Three-dimensional strain parameters from Oakwood salt core obtained by three different methods.

Sample Depth (ft)		1166	1178	1233	1275	1305	1315	1337	1339
THETA CURVE	All								
	lna	0.000	0.000	0.166	0.262	0.140	0.344	0.223	0.207
	lnb	0.336	0.693	0.678	0.806	0.751	0.693	0.802	0.888
	k	0.000	0.000	0.244	0.325	0.186	0.500	0.278	0.233
	%Z	10.6	37.0	39.8	46.5	42.2	43.8	45.6	48.4
	v	1.000	1.000	0.608	0.509	0.686	0.333	0.565	0.622
	E ₃	-0.112	-0.462	-0.507	-0.625	-0.548	-0.576	-0.609	-0.662
	E _s	0.274	0.566	0.632	0.787	0.678	0.747	0.762	0.823
	Large								
	lna	0.322	0.020	0.182	0.247	0.079	0.385	0.337	0.278
	lnb	0.113	0.732	0.663	0.763	0.870	0.677	0.765	0.878
	k	2.84	0.027	0.275	0.323	0.091	0.569	0.441	0.317
	%Z	16.7	39.0	39.5	44.6	45.5	44.0	46.3	49.2
	v	-0.479	0.947	0.569	0.512	0.833	0.275	0.388	0.519
	E ₃	-0.183	-0.494	-0.503	-0.591	-0.607	-0.580	-0.622	-0.677
	E _s	0.319	0.606	0.629	0.745	0.745	0.760	0.799	0.853
	Small								
	lna	0.030	0.000	0.122	0.191	0.367	0.254	0.125	0.251
	lnb	0.285	0.639	0.737	0.777	0.551	0.787	0.875	0.804
	k	0.104	0.000	0.166	0.245	0.665	0.323	0.143	0.312
	%Z	18.1	34.6	41.3	44.1	38.7	45.6	46.5	46.2
	v	0.812	1.000	0.715	0.606	0.201	0.512	0.750	0.524
	E ₃	-0.200	-0.425	-0.533	-0.582	-0.489	-0.609	-0.625	-0.620
	E _s	0.246	0.522	0.657	0.725	0.653	0.768	0.771	0.779

Table 5. (continued)

Sample Depth (ft)	1166	1178	1233	1275	1305	1315	1337	1339
All								
lna	0.017	0.135	0.105	0.349	0.350	0.255	0.329	0.222
lnb	0.538	0.732	0.809	0.806	0.754	0.844	0.802	0.928
k	0.032	0.184	0.129	0.432	0.464	0.302	0.411	0.240
%Z	30.6	41.3	43.7	48.0	46.17	47.7	47.5	50.0
v	0.938	0.689	0.771	0.397	0.366	0.536	0.417	0.613
E ₃	-0.365	-0.533	-0.574	-0.654	-0.620	-0.648	-0.644	-0.693
E _s	0.446	0.660	0.707	0.838	0.806	0.813	0.823	0.863
Large								
lna	0.034	0.100	0.062	0.381	0.283	0.291	0.442	0.172
lnb	0.490	0.738	0.818	0.768	0.825	0.791	0.713	0.963
k	0.069	0.135	0.076	0.496	0.343	0.368	0.619	0.179
%Z	28.7	40.9	43.2	47.2	47.5	46.4	46.3	50.3
v	0.871	0.762	0.859	0.337	0.489	0.462	0.235	0.696
E ₃	-0.338	-0.526	-0.566	-0.639	-0.644	-0.624	-0.622	-0.699
E _s	0.415	0.647	0.695	0.828	0.814	0.792	0.824	0.865
Small								
lna	0.072	0.171	0.149	0.314	0.411	0.217	0.190	0.174
lnb	0.553	0.726	0.801	0.847	0.688	0.899	0.909	0.932
k	0.129	0.236	0.186	0.371	0.598	0.241	0.209	0.186
%Z	32.5	41.8	44.2	48.8	44.9	48.9	48.8	37.5
v	0.771	0.618	0.686	0.459	0.252	0.612	0.654	0.686
E ₃	-0.393	-0.541	-0.583	-0.669	-0.596	-0.671	-0.669	-0.470
E _s	0.484	0.674	0.723	0.849	0.785	0.837	0.831	0.841

Table 5. (continued)

Sample Depth (ft)	1166	1178	1233	1275	1305	1315	1337	1339	
SHAPE GRID FACTOR	lna	0.145	0.163	0.262	0.262	0.185	0.384	0.312	0.273
	lnb	0.267	0.673	0.720	0.825	0.828	0.788	0.811	0.962
	k	0.544	0.243	0.364	0.318	0.224	0.487	0.384	0.284
	%Z	20.2	39.5	43.3	47.2	45.9	48.0	47.5	51.9
	v	0.295	0.609	0.466	0.517	0.634	0.345	0.445	0.558
	E ₃	-0.226	-0.503	-0.567	-0.637	-0.614	-0.654	-0.644	-0.732
	E _s	0.296	0.627	0.719	0.802	0.763	0.845	0.820	0.917

e_1, e_2, e_3 = elongations parallel to X, Y, Z

lna and lnb = natural logs of $a = (1 + e_1)/(1 + e_2)$ and $b = (1 + e_2)/(1 + e_3)$

$k = \ln a / \ln b$ = Flinn parameter

%Z = $-e_3 \cdot 100$ = percentage shortening parallel to Z

$v = (1 - k)/(1 + k) = (2E_2 - E_1 - E_3)/(E_1 - E_3) = (\ln b - \ln a)/(\ln b + \ln a)$ = Lode factor

where E_1, E_2, E_3 are logarithmic strains equal to $\ln(1 + e_1)$,
 $\ln(1 + e_2)$, $\ln(1 + e_3)$

$$E_s = \left\{ \frac{2}{3} [(\ln a)^2 + (\ln b)^2 + (\ln a \cdot \ln b)] \right\}^{1/2} = \text{natural strain}$$

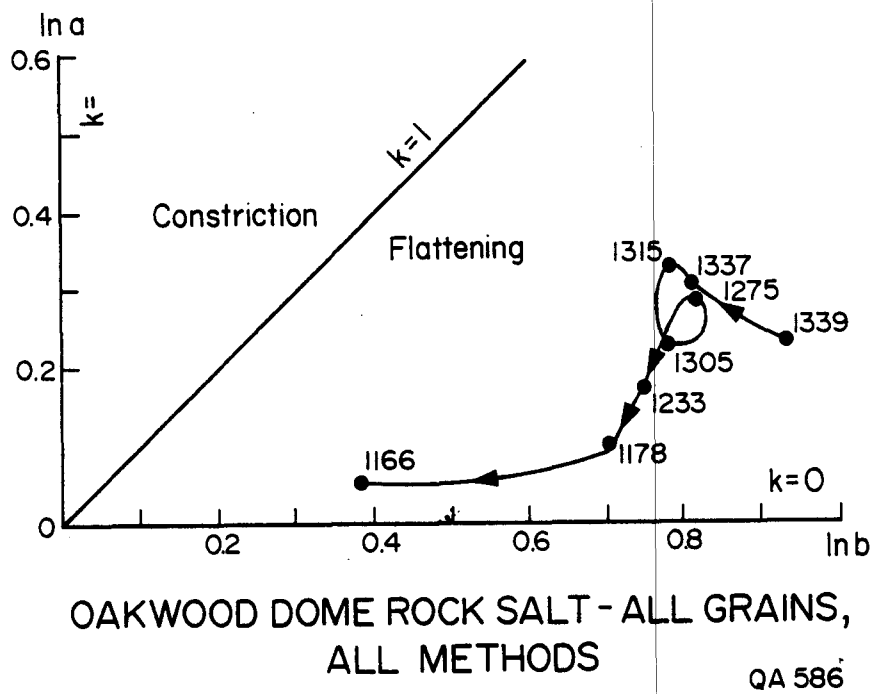
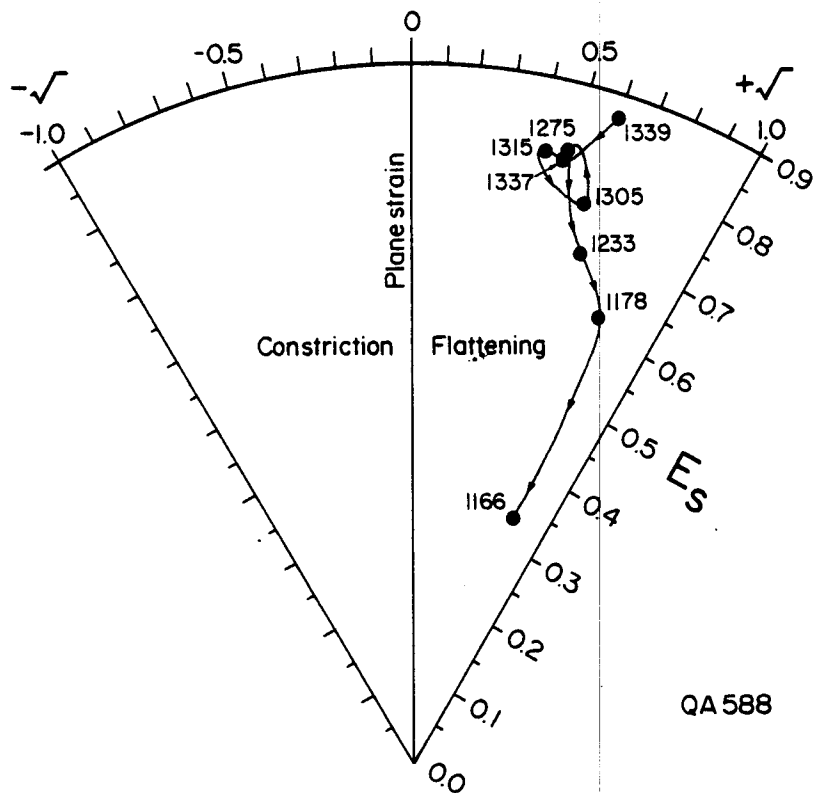


Figure 32. Flinn diagram showing the mean strain in the "all-grains" samples of halite recorded by all three methods of strain analysis. Numbers refer to sample numbers, equivalent to depths in feet. Line connecting points indicates upward trend in strain states. All samples lie in the flattening field of strain.



OAKWOOD DOME ROCK SALT - ALL GRAINS,
ALL METHODS

Figure 33. Hsu diagram showing the mean strain in the "all-grains" samples of halite recorded by all three methods of strain analysis. Numbers refer to sample numbers, equivalent to depths in feet. Line joining points indicates upward trend of strain states. All samples lie in the flattening field of strain.

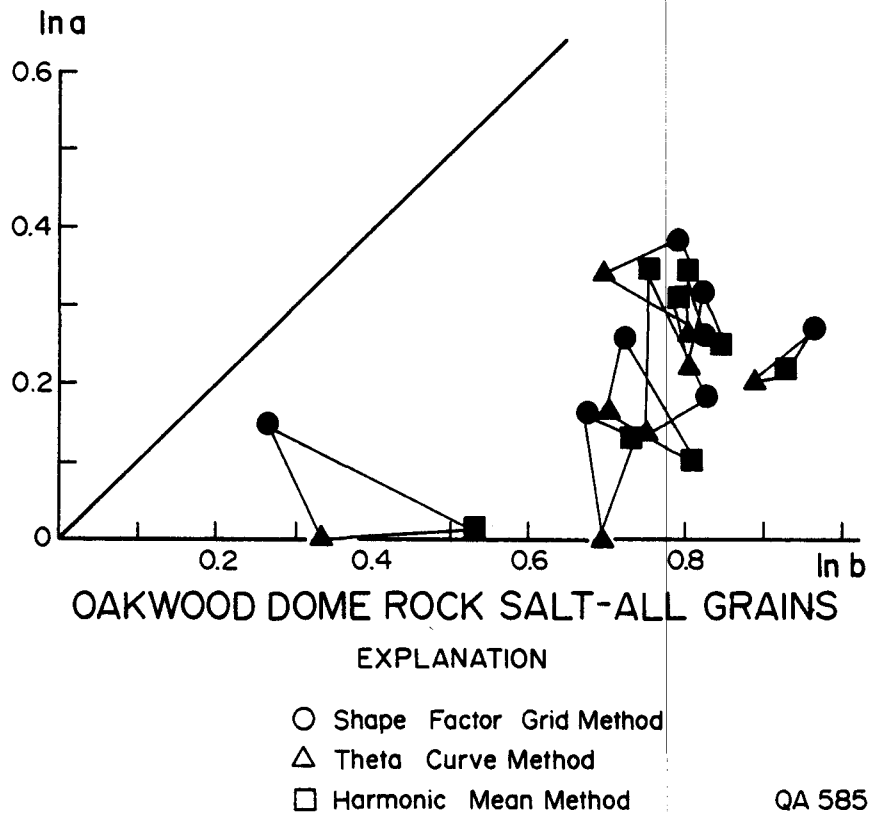
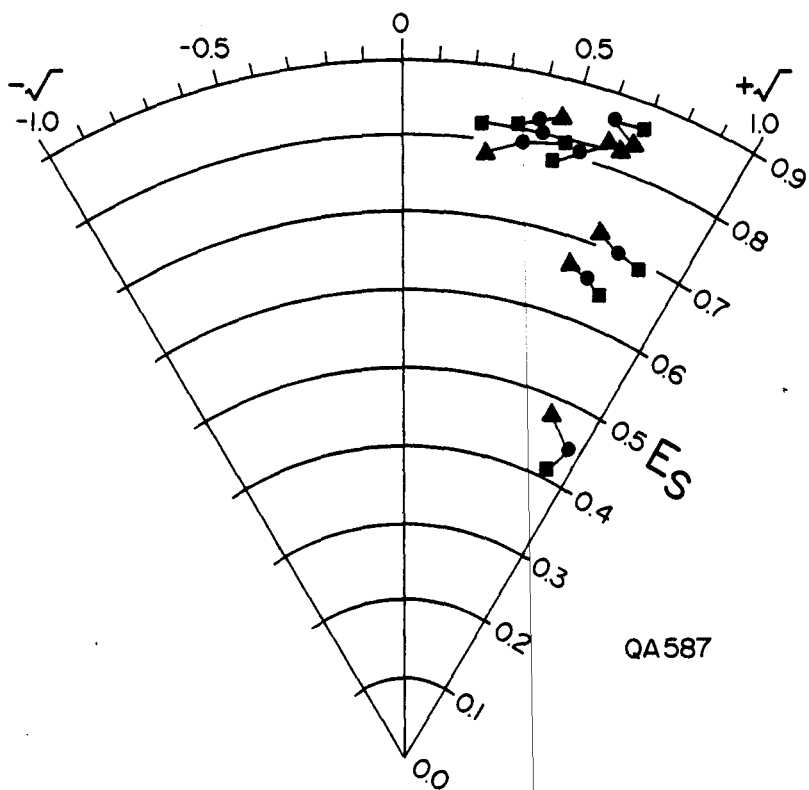


Figure 34. Flinn diagram showing triangles of discrepancy between results obtained by different methods of strain analysis on the same specimens. The lowermost harmonic-mean value can be ignored because strain in this specimen is too low for accurate results by this method.

strains with higher k values ($\ln a/\ln b$). The harmonic-mean value for unfoliated salt 1,166 ft deep can be ignored because of severe overestimation by this method at low levels of strain R_S . In general the methods show reasonable agreement, and the same trend is yielded by each method. Figure 35 compares the strains measured by the Harmonic Mean Method for the three sample groups of different-sized grains: all, large, and small grains. There, again, there is good agreement between groups. Not surprisingly the "all grains" samples are in most cases intermediate between the other two samples of each specimen analyzed. Significantly each trio of values, except for the lowest strain (nearest origin of graph), is spread out roughly parallel to contours of equal natural strain, E_S . Natural strain provides a measure of the overall strain magnitude in all three dimensions, unlike, say, maximum percentage shortening parallel to Z . Thus, the smaller grains show similar magnitudes of strain to the larger grains in any one specimen (except the least deformed). This indicates that, contrary to expectation, the smaller grains are not subgrains formed by recovery of larger, more deformed grains. They are simply smaller grains, with no evidence for a different strain history.

Variations in strain magnitude with depth are shown in figure 36. The three straight lines obtained by linear regression indicate the general trend for each method. The goodness-of-fit to a straight line was examined using the correlation coefficients (r values) for different levels of significance (Fisher and Yates, 1963, their table 8). The significance of the slope of the regression line was examined by the F test and by techniques of analysis of variance (Davis, 1973, p. 106-114, p. 192-217; Draper and Smith, 1967, p. 24-32). With regard to shortening parallel to Z (fig. 36A), all seven specimens of foliated rock salt yield strains that show a significant decrease in shortening with decreasing depth for each of the three methods. Both the linearity and slope of the regression lines are significant. Mean shortening decreases from around 50 percent in the deepest foliated salt to around 35 percent in the shallowest foliated salt. The unfoliated salt has weak strains, averaging 15 percent (ignoring the unrealistic harmonic-mean value). These strains are too weak to be visible to the eye in the fabric of the



OAKWOOD DOME ROCK SALT-
HARMONIC MEAN METHOD

EXPLANATION

- All grains
 - Large grains
 - ▲ Small grains
- } in same specimen

Contoured with lines of equal E_s

Figure 35. Hsu diagram showing strain states in the three different grain-size populations: all grains, large grains, and small grains. Natural strain intensity, E_s , increases outward from origin of plot. For the moderately to strongly deformed specimens, all three grain-size populations show similar levels of strain.

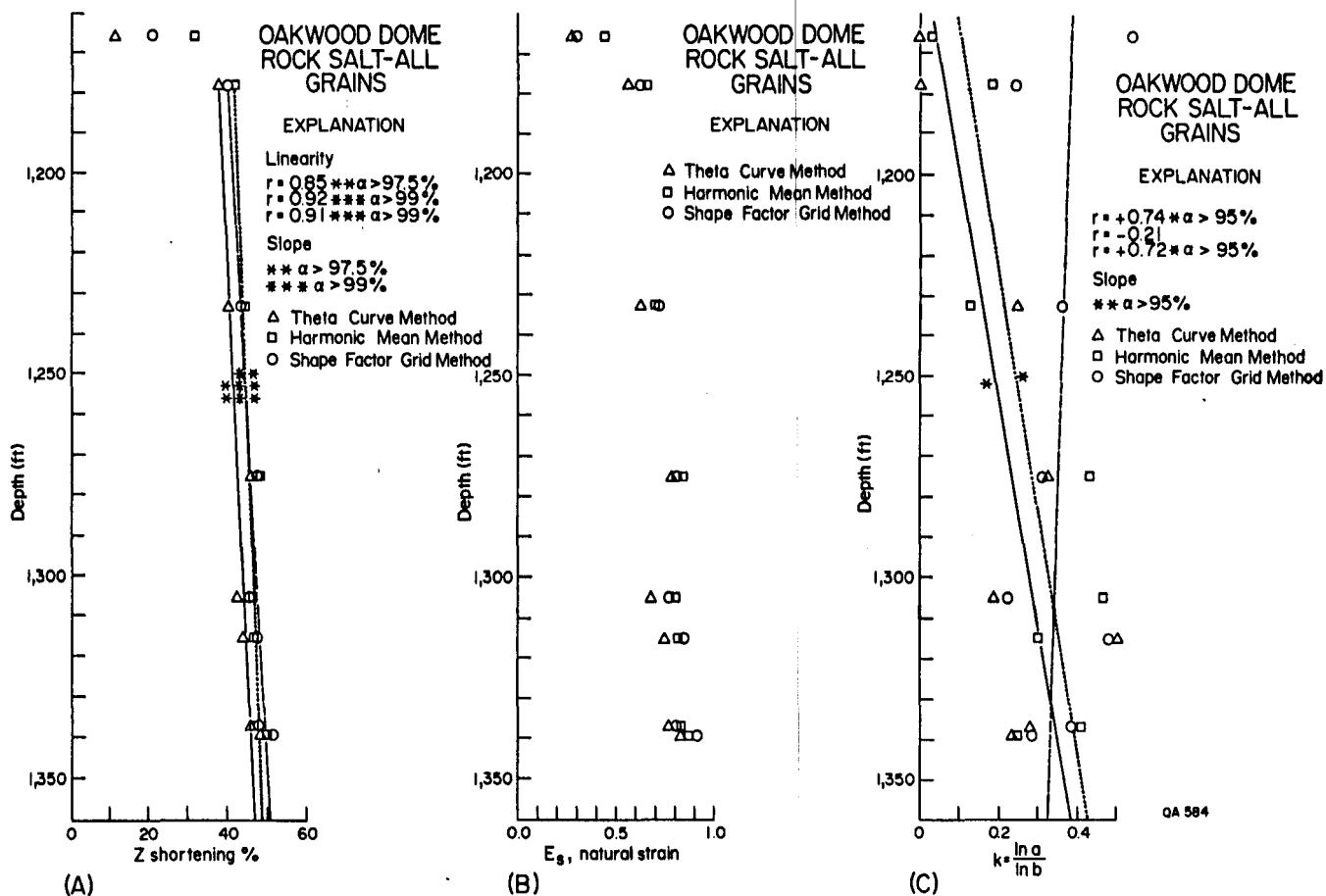


Figure 36. Variations in strain magnitude and type with depth. Regression lines for foliated rock salt have been statistically tested for linear fit to data and slope of line. Uppermost data points are from unfoliated rock salt. (A) Percentage shortening parallel to Z. (B) Natural strain. (C) k value, or ratio of constriction to flattening. Strain magnitudes and k values decrease significantly upward.

rock. Strain magnitude, as expressed by natural strain, E_S , shows virtually identical results (fig. 36B).

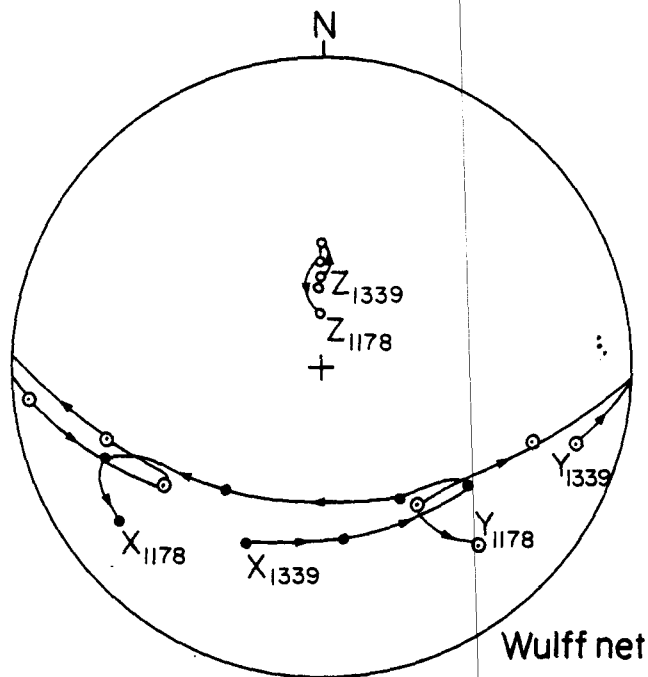
The parameters k and ν are alternative measures of the relative dominance of flattening (oblate strain ellipsoids with $k = 0$, $\nu = +1$) versus constriction (prolate strain ellipsoids with $k = \infty$, $\nu = -1$). Figures 32 and 33 show how all strains fall within the flattening field, where $0 < k < 1$ and $1 > \nu > 0$. Do k and ν vary systematically with depth? Figure 36C shows the statistically tested regression lines for each of the three methods. Two methods show significant trends of decreasing k values with decreasing depth; the third method shows no correlation between depth and k value. These results suggest that the shallower strains were characterized by more flattening and less constriction than were the deeper strains. The significance of these trends is discussed in the next section.

The orientations of the principal strains at various depths in the foliated-salt core are shown in figure 37. According to the conventions described in the section entitled "Defining orientation in nonoriented core", the XY foliation plane has been assumed to dip south toward the axis of Oakwood Dome. The uniform dip of the foliation plane is indicated by the small variation in plunge of its pole, the Z axis. The XY foliation plane steepens with depth down to 1,315 ft, below which it is progressively less steep with depth. The depth of 1,315 ft corresponds to the axial surface of an overturned, inclined synform (fig. 18). No significance is placed on this coincidence for two reasons. Firstly examination of about 65 more-closely spaced, direct readings of the foliation dip in the core, as reproduced in the appendix of Dix and Jackson (1982), shows no such trend. Secondly the overlying antiform shown in figure 18 shows no analogous change in dip of foliation at a depth of 1,278 ft. Within the foliation plane the principal extension axis, X, which marks the mineral lineation direction, varies widely from downdip at a depth of 1,338 ft to strongly oblique at depths of 1,233 ft and 1,315 ft (fig. 37). The latter depth is that below which the foliation plane becomes less steep with depth. The predominantly downdip orientation of the lineation within the foliation plane is compatible with the hypothesis discussed previously that tongues of rock salt rise predominantly updip and, presumably, outward from a central core. The obliquity of the lineation at some points (e.g. 1,233 ft and 1,315 ft) suggests that a significant component of oblique flow has also occurred, as was documented Winnfield, Weeks Island, and Grand Saline Domes in the section entitled "Assessing large-scale flow patterns from linear elements."

Significance of Measured Strains

Actual strains and measured strains

The measured strains in Oakwood rock salt are almost certainly smaller than the actual strains affecting the rock. Firstly the three methods employed all yield the minimum finite strain. As shown in figure 31 the finite strain, or end result of superimposing several strain



OAKWOOD DOME ROCK SALT

QA 589

Figure 37. Equal-angle stereographic projection (Wulff net) of the orientations of the principal axes of strain, X, Y, and Z, assuming a southward dip of the XY foliation plane. Lines connecting points indicate upward trend of orientations. The X direction of maximum extension varies widely although the XY plane containing X dips uniformly.

increments, is less than the sum of the incremental strains, apart from cases where the superimposed strains are coaxial. The actual strain can only be determined if the deformation path is known, as from syntectonic fiber growths for instance.

The second reason for lower strains is the probability of "hot working" or syntectonic recrystallization. The buildup of dislocations within crystals undergoing plastic strain causes strain hardening. Several strain-softening mechanisms counteract this buildup: (1) faster dislocation climb relative to dislocation buildup, promoted by high temperatures and low strain rates; (2) recovery by subgrain polygonization; and (3) recrystallization, or formation of new grains. Recrystallization can be divided into syntectonic recrystallization, which takes place during deformation under directed stress, and annealing recrystallization under nondirected stress.

Recrystallization generally occurs at higher temperatures than recovery, at homologous temperatures of 0.3 to 0.7; this range corresponds to an actual temperature range of 50°C to 480°C for recrystallization of halite. The crest of Oakwood salt stock is currently at a temperature of about 35°C; a temperature of 50°C is unlikely to prevail at depths shallower than 760 m, some 350 m deeper than the borehole (table 2). The base of the Oakwood salt stock is estimated to be at least 200°C. Thus whereas the crestal rock salt is presently too cool to recrystallize, it is likely to have been at a suitable temperature for syntectonic recrystallization during most of its emplacement. Because there is ample evidence in the form of folds for the existence of geologically effective differential stress, the Oakwood rock salt has almost certainly recrystallized syntectonically.

A mechanism for forming preferred orientation by this type of recrystallization in equant minerals like pyroxene and quartz--and halite--has grown out of observations on experimental deformation (Etheridge and Kirby, 1977; Ross and Nielsen, 1978; Tullis, 1977; Kern, 1977) and natural deformation (Marjoribanks, 1976; Rousell, 1976). The syntectonic new grains formed preferentially from more-highly strained grains, which tend to be less randomly oriented (White,

1976; Vernon, 1975). The probability of syntectonic recrystallization in Oakwood Dome entails that the existing grains do not record their entire deformation history, which will never be known.

The present analysis, therefore, is based on minimum finite strains in the rock salt, which record only the later deformation history of salt emplacement.

Model strains and measured strains

The Oakwood rock salt shows two upward trends through the foliated R-1 section (96 percent of the salt core): (1) decreasing natural strain and maximum shortening, and (2) decreasing k values, or increasing flattening/constriction ratios. How do these trends compare with those in experimentally modeled diapirs?

The only quantified internal strains in diapir models known to the writer are those of Dixon (1975). His models were circular or elliptical "salt" diapirs and ridgelike "gneiss" diapirs. Both types are qualitatively similar, apart from higher strains in the less viscous model "salt." But only the ridgelike geometry lends itself to quantification of the internal strains. Dixon's "gneiss" domes were studied as two-dimensional plane-strain structures from which qualitative three-dimensional strains during radial flow can be deduced. Constriction strains in the diapir trunk result from radial tangential shortening; they were replaced upward by flattening strains in the diapir crest, which extended radially and tangentially beneath its uplifted overburden. Plotted on a graph of depth versus k value, these strain states would show a trend of decreasing k values upward. This is the same trend as that observed in Oakwood Dome (fig. 36C).

The upward trend of decreasing strain with decreasing depth toward the crest of Oakwood dome (fig. 36A, B) has no counterpart in experimental models. But the crest of Oakwood Dome is not analogous to that of the experimental models. Structural evidence for truncation of the salt stock was given in the section on geometric analysis. That the agent for this truncation was ground-water dissolution is suggested by fluid-inclusion studies and by the microstructure of the rock-salt/cap-rock contact (Dix and Jackson, 1982). Thus we should compare the present

crest of Oakwood Dome not with the crests of Dixon's diapirs but with lower zones in his models. In Dixon's models WD-2 and WD-8, whose overhangs were respectively smaller and larger than that of Oakwood Dome, a "neutral" zone was situated at depths of 17-48 percent of diapir height, where strains were minimal ($1 + e < 1.1$). Below and above this "neutral" zone, the strains increased downward and upward, respectively. By approximate analogy with this model, therefore, the Oakwood crest would have truncated to a present level below this "neutral" zone.

It should be stressed that this analogy can only be approximate because (1) the model structure is ridgelike, (2) the viscosity of the buoyant layer is modeled after gneiss, which is stiffer than its overburden, unlike salt, and (3) internal strains in Oakwood Dome are much less homogeneous, as evidenced by the existence of salt tongues. Nevertheless, this model is the nearest analogy we have to the combined trends of upward decrease in both strain magnitude and k value.

Recrystallization and measured strains

The sequence of events during halite recrystallization and anhydrite cap-rock formation deduced and documented by Dix and Jackson (1982) is summarized in figure 38. This sequence portrays the most recent cycle of, perhaps, many thousands of cycles that preceded it. Each cycle is speculated to have formed a lamina in the laminated anhydrite cap rock.

Stage 1 shows the effects of vertical shortening (under vertical compressive stress greater than confining stress) caused by rise of the diapiric rock salt. The shortening produced horizontal pressure stripes and vertical dilation veins in the anhydrite cap rock. The medium-grained unfoliated salt with inclusions of disseminated anhydrite formed in the previous cycle of dissolution.

Stage 2. A further influx of water dissolved rock salt to form a cavity below the cap-rock contact, as at Gyp Hill, Winnfield, Jefferson Island, and Lake Washington Domes (O'Donnell, 1935; Taylor, 1938; p. 53-54; Hoy and others, 1962; Dutton and Kreitler, 1980). Active flow of ground water has been documented within some of these cavities (Huner, 1939, p. 221; Hoy and

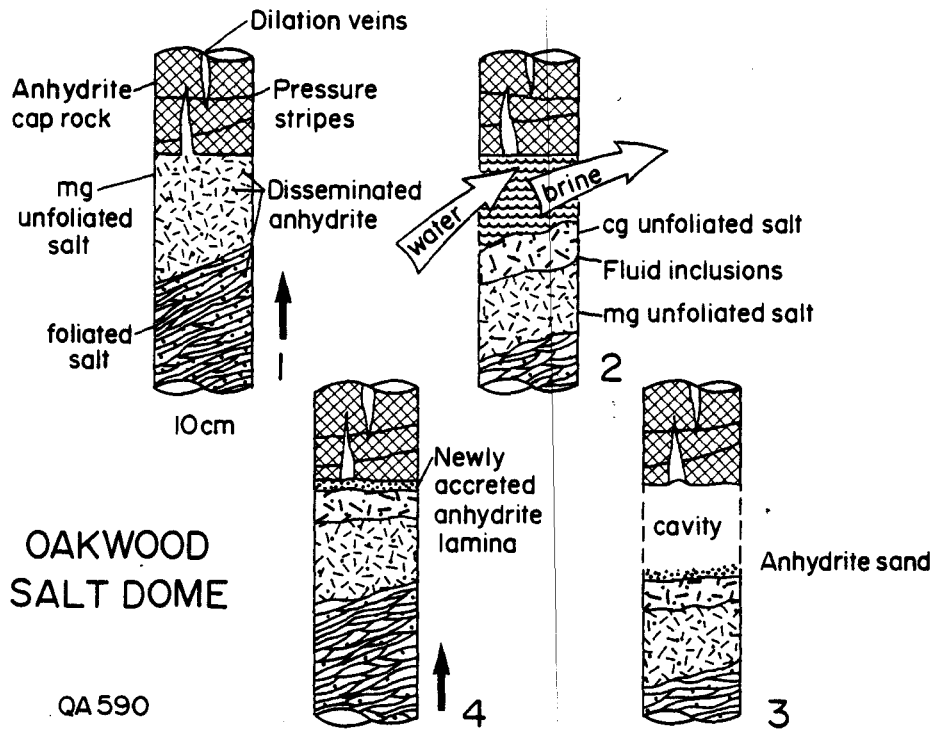


Figure 38. Schematic illustration of the model proposed by Dix and Jackson (1982) for basal accretion of anhydrite cap rock, formation and closure of a dissolution cavity, and superimposed strains in rock salt and cap rock of Oakwood Dome. See text for explanation.

others, 1962). Water penetrated the underlying Oakwood rock salt along halite grain boundaries and caused secondary recrystallization just below the cavity (forming the coarse-grained R-3 zone of unfoliated salt with abundant intracrystalline fluid inclusions), and primary recrystallization slightly deeper (forming a new zone of medium-grained unfoliated salt, the R-2 zone).

Stage 3. Anhydrite sand accumulated on the floor of the cavity as a residue from the dissolution of halite.

Stage 4. The cavity closed by diapiric rise of the salt (there is no evidence for collapse of the cap rock, nor would such collapse result in vertical principal compressive stresses). The anhydrite sand was accreted against the base of the cap rock. Forceful closure of the cavity is indicated by a tight seal of the halite-anhydrite contact, inclined shear fractures that offset the horizontal pressure stripes, and buckling of the vertical dilation veins.

The final strain increment (strain ellipsoid, E_2), induced by vertical uniaxial compression as the dissolution cavity closed, is recorded in the R-2 zone of recrystallized unfoliated salt (specimen O-1166). The total strain (strain ellipsoid, E_R), which comprises both this final strain increment and the previous strain increments, is recorded in the foliated R-1 zone (specimen O-1178 and lower specimens). Knowing the strain in E_2 and E_R , represented by 3×3 symmetric matrices, the state of strain at the top of the R-1 zone before the final strain increment can be calculated by means of the equation

$$E_R = E_2^{1/2} \cdot E_1 \cdot E_2^{1/2} \quad (\text{Flinn; 1978, eq. 13a})$$

which may be rewritten

$$E_1 = E_2^{-1/2} \cdot E_R \cdot E_2^{-1/2}$$

to solve for E_1 by matrix multiplication. This procedure allows the final part of the salt deformation path to be calculated. The strain ellipses E_1 , E_2 , and E_R are schematically illustrated in figure 39A and their orientations are shown in stereographic projection in

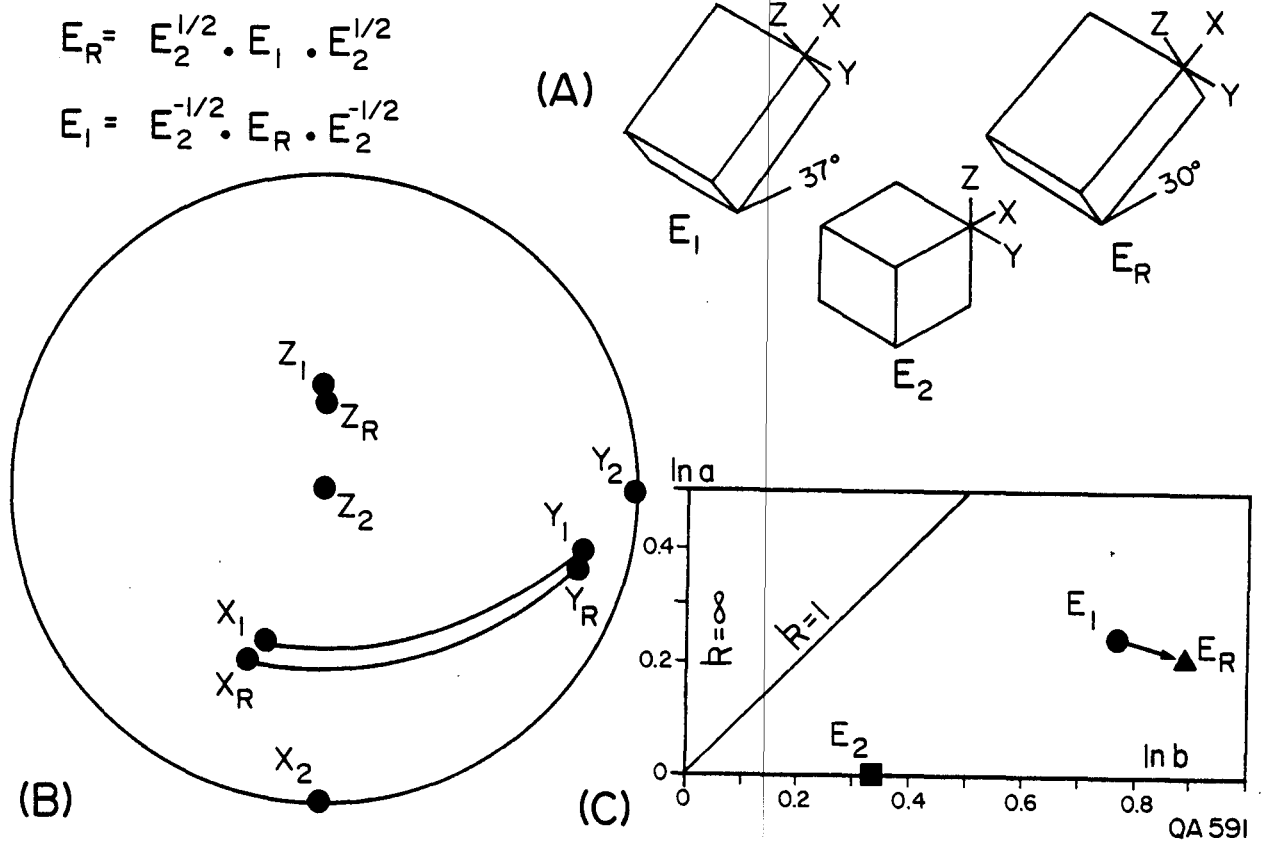


Figure 39. Quantitative modeling of superimposed strains in the crest of Oakwood Dome. E_1 is initial strain ellipsoid, E_2 is incremental strain ellipsoid, E_R is resultant, or final, strain ellipsoid. (A) Strains drawn to scale as blocks in true orientation. (B) Equal-area stereographic projection (Schmidt net) showing orientation of principal strain axes of the three strain ellipsoids. (C) Flinn diagram showing deformation path of E_1 strain ellipsoid being converted to E_R strain ellipsoid by addition of E_2 strain increment.

figure 39B. During the final strain increment, E_2 , the XY foliation plane in the uppermost foliated R-1 salt rotated from a dip of 37 degrees to 30 degrees. Figure 39C shows the deformation path on a Flinn diagram. Addition of the final strain increment, E_2 , changed E_1 to E_R by increased flattening. This increased flattening (decreasing k value) is similar to that recorded in Dixon's (1975) model diapirs.

CONCLUSIONS

Dix and Jackson (1982) concluded their report by discussing the implications of their salt-core study to isolation of nuclear waste in Oakwood Dome and in salt domes generally. All the conclusions in their complementary study are supported by the present study and need not be repeated here.

Additional findings of the present study are given below: firstly generic conclusions on the internal structure of salt domes in general, and secondly specific conclusions on the internal structure of Oakwood Dome. If similar studies are carried out on other domes, the latter group of observations may prove applicable in part to other domes as well.

- 1) Direct and indirect measurement of strain rates in Iranian salt glaciers indicate that salt flows under tiny differential stress much faster and more readily than predicted by laboratory experiments. The presence of water is essential for rapid flow, perhaps allowing flow by liquid diffusion. By inference the concentration of water in repository rock salt plays a critical role in determining rate of salt creep around mined cavities.
- 2) Contrary to widespread generalization, little of the interior of salt mines consists of vertical or near vertical structural elements: rather, dips and plunges are predominantly moderate to steep. This inclined fabric anisotropy has an important bearing on fluid flow paths and on the flow paths of salt during creep.

- 3) There is no evidence for fundamental differences between the internal structure of salt stocks in interior basins and those in the Gulf coast as has been proposed in the literature. All salt stocks studied share certain characteristics. A broad range of dissimilarities also exists.
- 4) Folding in salt domes closely follows the similar-fold model (shear folding), though many folds appear to have been initiated by buckling. The closed interference structures are sheath folds formed by intense constriction of originally gentle fold culminations and depressions.
- 5) Construction of plunge isogon maps from linear structural elements mapped in salt mines allows the flow directions of diapiric salt to be deduced. Winnfield Dome, for example, appears to have been fed by two massive tongues of rising salt, showing geometric similarity with ice lobes in piedmont glaciers, and with certain model diapirs. Unfortunately, in some salt mines, geologists measured few linear structural elements, so the data base is sparse for some domes.
- 6) Strain rates estimated for natural deformation of rock salt vary enormously over eight orders of magnitude from $10^{-8}/s$ to $10^{-16}/s$. The slowest rates characterize average uplift rates of salt diapirs over millions of years.
- 7) The Oakwood salt core has penetrated the hinge zone and lower limb of an inclined, overturned antiform. This is inferred to represent one of several salt tongues that have fed the diapir, rising upward and outward, and changing in orientation from steeply plunging folds to recumbent, overthrust folds.
- 8) Geometric analysis and strain analysis of Oakwood Dome salt core indicate severe truncation of the diapir crest, so that fold structures originally situated deep in the cap--or even the trunk--have now been bared and juxtaposed against the base of the cap rock. This truncation, almost certainly by ground-water dissolution, is an integral part of cap-rock formation, in which anhydrite sand is concentrated by dissolution of halite and repeatedly accreted against the base of the cap rock by diapiric rise of salt.

9) The uppermost part of the Oakwood salt stock is now too shallow and cool to undergo conventional recrystallization (formation of new grains). But at depths greater than about 760 m, the salt would have been able to recrystallize during its rise to the surface. On the basis of homologous temperatures, it is suggested that the water-facilitated recrystallization of the uppermost 2 m of rock salt (the R-3 zone) took place when the crest of the diapir was at least 400 m deeper than present. At present maximum erosion rates based on suspended sediment data in the area (Collins, 1982), this would be at least 3 million years ago. Bearing in mind the uncertainties of extrapolating these rates backward, active recrystallization is presently unlikely in shallow parts of shallow salt stocks. Nevertheless the resultant coarse-grained isotropic rock has great significance to rock mechanics during mining because of its radically different properties to the foliated rock salt.

10) There is no evidence that smaller halite grains in Oakwood Dome represent subgrains that have undergone less deformation than larger halite grains.

11) All the strains recorded from Oakwood are of the flattening type, and the ratio of flattening to constriction increases upward, whereas the strain intensity decreases upward. This upward decrease in strain intensity may mark the transition to an originally "neutral" zone in the diapir, since removed by dissolution during diapir truncation.

12) The orientations of maximum-extension directions in the rock-salt samples vary widely even though the foliation plane, which contains these directions, dips uniformly. Thus the preferred directions of salt creep or intergranular fluid flow are also likely to vary widely.

ACKNOWLEDGMENTS

This study is part of the East Texas Nuclear Waste Isolation Feasibility Project, which was funded by the National Waste Terminal Storage (NWTS) Program of the U.S. Department of

Energy under Contract No. DE-AC97-80ET46617 (formerly Contract No. DE-AC97-79ET-46605). The ETWI Project of the Bureau of Economic Geology is integrated with others outside Texas by the Office of Nuclear Waste Isolation (Battelle Memorial Institute, Columbus) and ERTEC (Long Beach). The TOG-1 core was supplied by Law Engineering and Testing Company under the NWTs Program.

Bruce Wilson collected the Oakwood data for halite strain analysis, assisted greatly with its processing, and provided critical discussion. Rachel Burks carried out the fold-shape analysis for folds in Grand Saline and Avery Island Domes. Michael Roberts and Arthur Goldstein assisted with the smooth running of program THETA and matrix multiplication. Useful discussions were held with Owen Dix during the early stages of this project.

I would also like to thank the following for their contribution: Virginia C. Zeikus, Jean Wilke, and Karen E. Bonnacarrere for typing; Twyla J. Coker and Dorothy C. Johnson for word processing and Fannie M. Sellingsloh for typesetting, under the direction of Lucille Harrell. Figures were drafted by Mark Bentley, Barbara Hartmann, Jamie McClelland, Margaret Evans, John Ames, Robert Baum, Richard Platt, Jeff Horowitz, Margaret Day, and Byron Holbert under the direction of Dan Scranton and James Macon.

REFERENCES

- Ala, M. H., 1974, Salt diapirism in southern Iran: American Association of Petroleum Geologists Bulletin, v. 58, no. 9, p. 1758-1770.
- American Association of Petroleum Geologists and United States Geological Survey, 1976, Subsurface temperature map of North America: scale 1:5,000,000. Alt. author: Geothermal Survey of North America Subcommittee of the AAPG Research Committee.
- Anthony, M., and Wickham, J., 1978, Finite-element simulation of asymmetric folding: Tectonophysics, v. 47, p. 1-14.
- Atwater, G. I., and Forman, M. J., 1959, Nature of growth of southern Louisiana salt domes and its effect on petroleum accumulation: American Association of Petroleum Geologists Bulletin, v. 43, no. 11, p. 2592-2622.
- Balk, R., 1937, Structural behavior of igneous rocks: Geological Society of America Memoir 5, p. 1-177.
- Balk, R., 1949, Structure of Grand Saline salt dome, Van Zandt County, Texas: American Association of Petroleum Geologists Bulletin, v. 33, no. 11, p. 1791-1829.
- Balk, R., 1953, Salt structure of Jefferson Island salt dome, Iberia and Vermilion Parishes, Louisiana: American Association of Petroleum Geologists Bulletin, v. 37, no. 11, p. 2455-2474.
- Biot, M. A., 1965, Theory of similar folding of the first and second kind: Geological Society of America Bulletin, v. 76, p. 251-258.
- Boulter, C. A., 1976, Sedimentary fabrics and their relation to strain-analysis methods: Geology, v. 4, no. 3, p. 141-146.
- Bredden, H., 1956, Die tectonische Deformation der Fossilien im Rheinischen Schiefergebirge: Deutsche Geologische Gesellschaft Zeitschrift, v. 106, p. 227-305.
- Bucher, W. H., 1956, Role of gravity in orogenesis. Geological Society of America Bulletin, v. 67, p. 1295-1318.

- Carey, S. W., 1962, Folding: Alberta Society of Petroleum Geologists Journal, v. 10, no. 3, p. 95-144.
- Carter, N. L., 1976, Steady state flow of rocks: Reviews of Geophysics and Space Physics, v. 14, no. 3, p. 301-360.
- Carter, N. L., and Hansen, F. D., 1980, Mechanical behavior of Avery Island halite: a preliminary analysis: Battelle Office of Nuclear Waste Isolation Technical Report ONWI-100, 21 p.
- Carter, N. L., and Heard, H. C., 1970, Temperature and rate dependent deformation of halite: American Journal of Science, v. 269, no. 10, p. 193-249.
- Clabaugh, P. S., 1962a, Petrofabric study of deformed salt: Science, v. 136, no. 3514, p. 389-391.
- Clabaugh, P. S., 1962b, Petrofabric analysis of salt crystals from Grand Saline salt dome: University of Texas, Austin, Master's thesis.
- Cloos, E., 1936, Der Sierra Nevada Pluton in Californien: Neues Jahrbuch für Mineralogie, Beilage, v. 13, no. 76, p. 355-450.
- Cobbold, P. R., 1977, Description and origin of banded deformation structures. I. Regional strain, local perturbations, and deformation bands: Canadian Journal of Earth Sciences, v. 14, p. 1721-1731.
- Collins, E. W., 1982, Surficial evidence of tectonic stability and erosion rates, Palestine, Keechi, and Oakwood salt domes, East Texas: The University of Texas at Austin, Bureau of Economic Geology Geological Circular 82-3, 39 p.
- Coward, M. P., 1976, Strain within ductile shear zones: Tectonophysics, v. 34, p. 181-197.
- Davis, J. C., 1973, Statistics and data analysis in geology: New York, John Wiley, 550 p.
- De Paor, D. G., 1980, Some limitations of the R_f/ϕ technique of strain analysis: Tectonophysics, v. 64, no. 1, p. T29-T31.

- Dickinson, G., 1953, Biological aspect of abnormal reservoir pressures in Gulf Coast, Louisiana: American Association of Petroleum Geologists Bulletin, v. 37, no. 2, p. 410-432.
- Dieterich, J. H., 1970, Computer experiments on mechanics of finite-amplitude folds: Canadian Journal of Earth Sciences, v. 7, p. 467-476.
- Dix, O. R., and Jackson, M.P.A., 1982, Lithology, microstructures, fluid inclusions, and geochemistry of rock salt and of the cap-rock contact in Oakwood Dome, East Texas: Significance for nuclear waste storage: The University of Texas at Austin, Bureau of Economic Geology Report of Investigations No. 120, 59 p.
- Dixon, J. M., 1975, Finite strain and progressive deformation in models of diapiric structures: Tectonophysics, v. 28, p. 89-124.
- Donaldson, I. G., 1962, Temperature gradients in the upper layers of the earth's crust due to convective water flows: Journal of Geophysical Research, v. 67, p. 3449-3459.
- Donath, F. A., and Parker, R. B., 1964, Folds and folding: Geological Society of America Bulletin, v. 75, p. 45-62.
- Draper, N. R., and Smith, H., 1967, Applied regression analysis: New York, John Wiley, 407 p.
- Dunnet, D., 1969, A technique of finite strain analysis using elliptical particles: Tectonophysics, v. 7, no. 2, p. 117-136.
- Dunnett, D., and Siddans, A.W.B., 1971, Non-random sedimentary fabrics and their modification by strain: Tectonophysics, v. 12, no. 4, p. 307-325.
- Dutton, S. P., and Kreitler, C. W., 1980, Cap rock formation and diagenesis, Gyp Hill salt dome, South Texas: Gulf Coast Association of Geological Societies Transactions, v. 30, p. 333-339.
- Eargle, D. H., 1962, Geology of core hole WP-1 Tatum Dome, Lamar County, Mississippi: U.S. Geological Survey Technical Letter Dribble - 15, Open-File Report 474-278, 46 p.
- Elliott, D., 1965, The quantitative mapping of directional minor structures: Journal of Geology, v. 73, p. 865-880.

- Elliott, D., 1968, Interpretation of fold geometry from lineation isogonic maps: *Journal of Geology*, v. 76, p. 171-190.
- Elliott, D., 1970, Determination of finite strain and initial shape from deformed elliptical objects: *Geological Society of America Bulletin*, v. 81, no. 8, p. 2221-2236.
- Escher, B. G., and Kuenen, P. H., 1929, Experiments in connection with salt domes: *Leidsche Geologische Mededeelingen*, v. 3, no. 3, p. 151-182; reviewed by D. C. Barton, 1980: *American Association of Petroleum Geologists Bulletin*, v. 4, no. 1, p. 107-108.
- Etheridge, M. A., and Kirby, S. H., 1977, Experimental deformation of rock-forming pyroxenes: recrystallization mechanisms and preferred orientation development: *American Geophysical Union Transactions*, v. 58, p. 513.
- Ewing, M., and Ewing, J. I., 1962, Rate of salt-dome growth: *American Association of Petroleum Geologists Bulletin*, v. 46, no. 5, p. 708-709.
- Fisher, R. A., and Yates, F., 1963, *Statistical tables for biological, agricultural and medical research*: Edinburgh, Oliver and Boyd, 146 p.
- Flinn, D., 1962, On folding during three-dimensional progressive deformation: *Geological Society of London Journal*, v. 118, no. 4, p. 385-433.
- Flinn, D., 1965, On the symmetry principle and the deformation ellipsoid: *Geological Magazine*, v. 102, no. 1, p. 36-45.
- Flinn, D., 1978, Construction and computation of three-dimensional progressive deformations: *Geological Society of London Journal*, v. 135, p. 291-305.
- Fry, N., 1979, Random point distributions and strain measurement in rocks: *Tectonophysics*, v. 60, no. 1/2, p. 89-105.
- Grocott, J., 1979, Shape fabrics and superimposed simple shear strain in a Precambrian shear belt, W Greenland: *Geological Society of London Journal*, v. 136, no. 4, p. 471-488.
- Hambrey, M. J., 1979, Origin of foliation in glaciers: comments on a paper by R. L. Hooke and P. J. Hudleston: *Journal of Glaciology*, v. 21, p. 556-558.

- Hanna, S. S., and Fry, N., 1979, A comparison of methods of strain determination in rocks from southwest Dyfed (Pembrokeshire) and adjacent areas: *Journal of Structural Geology*, v. 1, no. 2, p. 155-162.
- Harrison, J. V., 1930, The geology of some salt plugs in Laristan (Southern Persia): *Geological Society of London Quarterly Journal*, v. 86, p. 463-522.
- Henderson, J. R., 1981, Structural analysis of sheath folds with horizontal X-axes, northeast Canada: *Journal of Structural Geology*, v. 3, no. 3, p. 203-210.
- Holmes, A., 1965, *Principles of physical geology*, Second Edition: London, Thomas Nelson, 1288 p.
- Hooke, R. LeB., and Hudleston, P. J., 1978, Origin of foliation in glaciers: *Journal of Glaciology*, v. 20, p. 285-299.
- Hooke, R. LeB., and Hudleston, P. J., 1980: Ice fabrics in a vertical flow plane, Barnes Ice Cap, Canada; *Journal of Glaciology*, v. 25, no. 92, p. 195-214.
- Hossack, J. R., 1968, Pebble deformation and thrusting in the Bygdin area (southern Norway): *Tectonophysics*, v. 5, no. 4, p. 315-339.
- Howard, J. C., 1971, Computer simulation models of salt domes: *American Association of Petroleum Geologists Bulletin*, v. 55, no. 3, p. 495-513.
- Howe, H. V., and Moresi, C. K., 1931, *Geology of Iberia Parish*: Louisiana Geological Survey, *Geological Bulletin* 1, 187 p.
- Hoy, R. B., Foose, R. M., and O'Neill, B. J., Jr., 1962, Structure of Winnfield salt dome, Winn Parish, Louisiana: *American Association of Petroleum Geologists Bulletin*, v. 46, no. 8, p. 1444-1459.
- Hudleston, P. J., 1973a, Fold morphology and some geometrical implications of theories of fold development: *Tectonophysics*, v. 16, p. 1-46.
- Hudleston, P. J., 1973b, The analysis and interpretation of minor folds developed in the Moine rocks of Monar, Scotland: *Tectonophysics*, v. 17, p. 89-132.

- Hudleston, P. J., 1976, Recumbent folding in the base of the Barnes Ice Cap, Baffin Island, Northwest Territories, Canada: Geological Society of America Bulletin, v. 87, p. 1684-1692.
- Hudleston, P. J., 1977, Similar folds, recumbent folds, and gravity tectonics in ice and rocks: Journal of Geology, v. 85, p. 113-122.
- Hudleston, P. J., 1980, The progressive development of inhomogeneous shear crystallographic fabric in glacial ice: Journal of Structural Geology, v. 2, no. 1/2, p. 189-196.
- Hudleston, P. J., and Hooke, R. LeB., 1980, Cumulative deformation in the Barnes Ice Cap and implications for the development of foliation: Tectonophysics, v. 66, p. 127-146.
- Hudleston, P. J., and Stephansson, O., 1973, Layer shortening and fold-shape development in the buckling of single layers: Tectonophysics, v. 17, p. 299-321.
- Huner, J., Jr., 1939, Geology of Caldwell and Winn Parishes: Louisiana Geological Survey Bulletin 15, 356 p.
- Jackson, M.P.A., 1981a, Strain analysis of halite in the Oakwood core, in Kreitler, C. W., and others, Geology and geohydrology of the East Texas Basin: A report on the progress of nuclear waste isolation feasibility studies (1980): The University of Texas at Austin, Bureau of Economic Geology Geological Circular 81-7, p. 183-187.
- Jackson, M.P.A., 1981b, Upward flow of diapiric rock salt and the formation of anhydrite cap rock in Oakwood Dome, East Texas: Geological Society of America Abstracts with Programs, v. 13, no. 7, p. 479.
- Jackson, M.P.A., and Dix, O. R., 1981, Geometric analysis of macroscopic structures in Oakwood salt core, in Kreitler, C. W. and others, Geology and geohydrology of the East Texas Basin: A report on the progress of nuclear waste isolation feasibility studies (1980): The University of Texas at Austin, Bureau of Economic Geology Geological Circular 81-7, p. 177-182.

- Jackson, M.P.A., and Seni, S. J., 1983, Geometry and evolution of salt structures in a marginal rift basin of the Gulf of Mexico, East Texas: *Geology*, in press.
- Kent, P. E., 1966, Temperature conditions of salt dome intrusions: *Nature*, v. 211, no. 5056, p. 1387.
- Kent, P. E., 1970, The salt plugs of the Persian Gulf region: *Leicester Literary and Philosophical Society Transactions*, v. 64, p. 56-88.
- Kent, P. E., 1979, The emergent Hormuz salt plugs of southern Iran: *Journal of Petroleum Geology*, v. 2, no. 2, p. 117-144.
- Kern, H., 1977, Preferred orientation of experimentally deformed limestone, marble, quartzite, and rock salt at different temperatures and states of stress: *Tectonophysics*, v. 39, p. 103-120.
- Kreitler, C. W., and Muehlberger, W. R., 1981, Geochemical analyses of salt, Grand Saline Dome, East Texas, in Kreitler, C. W. and others, *Geology and geohydrology of the East Texas Basin: A report on the progress of nuclear waste isolation feasibility studies (1980): The University of Texas at Austin, Bureau of Economic Geology Geological Circular 81-7*, p. 188-194.
- Kupfer, D. K., 1962, Structure of Morton Salt Company mine, Weeks Island salt dome, Louisiana: *American Association of Petroleum Geologists Bulletin*, v. 46, p. 1460-1467.
- Kupfer, D. H., 1968, Relationship of internal to external structure of salt domes: *American Association of Petroleum Geologists Memoir 8*, p. 79-89.
- Kupfer, D. H., 1970, Mechanism of intrusion of Gulf Coast salt in D. H. Kupfer, ed., *Proceedings of Symposium on Geology and Technology of Gulf Coast Salt: Baton Rouge, Louisiana State University, School of Geoscience*, p. 25-66.
- Kupfer, D. H., 1974, Boundary shear zones in salt stocks, in A. H. Coogan (ed.), *Fourth Symposium on Salt: Cleveland, Ohio, Northern Ohio Geological Society*, v. 1, p. 215-225.

- Kupfer, D. H., 1976, Shear zones inside Gulf Coast salt stocks help delineate spines of movement: *American Association of Petroleum Geologists Bulletin*, v. 60, no. 9, p. 1434-1447.
- Laing, W. P., 1977, Structural interpretation of drill core from folded and cleaved rocks: *Economic Geology*, v. 72, p. 671-685.
- Le Theoff, B., 1979, Non-coaxial deformation of elliptical particles: *Tectonophysics*, v. 53, no. 1/2, p. T7-T13.
- Lisle, R. J., 1977a, Clastic grain shape and orientation in relation to cleavage from the Aberystwyth Grits, Wales: *Tectonophysics*, v. 39, no. 1-3, p. 381-395.
- Lisle, R. J., 1977b, Estimation of the tectonic strain ratio from the mean shape of deformed elliptical markers: *Geologie en Mijnbouw*, v. 56, no. 2, p. 140-144.
- Lisle, R. J., 1979, Strain analysis using deformed pebbles: the influence of initial pebble shape: *Tectonophysics*, v. 60, no. 3/4, p. 263-277.
- Lister, G. S., and Price, G. P., 1978, Fabric development in a quartz-feldspar mylonite: *Tectonophysics*, v. 49, p. 37-78.
- Lotze, F., 1957, *Steinsalz und Kalisalze*, Pt. I: Berlin, Gebrüder Borntraeger, 466 p.
- Marjoribanks, R. W., 1976, The relation between microfabric and strain in a progressively deformed quartzite sequence from Central Australia: *Tectonophysics*, v. 32, p. 269-294.
- Martin, R. G., 1980, Distribution of salt structures, Gulf of Mexico, Sheet 2: U.S. Geological Survey, Miscellaneous Field Studies Map MF-1213, scale 1:2,500,000.
- Martinez, J. D., Thoms, R. L., Kolb, C. R., Kumar, M. B., Wilcox, R. E., and Newchurch, E. J., 1978, An investigation of the utility of Gulf Coast salt domes for the storage or disposal of radioactive wastes, Volume 1: Louisiana State University, Institute for Environmental Studies Contract Report EW-78-C-05-5941/53, 390 p.
- Matthews, P. E., Bond, R. A. B., and Van den Berg, J. J., 1974, An algebraic method of strain analysis using elliptical markers: *Tectonophysics*, v. 24, no. 1, p. 31-67.

- Minnigh, L. D., 1979, Structural analysis of sheath-folds in a meta-chert from the Western Italian Alps: *Journal of Structural Geology*, v. 1, no. 4, p. 275-282.
- Muehlberger, W. R., 1959, Internal structure of the Grand Saline salt dome, Van Zandt County, Texas: University of Texas, Bureau of Economic Geology Report of Investigations No. 38, 23 p.
- Muehlberger, W. R., and Clabaugh, P. S., 1968, Internal structure and petrofabrics of Gulf Coast salt domes: *American Association of Petroleum Geologists Memoir* 8, p. 90-98.
- Mukhopadhyay, D., and Sengupta, S., 1979, "Eyed folds" in Precambrian marbles from southeastern Rajasthan, India: *Geological Society of America Bulletin*, Part I, v. 90, p. 397-404.
- Nance, D., and Wilcox, R. E., 1979, Lithology of the Rayburn's Dome salt core: Louisiana State University, Institute for Environmental Studies, 307 p.
- Nance, D., Rovik, J., and Wilcox, R. E., 1979, Lithology of the Vacherie salt dome core: Louisiana State University, Institute for Environmental Studies, 343 p.
- O'Donnell, L., 1935, Jefferson Island salt dome, Iberia Parish, Louisiana: *American Association of Petroleum Geologists Bulletin*, v. 19, no. 11, p. 1602-1644.
- Peach, C. J., and Lisle, R. J., 1979, A Fortran IV program for the analysis of tectonic strain using deformed elliptical markers: *Computers and Geosciences*, v. 5, no. 3/4, p. 325-334.
- Pfiffner, O. A., and Ramsay, J. G., 1982, Constraints on geological strain rates: Arguments from finite strain states of naturally deformed rocks: *Journal of Geophysical Research*, v. 87, no. B1, p. 311-321.
- Quinquis, H., Audren, C., Brun, J. P., and Cobbold, P. R., 1978, Intense progressive shear in Ile de Groix blueschists and compatibility with subduction or obduction: *Nature*, v. 273, p. 43-45.
- Ragan, D. M., 1969, Structures at the base of an ice fall: *Journal of Geology*, v. 77, p. 647-667.

- Ramberg, H., 1981, Gravity, deformation and the Earth's crust in theory, experiments and geological application, Second Edition: London, Academic Press, 452 p.
- Ramsay, J. G., 1967, Folding and fracturing of rocks: New York, McGraw-Hill, 568 p.
- Ramsay, J. G., 1976, Displacement and strain: Royal Society of London Philosophical Transactions, Series A, v. 283, p. 3-25.
- Ramsay, J. G., 1980, Shear zone geometry: a review: Journal of Structural Geology, v. 2, no. 1/2, p. 83-99.
- Ramsay, J. G., and Allison, I., 1979, Structural analysis of shear zones in an alpinised Hercynian Granite: Schweizerische Mineralogische Petrographische Mitteilungen 59, p. 251-279.
- Ramsay, J. G., and Graham, R. H., 1970, Strain variation in shear belts: Canadian Journal of Earth Sciences, v. 7, p. 786-813.
- Reynolds, E., and Gloyna, E. F., 1960, Reactor fuel waste disposal project, Permeability of rock salt and creep of underground cavities, final report: University of Texas, Austin, 40 p.
- Rickard, M. J., 1971, A classification diagram for fold orientations: Geological Magazine, v. 108, p. 23-26.
- Rogers, G. S., 1918, Intrusive origin of the Gulf Coast salt domes: Economic Geology, v. 13, p. 447-485.
- Rondeel, H. E., and Storbeck, F., 1978, Errors in geological compass determinations of the attitude of planar structures: Geologische Rundschau, v. 67, no. 3, p. 913-919.
- Ross, J. V., and Nielsen, K. C., 1978, High temperature flow of wet polycrystalline enstatite: Tectonophysics, v. 44, p. 233-262.
- Rousell, D. H., 1976, Preferred crystallographic orientation of quartz from deformed quartzite breccia of the Onaping Formation, Sudbury Basin: Canadian Journal of Earth Sciences, v. 13, p. 1347-1350.
- Sannemann, D., 1968, Salt-stock families in northwestern Germany: American Association of Petroleum Geologists, Memoir 8, p. 261-270.

- Sarkar, S., Chanda, S. K., and Bhattacharyya, A., 1982, Soft-sediment deformation fabric in the Precambrian Bhandar oolite, central India: *Journal of Sedimentary Petrology*, v. 52, no. 1, p. 95-107.
- Schwerdtner, W. M. 1966, Preferred orientation of halite in a "saltseismogram": *Proceedings of the Second Symposium on Salt*, Cleveland, Ohio, p. 70-84.
- Schwerdtner, W. M., 1967, Intragranular gliding in domal salt: *Tectonophysics*, v. 5, no. 5, p. 353-380.
- Schwerdtner, W. M., Bennett, P. J., Jones, T. W., 1977, Application of L-S fabric scheme to structural mapping and paleostrain analysis: *Canadian Journal of Earth Sciences*, v. 14, p. 1021-1032.
- Selig, F., and Wallick, G. C., 1966, Temperature distribution in salt domes and surrounding sediments: *Geophysics*, v. 31, no. 2, p. 346-361.
- Seni, S. J., and Jackson, M.P.A., 1983, Sedimentary record of Cretaceous and Tertiary salt movement, East Texas Basin: Times, rates, and volumes of salt flow, implications to nuclear-waste isolation and petroleum exploration: The University of Texas at Austin, Bureau of Economic Geology Report of Investigations (in press).
- Serata, S., and Gloyne, E. F., 1959, Development of design principle for disposal of reactor fuel waste into underground salt cavities, Reactor Fuel Waste Disposal Project: University of Texas, Austin, 173 p.
- Sharp, R. P., 1958, Malaspina Glacier, Alaska: *Geological Society of America Bulletin* v. 69, p. 617-646.
- Shimamoto, T., and Ikeda, Y., 1976, A simple algebraic method for strain estimation from deformed ellipsoidal objects. 1. Basic theory: *Tectonophysics*, v. 36, no. 4, p. 315-337.
- Siddans, A. W. B., 1980, Analysis of three-dimensional, homogeneous, finite strain using ellipsoidal objects: *Tectonophysics*, v. 64, no. 1, p. 1-16.

- Sprague, D., and Pollack, H. N., 1980, Heat flow in the Mesozoic and Cenozoic: *Nature*, v. 285, no. 5764, p. 393-395.
- Talbot, C. J., 1974, Fold nappes as asymmetric mantled gneiss domes and ensialic orogeny: *Tectonophysics*, v. 24, p. 259-276.
- Talbot, C. J., 1977, Inclined and asymmetric upward-moving gravity structures: *Tectonophysics*, v. 42, p. 159-181.
- Talbot, C. J., 1978, Halokinesis and thermal convection: *Nature*, v. 273, p. 739-741.
- Talbot, C. J., 1979, Fold trains in a glacier of salt in southern Iran: *Journal of Structural Geology*, v. 1, no. 1, p. 5-18.
- Talbot, C. J., 1981, Sliding and other deformation mechanisms in a glacier of salt, S Iran, in K. R. McClay and N. J. Price, eds., *Thrust and nappe tectonics*: Oxford, Geological Society of London, p. 173-183.
- Talbot, C. J., and Rogers, E. A., 1980, Seasonal movements in a salt glacier in Iran: *Science*, v. 208, April 25, p. 395-397.
- Talbot, C. J., Tully, C. P., and Woods, P. J. E., 1982, The structural geology of Boulby (Potash) Mine, Cleveland, United Kingdom: *Tectonophysics*, v. 85, p. 167-204.
- Taylor, R. E., 1938, Origin of the cap rock of Louisiana salt domes: *Louisiana Geological Survey Bulletin* 11, 191 p.
- Thiessen, R. L., and Means, W. D., 1980, Classification of fold interference patterns: a re-examination: *Journal of Structural Geology*, v. 2, no. 3, p. 311-316.
- Trusheim, F., 1960, Mechanism of salt migration in northern Germany: *American Association of Petroleum Geologists Bulletin*, v. 44, no. 9, p. 1519-1540.
- Tullis, J., 1977, Preferred orientation of quartz produced by slip during plane strain: *Tectonophysics*, v. 39, p. 87-102.
- Turk, Kehle and Associates, 1978, Tectonic framework and history, Gulf of Mexico region: Report prepared for Law Engineering Testing Co., Marietta, Georgia, 29 p.

- Vernon, R. H., 1975, Deformation and recrystallization of a plagioclase grain: *American Mineralogist*, v. 6, p. 884-888.
- Washburn, B., 1935, Morainic bandings of Malaspina and other Alaskan glaciers: *Geological Society of America Bulletin*, v. 46, no. 12, p. 1876-1890.
- Wegmann, C. E., 1963, Tectonic patterns at different levels: *Geological Society of South Africa (A. L. du Toit Memorial Lecture no. 8)*, v. 66 (annex), p. 1-78.
- Wenkert, D. D., 1979, The flow of salt glaciers: *Geophysical Research Letters*, v. 6, no. 6, p. 523-526.
- Wynne-Edwards, H. R., 1963, Flow folding: *American Journal of Science*, v. 261, no. 11, p. 793-814.

FIGURE CAPTIONS

Figure 1. Homogeneous change in thickness from t to t' of a stippled layer in a matrix of similar viscosity by uniform simple shear parallel to x . (A) Thickening. (B) Thinning. (C) Thickening followed by thinning. (Adapted from Ramsay, 1980.)

Figure 2. Photograph of low-temperature mylonite comprising porphyroclasts and highly strained streaks of competent, pale, sandstone in an incompetent matrix of dark rock salt. Vertical rock face in underground mine, Avery Island Dome, Louisiana. Width of view is 0.5 m.

Figure 3. Fold-shape analysis and classification of folds. (A) Fold profile showing dip isogon (α) connecting points of equal dip, orthogonal thickness (t) and thickness parallel to the axial trace (T). Subscript refers to dip of tangents on folded surfaces measured from normal to axial trace. (B) Plot of $t'^2/\cos^2 \alpha$ showing classification of folds on the basis of orthogonal-thickness changes. Each quarter-wavelength fold plots as a (theoretically) straight line originating at the point (1,1). (C) Representative examples of each class of folds: Class 1, dip isogons converge to core of fold; Class 2 isogons are parallel; Class 3, isogons diverge. Subclasses of Class 1 are differentiated by their $t'^2/\cos^2 \alpha$ values, as in (B). (Adapted from Ramsay, 1967, figs. 7-18, 7-24, 7-25, and Hudleston, 1973a.)

Figure 4. Fold-shape analysis of large folds defined by disseminated-anhydrite layers in underground salt mines in Grand Saline Dome, East Texas, and Avery Island Dome, Louisiana. Left, fold profiles showing dip isogons (Grand Saline example from Muehlberger, 1959, Plate 5). Right, $t'^2/\cos^2 \alpha$ plots of 16 quarter-wavelength folds. Each plot is represented by a linear regression line. The high correlation coefficients (r) indicate close conformation to ideal folded surfaces. The positions and, more importantly, the slopes of these regression lines are those of similar folds.

Figure 5. The appearance of ideal similar folds formed by differential simple shear of layers along parallel flow lines (flow surfaces in three dimensions). Layers act merely as passive markers with no mechanical influence. Strain is zero along axial traces, which are parallel to the flow lines. Limbs show apparent attenuation in terms of their orthogonal thicknesses, but limb thicknesses measured parallel to the axial traces are constant. Limbs are not boudinaged, and there is no shortening normal to the flow lines. (After Carey, 1962.)

Figure 6. Mechanisms for the formation of similar (Class 2) and subsimilar (nearly similar) folds. Folds with the same shape (e.g., A, B, C, E, and F) have different internal strains (diagrammatically shown by black strain ellipses) because they are formed by different mechanisms. Models A, B, and C show simple shear acting on previously unstrained layers: A, zero tangential (parallel to original layer) elongation; B, tangential shortening; C, tangential extension. D, subsimilar fold formed by homogeneous tangential shortening acting on a weakly buckled flexural fold (Class 1B parallel fold). Models A-C require unlikely reversals of shear sense across every fold axial trace. Models E-G are more realistic because they do not require reversals of shear sense. Model E shows differential simple shear (curved shear profile) acting on a stippled planar layer (which may have undergone a previous episode of uniform simple shear oriented in the opposite direction to the shear profile, as shown). Model F shows uniform simple shear (straight shear profile) acting on a layer of constant T thickness previously deformed by differential simple shear of constant shear sense. Model G shows uniform simple shear acting on a layer of constant t thickness previously deformed by flexural buckling. (E adapted from Ragan, 1969, F and G adapted from Hudleston, 1977.)

Figure 7. Models for generating folds during centripetal flow of rock salt into a salt diapir. Diapir axis lies to right of each radial section; flow in concentric section is normal to paper. (A) Shear stresses (σ_s) induced by upward flow. (B) Normal stresses (σ_n) induced by convergent

flow. (C) Shear stresses (σ_s) induced by lower boundary effects. (C adapted from Talbot, 1981, Kuh-e-Namak salt glacier, Iran.)

Figure 8. Rotation and axial constriction (by the mechanism in fig. 7A) of initially open, upright, horizontal folds (folded by the mechanism in fig. 7B) to form isoclinal, vertical folds by upward flow of salt into the trunk of a diapir.

Figure 9. Refolding and rotation (by the mechanisms in fig. 7A, B) of originally recumbent F1 folds (formed by the mechanism in fig. 7C) during flow of salt into and up the trunk of a diapir. (A) Original F1 folds. (B, C) Progressive F2 refolding analogous to Ramsay's (1967) Type 2 interference. (D) No interference patterns, apart from reversal of younging directions, are visible in cross section plane a in figure C, normal to F2 hinges. (E) Characteristic crescentic patterns visible in slightly oblique cross section plane b. Reversal of younging would also be present. (F, G) Oblique cross sections through computer modeled, orthogonally superposed folds (case N, Thiessen and Means, 1980) of similar geometry to those in figure C. Hooks and crescents predominate.

Figure 10. The changing orientations of F1 and F2 folds during F2 refolding and rotation shown in figure 9. Left, stereographic projection, right Rickard's (1971) dip-pitch-plunge diagram; curved lines in grid are for pitch. F2 folds rotate from upright (axial planes) horizontal (hinges) to vertical along a single path with upright axial planes. F1 folds rotate from recumbent to upright horizontal along an infinite number of paths (stippled area) ranging from horizontal hinges (diamond symbols) to moderately inclined (axial planes) plunging (hinges) (circle symbols). F1 folds cannot be rotated to a vertical position in the model shown in figure 9.

Figure 11. Model for the formation of vertical and near-vertical F2-F1 sheath folds (right) during D2 deformation by intense constriction of originally upright or inclined, noncylindrical folds (left) during diapiric rise of rock salt. F1 folds on the limbs of F2 folds have elliptical cross sections, whereas F1 folds in the hinge of F2 folds have crescentic or circular cross sections. The F1 sheath folds are too noncylindrical to plot on a dip-pitch-plunge diagram, but vary from upright horizontal at the culminations to vertical down the sheath flanks.

Figure 12. Cross sections through large fold interference structures in the roofs of Gulf Coast dome-salt mines, illustrating six basic patterns. These patterns are postulated to be profiles of sheath folds formed by the model shown in figure 11. Except for C, all views are downward and normal to horizontal plan projections; north is to the top of the diagram. (A, B) Grand Saline Dome, East Texas, 700-ft level of Kleer Mine (Balk, 1949). (C) Jefferson Island Dome, Louisiana, 1000-ft level of Jefferson Island Salt Company Mine (Balk, 1953). Oblique view about 60 degrees upward toward southwest. (D, E) Winnfield Dome, Louisiana, 811-foot level of Carey Salt Company Mine (Hoy and others, 1962). (F-H) Weeks Island Dome, Louisiana, 758-foot level of Morton Salt Company Mine (Kupfer, 1962). (I) For comparison, a profile through much smaller, but similar, sheath folds in mylonitic rocks from Vang, Valdres, Norway, probably deformed by intense simple shear nearly parallel to the layers (Cobbold and Quinquis, 1980).

Figure 13. Maps showing inferred flow paths and flow directions of rock salt in three dome-salt mines. Flow paths have much larger vertical components of movement, but only horizontal components are shown. Data collected by Balk (1949), Hoy and others (1962), and Kupfer (1962).

Figure 14. Maps showing plunge isogons for linear elements in rock salt in three salt-dome mines. Note the rarity of vertical plunges. See figure 13 for data sources.

Figure 15. Models for the inhomogeneous rise of material. (A) During thermal convection, maximum upward flow occurs in zones of steep plunge. (B) During differential advance, as in glacial surges, maximum upward flow takes place beneath zones of shallow plunge; zones of steep plunge mark the borders of advancing tongues. Model B is considered more appropriate for diapiric salt.

Figure 16. Cross sections through salt domes showing major structure and inferred salt tongues based on plunge isogons in figure 14. These tongues are defined by changes in plunge of linear elements rather than by conventional layering. (A) Location of cross-section lines; see also figure 14. (B, C) Alternative models for Winnfield Dome; C is more realistic and shows two major salt tongues rising symmetrically outward. (D) Almost identical structure to C in Dixon's (1975) model WD-2, in which a surface of plunge reversal of principal extensions marks the axial surface of two symmetric tongues of diapiric material. (E, F) Cross sections for the other two domes are too short to define major structures.

Figure 17. Equal-area stereographic projection showing conventions for describing orientation of structural elements relative to S_1 schistosity in the TOG-1 core.

Figure 18. (A) Structural cross section along vertical salt core, Oakwood Dome. On the basis of measurements of layering and schistosity, the section was constructed to scale assuming a mechanism of similar folding and projecting elements outward from the core for better visibility. (B) Schistosity (dashed lines) in the halite transects older isoclinal folds at arrowed localities. Thin, anhydrite-rich layers containing dark laminae (each shown as a solid line) have

been boudinaged in numerous places. Traced from contiguous thick sections. [From Dix and Jackson, 1982.]

Figure 19. Deducing the orientation of a fold axis from the trace of layering in a schistosity plane. Fold axis trends subhorizontally, parallel to strikes of S_0 and S_1 . Left, diagrammatic view of vertical core. Right, equal-area stereographic projection.

Figure 20. Medium-scale structure within Oakwood Dome, extrapolated on the basis of figure 18A. Three hypothetical structures, a, b, c, were possible. Removal of each allows for different estimates of the amount of structural truncation.

Figure 21. Model, based on figures 18 and 20, for flow patterns within Oakwood Dome. Tongues of salt are sequentially overthrust as vertical folds refolded to recumbent folds. The TOG-1 borehole has pierced the lower part of tongue 5. The upper part of this tongue has been removed by truncation of the dome crest.

Figure 22. Model deformation fabrics produced by homogeneous, plane-strain, pure shear ($R_S = 2.5$) of ideal populations of circular and elliptical particles (black dots). Initial axial ratios and orientations are designated R_i and θ , respectively and shown at left. In cases of random initial distributions (B, C) median ϕ orientations after strain (shown by arrows) are parallel to principal extension directions (long side of right rectangles). In cases of nonrandom initial distribution where the particles show bedding-preferred orientation (D, E) neither the median ϕ , nor the principal extension direction, nor the bedding trace are parallel after strain. (A-D modified from Ramsay, 1976).

Figure 23. Unstrained elliptical particles, with arbitrary numbers for reference, and a unit circle, showing initial axial ratios (R_i) and θ angles measured from a reference line. Note the sign convention for θ .

Figure 24. The particles of figure 23, after homogeneous pure shear ($R_s = 3$ illustrated by the strain ellipse), showing finite axial ratios (R_f), and ϕ angles measured from a reference line (here, parallel to the principal extension direction, X). Note the sign convention for ϕ . Most particles have become thinner and have rotated toward the X direction. But particle 3 has become fatter, particle 1 has become circular, and particle 4 is little changed in shape although its orientation has changed by 90 degrees.

Figure 25. Comparison between methods of strain analysis of perpendicular sections through the same specimen (O-1339) of rock salt in core from Oakwood Dome, showing minimum strain ($R_s = 1.2$ in XY plane) and maximum strain ($R_s = 2.8$ in XZ plane). (A) 100 mathematically unstrained grains on a R_f/ϕ plot showing estimated initial fabrics in salt before deformation. (B) 100 strained grains on a R_f/ϕ plot, showing the present strains in the salt. (C) 100 strained grains on the shape-factor grid. The ICP (initial circle point) lies on the X direction and defines the finite strain for the whole sample of grains. (D) Random-point distributions that define ellipses representing whole-rock strain. In these particular distributions the ellipses are comparatively well defined and the strain magnitudes agree with that of the other methods. But in general this method did not define strain ellipses sufficiently accurately to be used. (E) Harmonic means provide reasonably accurate strain ratios at high strains (XZ plane), but overestimate strain ratios at low strains (XY plane).

Figure 26. Strain states in rock-salt specimens O-1166, O-1178, O-1233, and O-1275 on R_f/ϕ plots. Note the increased degree of preferred orientation in the most strained (XZ) sections.

Figure 27. Strain states in rock-salt specimens O-1305, O-1315, O-1337, and O-1339 on R_f/ϕ plots. Note the increased degree of preferred orientation in the most strained (XZ) sections.

Figure 28. Strain states in rock-salt specimens O-1166, O-1178, O-1233, and O-1275 on the shape-factor grid. See figure 29 for key and scale.

Figure 29. Strain states in rock-salt specimens O-1305, O-1315, O-1337, and O-1339 on the shape-factor grid.

Figure 30. Error analysis in histogram form of strain data of 2,400 grains in the eight specimens. (A) Initial grain shapes calculated by program THETA. The median initial axial ratio was 1.5 in all three principal planes of strain. (B) Percentage overestimate of strain by the harmonic-mean method. The error increases with increase of initial grain axial ratios, R_i , and decreases with increase of imposed strain, R_s . (C) χ^2 tests for randomness by program THETA. Half of the "all grains" samples exceed the χ^2 limit of 15.5. But if separated into "large grains" and "small grains," almost all samples fall below the χ^2 limit.

Figure 31. Theoretical fabrics produced by homogeneous strains of a model sample of elliptical particles on the shape-factor grid. An initially random distribution, defining a circular field at the graph's origin, is deformed to form an elliptical field by burial or tectonic strain. Subsequently superimposed strains produce only elliptical fields. Strain ellipses above show how a finite, or total, strain can be less than even one of the incremental strains that built up the finite strain.

Figure 32. Flinn diagram showing the mean strain in the "all-grains" samples of halite recorded by all three methods of strain analysis. Numbers refer to sample numbers, equivalent to depths in feet. Line connecting points indicates upward trend in strain states. All samples lie in the flattening field of strain.

Figure 33. Hsu diagram showing the mean strain in the "all-grains" samples of halite recorded by all three methods of strain analysis. Numbers refer to sample numbers, equivalent to depths in feet. Line joining points indicates upward trend of strain states. All samples lie in the flattening field of strain.

Figure 34. Flinn diagram showing triangles of discrepancy between results obtained by different methods of strain analysis on the same specimens. The lowermost harmonic-mean value can be ignored because strain in this specimen is too low for accurate results by this method.

Figure 35. Hsu diagram showing strain states in the three different grain-size populations: all grains, large grains, and small grains. Natural strain intensity, E_S , increases outward from origin of plot. For the moderately to strongly deformed specimens, all three grain-size populations show similar levels of strain.

Figure 36. Variations in strain magnitude and type with depth. Regression lines for foliated rock salt have been statistically tested for linear fit to data and slope of line. Uppermost data points are from unfoliated rock salt. (A) Percentage shortening parallel to Z. (B) Natural strain. (C) k value, or ratio of constriction to flattening. Strain magnitudes and k values decrease significantly upward.

Figure 37. Equal-angle stereographic projection (Wulff net) of the orientations of the principal axes of strain, X, Y, and Z, assuming a southward dip of the XY foliation plane. Lines connecting points indicate upward trend of orientations. The X direction of maximum extension varies widely although the XY plane containing X dips uniformly.

Figure 38. Schematic illustration of the model proposed by Dix and Jackson (1982) for basal accretion of anhydrite cap rock, formation and closure of a dissolution cavity, and superimposed strains in rock salt and cap rock of Oakwood Dome. See text for explanation.

Figure 39. Quantitative modeling of superimposed strains in the crest of Oakwood Dome. E_1 is initial strain ellipsoid, E_2 is incremental strain ellipsoid, E_R is resultant, or final, strain ellipsoid. (A) Strains drawn to scale as blocks in true orientation. (B) Equal-area stereographic projection (Schmidt net) showing orientation of principal strain axes of the three strain ellipsoids. (C) Flinn diagram showing deformation path of E_1 strain ellipsoid being converted to E_R strain ellipsoid by addition of E_2 strain increment.